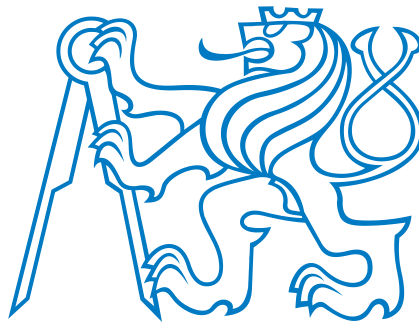


Optimization of Masonry Mortars Based on Numerical Modeling and Experimental Observations

Jakub Antoš

supervisor: **Jan Zeman**

co-supervisor: **Václav Nežerka**



Czech Technical University in Prague

Faculty of Civil Engineering
Department of Mechanics

I would like to dedicate this thesis to my deceased grandfather Milan Antoř.

Honesty Declaration

I declare that this master thesis has been carried out by me and only with the use of materials that are stated in the literature sources. Results are going to be published in the Construction and Building Materials journal.

September 28th, 2014

Jakub Antoš

Acknowledgements

First of all, I would like to thank my supervisor Jan Zeman for his support, encouragement, and patience. Also I would like to thank my co-supervisor Václav Nežerka for his indispensable advice, explanation, motivation, and fruitful discussions. Cooperation with them was very valuable for me and their knowledge is a big inspiration for the future. Next, I want to express my gratitude to my colleague Pavel Tesárek for his willingness to help me with the preparation of experiments any time I needed. Special thanks go to Professor Petr Kabele for his trust in me and for giving me the opportunity to participate in the project led by him.

Thanks also belong to several members of the Department of Mechanics at Faculty of Civil Engineering, CTU in Prague, in particular to Professor Bořek Patzák for his patience when introducing me into the finite element analysis software OOFEM, to Jiří Litoš and his crew of the Experimental Centre at Faculty of Civil Engineering, CTU in Prague, for their selflessness during the experimental testing of masonry piers and to Pavel Kokeš for his help with experimental assessment of material properties of mortars. Last but not least my thanks belong to my parents, Vladimíra Antošová and Bohumil Antoš for their support during the whole studies and to my girlfriend Shirleny Monserrat Sandoval Arias for her patience with me during writing this thesis.

The support of Ministry of Culture of the Czech Republic under the project NAKI, No. DF11P01OVV008, is gratefully acknowledged.

Abstract

Lime-based mortars were frequently used in history and therefore they are required for restoration of ancient masonry structures by public authorities. However, their slow setting, relatively low tensile strength, and quite extensive shrinkage cracking are the main obstacles to their application. These have been partly overcome by the addition of pozzolans, such as volcanic ash or crushed clay products, exploited by masons since the Roman period. Such mortars proved to be more resistant especially with respect to seismic loading. The enhancement of mechanical properties was later attributed to the formation of hydration products such as CSH gels present in modern Portland cement concrete. In the case of addition the crushed clay products, such as pottery or brick fragments, the reduced shrinkage cracking at the interface between the compliant particles and the surrounding matrix seems to have the major positive impact on the mortars. The Romans used crushed clay aggregates where there was no natural source available, and these mortars, known as *cocciopesto*, exhibited a remarkable resistance.

The presented study exploiting the combination of numerical simulations and advanced experimental measurements reveals the influence of various mortars intended for the repairs of cultural heritage on the behavior of masonry loaded in compression and bending. The results indicate that the traditional materials can be efficiently utilized for the production of modern high-strength mortars compatible with the materials used in ancient times.

Abstrakt

Vápenné malty byly v minulosti široce používány a proto jsou dnes vyžadovány pro opravu historických zděných konstrukcí ze strany památkové péče. Nicméně jejich pomalé tuhnutí, relativně nízká pevnost v tahu a vznik smršťovacích trhlin jsou hlavní překážky pro jejich použití. Tyto překážky lze částečně překonat přidáním pucoánů, jako je sopečný popel nebo drcené výrobky z pálené hlíny, čehož využívali zedníci už v Římském období. Tyto malty se ukazují být odolné zejména s ohledem na seismické zatížení. Zlepšení mechanických vlastností bylo později připisováno tvorbě hydratačních produktů, jako jsou CSH gely přítomné v moderním betonu z portlandského cementu. V případě přídavku drcených jílových výrobků, jako jsou keramika nebo úlomky cihel, dochází ke snížení výskytu trhlin na rozhraní mezi částicemi a okolní maticí. Římané používali drcené jílové produkty, když nebyly k dispozici žádné jiné zdroje a tyto malty, známé jako *cocciopesto*, vykazovaly pozoruhodnou odolnost.

Prezentovaná studie využívá kombinaci numerických simulací s pokročilým experimentálním měřením deformací, využívajícím korelace digitálního obrazu. Konkrétně je studie zaměřena na vliv spárových malt zamýšlených pro opravy kulturních památek, na chování zdiva zatíženého tlakovou silou a ohybovým momentem. Výsledky naznačují, že tradiční materiály mohou být efektivně využity pro výrobu moderních vysokopevnostních malt, kompatibilních s materiály používanými v dávných dobách.

Contents

List of Figures	viii
1 Introduction and State of Art	1
1.1 Historical Background	1
1.2 Requirements for Nowadays Repair Mortars	2
1.3 Chemical Processes	3
1.3.1 Air Lime	3
1.3.2 Lime with Hydraulic Properties	5
1.3.3 Portland Cement	6
1.3.4 Pozzolans	8
2 Experimental Analysis	11
2.1 Basic Testing of Mortars	11
2.1.1 Composition of Tested Mortars	11
2.1.2 Acquisition of Basic Material Parameters	13
2.1.3 Results	17
2.2 Experimental Testing of Masonry Piers	19
2.2.1 Specimen Preparation	19
2.2.2 Destructive Testing	20
2.3 Digital Image Correlation	21
2.3.1 DIC principles	21
2.3.2 Contrast Pattern	25
2.3.3 Acquisition of Input Images	26
2.3.4 Processing of Acquired Images	27
2.3.5 DIC Processing	27
2.3.6 Results of DIC	34
3 Numerical Simulations	38

3.1	Summary of the Theory of Elasticity	38
3.1.1	Kinematic Equations	38
3.1.2	Static Equations	42
3.1.3	Constitutive Equations	45
3.2	Introduction to FEM	46
3.2.1	Principle of FEM	47
3.2.2	Convergence Conditions	48
3.2.3	Linearity / Nonlinearity	48
3.3	Numerical Modeling	52
3.3.1	Material Model	52
3.3.2	Numerical Simulations of Masonry Pier Failure	56
4	Results	59
4.1	Comparison of Crack Patterns	59
4.2	Influence of Mortar Properties on Mechanical Resistance of Masonry Piers	60
4.2.1	Influence of Mortar Young's modulus	61
4.2.2	Influence of Mortar Tensile Strength	61
4.2.3	Influence of Mortar Compressive Strength	62
4.3	Discussion of Results	63
5	Conclusions	65
	References	67

List of Figures

1.1	Typical ancient masonry structures.	2
1.2	Fragments of pottery in ancient samples of cocchiopesto mortar, reproduced from [1].	10
2.1	Grading curves of sand and crushed brick aggregates.	12
2.2	Processing of modal analysis by resonance method.	15
2.3	Sample of brick as documentation of three-point-bending test and sample of LMK-SCB mortar as an example of compression test.	16
2.4	Execution of adhesive strength tests.	17
2.5	Individual force-displacement diagrams for compression (left) and three-point-bending (right) tests of brick.	18
2.6	Individual force-displacement diagrams for compression tests of mortars.	18
2.7	Individual force-displacement diagrams for three-point-bending tests of mortars.	19
2.8	Loading of the tested piers and placement of virtual extensometers.	20
2.9	The reference and current image, the subset's coordinates are shown as red crosses.	22
2.10	Linear transformations for subset coordinates, reproduced from [2].	23
2.11	Artificial stochastic contrast pattern.	25
2.12	Experimental testing of columns.	26
2.13	Comparison of <i>.jpg</i> compression ratio.	27
2.14	Main menu window in Ncorr.	28
2.15	Window with settings of DIC in Ncorr.	29
2.16	Optimal distribution of seeds (green dots) in Ncorr.	30
2.17	Displacement formatting window in Ncorr.	30
2.18	Strain Analysis window in Ncorr.	31
2.19	Ncorr plotting options.	32
2.20	Main window of Ncorr_post application.	33
2.21	Example of virtual extensometers data plotting provided by Ncorr_post.	33

2.22	Direction and magnitude of principal strains; L-SCB pier in 410 seconds of the test.	34
2.23	Time step: 0s (left) 200s (right).	35
2.24	Time step: 300s (left) 400s (right).	35
2.25	Time step: 500s (left) 600s (right).	36
2.26	Time step: 650s (left) 700s (right).	36
2.27	Time step: 750s (left) 790s (right).	37
3.1	Governing equations of elasticity, reproduced from [3].	39
3.2	Two-dimensional geometric deformation of an infinitesimal material element, reproduced from [4].	40
3.3	Illustration of Newton-Raphson method.	50
3.4	Illustration of Modified Newton-Raphson method.	51
3.5	FE model of specimens for three-point bending (left) and uniaxial compression (right) tests.	53
3.6	Fitting of the material model input parameters representing bricks on results of three-point bending (left) and uniaxial compression (right) tests.	54
3.7	Fitting of the material model input parameters representing mortars on results of three-point bending tests.	55
3.8	Fitting of the material model input parameters representing mortars on results of uniaxial compression tests.	55
3.9	Geometry and FE mesh of investigated masonry pier.	56
3.10	Boundary conditions of FE model.	57
3.11	Comparison between the numerically and experimentally obtained load-displacement diagrams, describing the response of the tested masonry piers to the imposed vertical displacement at the crest of the loading cell.	58
4.1	DIC map of maximum principal strain (left within the couple) and FE model damage prediction (right) on the face of the tested piers after reaching load-peak.	60
4.2	Dependence of the masonry pier load-bearing capacity on mortar stiffness; black line represents the Youngs modulus of the bricks, $E^{(b)} = 14$ GPa.	61
4.3	Crack patterns on masonry piers containing compliant ($E^{(m)} = 2$ GPa, left) and stiff ($E^{(m)} = 20$ GPa, right) mortar.	61
4.4	Dependence of the masonry pier load-bearing capacity on mortar tensile strength; black line represents the tensile strength of the bricks, $f_t^{(b)} = 2.7$ MPa.	62
4.5	Crack patterns on masonry piers containing weak ($f_t = 0.1$ MPa, left) and strong ($f_t = 3.2$ MPa, right) mortar in tension.	62
4.6	Dependence of the masonry pier load-bearing capacity on mortar compressive strength; black line represents the compressive strength of the bricks, $f_c^{(b)} = 30$ MPa.	63

-
- 4.7 Crack patterns on masonry piers containing weak ($f_c = 3$ MPa, left) and strong ($f_c = 33$ MPa, right) mortar in compression. 63

Chapter 1

Introduction and State of Art

The purpose of this thesis is to investigate the structural performance of different mortars commonly used in the repairs of historic buildings. The study consists of a comprehensive experimental and numerical analysis. The material properties of individual constituents were found by standard laboratory tests, namely uniaxial compression and three-point bending. Several lime-based and cement-based mortars with various additives were used in the bed joints of masonry pillars subjected to a quasi-static combination of compression and bending. An experimental analysis was employed to study the failure modes and crack patterns using the digital image correlation (DIC), to assess the structural performance of the investigated mortars and verify the proposed material model implemented in the finite element (FE) package OOFEM. Numerical FE analysis was then used for parametric studies of key material parameters that affect the load-bearing capacity and failure modes of the masonry piers.

1.1 Historical Background

Mortars is among the oldest and the most widely used building materials for their compliance and their easy adaptability to the morphological needs of the construction work. In human history various types of mortars were invented. From a modern chemical point of view it is possible to divide them into two general groups: mortars based on hydraulic or non-hydraulic chemical components. The term historical mortar is used basically for all types of mortars which have been used before the Portland cement invention in 19th century. The first mortars were made of mud and clay. According to research of Roman Ghirshman, the first evidence of humans using a form of mortar was at the Mehrgarh of Baluchistan in Pakistan, built of sun-dried bricks bounded by clay [5] in 6,500 BC. Additional progress was achieved with the invention of lime. In the Middle Ages the use of mortars undergone huge research and the first mortars based on hydraulic reaction were invented. These mortars were composite material formed by a binder (hydraulic or aerial lime) and variety of inert materials (silicate, dolomite or carbonate sand) and some additives mentioned further.

Historical and monumental buildings represents the culture and stories of the people who built and lived in them. This makes the places with well-preserved cultural heritage very attractive for tourists, which has a huge positive impact on the popularity and economy of these regions. For this reason, preservation and restoration of historic masonry structures is usu-

ally supported by the governments or organizations. Most famous organization to preserve cultural heritage, but not only for this purpose, is United Nations Educational, Scientific and Cultural Organization, UNESCO, a specialized agency of the United Nations. UNESCO has 195 member states around the whole world, it was founded in 1946 and the location of the major mansion is in Paris, France. Inappropriate attempts to recondition can cause enormous damage, and therefore authorities for cultural heritage have introduced numerous demands on techniques and materials used for the protection and repairs of these structures. Among the most important historical structures could be regarded: Hagia Sofia in Istanbul, Turkey; Cathedral of the Holy Cross and Saint Eulalia in Barcelona, Spain; St Peter's Basilica in Rome, Italy; Monastery San Vicente de Fora in Lisbon, Portugal; or Byzantine monuments on the island of Crete, Greece.



(a) Hagia Sofia arches

(b) Panagia Kera in Crete

Figure 1.1: Typical ancient masonry structures.

1.2 Requirements for Nowadays Repair Mortars

Masonry structures usually exhibit high durability, but on the other hand, they are relatively difficult to maintain. Deterioration and damage are usually concentrated in the joints between brick or stone units. It is widely known, not only in the academic area, that the mortars for repairs have to be compatible with the original materials. In the last 50 years, serious damage to a number of historical masonry structures was caused by the extensive use of Portland cement in the mortar mixtures [6, 7, 8]. The aim of the Portland cement use was to increase initial strength, durability, and reduce shrinkage. In their unmodified form, the lime-based mortars exhibit opposite behavior: slow increase of strength, high shrinkage, and low ultimate strength [9]. However, the use of Portland cement-based mortars was finally reconsidered, due to their low plasticity, excessive brittleness, and rigidity of earnings at the beginning [10, 11, 12, 13]. In addition, the relatively high content of soluble salts such as most common are calcium sulphate – CaSO_4 and sodium sulphate – Na_2SO_4 is also undesirable. These salts leach over time [11, 12, 13] and can seriously damage the original masonry units due to the high crystallization pressures [14, 15] and produce anesthetic layers on the surface of masonry elements. Maravelaki-Kalaitzaki et al. [16] also criticized cement-based mortars, which were used for restoration purposes, for their limited physico-chemical and mechanical compatibility with the old masonry. The adhesion of cement-based to the old historic materials was found very poor, their thermal conductivity usually much higher, and the open porosity lower than of the lime-based mortars [15].

Very strict regulations in relation to the use of Portland cement-based mortars have led to the use of traditional ingredients such as volcanic ash, burnt clay shale [17] or metakaolin [13] especially during the last decades. These additives known as *pozzolans* have been used since ancient times in combination with lime to improve the moisture resistance of mortars, their resistance to frost [18], and also extend their lifetime [9, 13] and mechanical strength [19, 20]. Many researchers believe that the first use of truly cementitious binding agents – pozzolans (occurred in southern Italy around the second century BC) was a first little resemblance to modern Portland cement concrete. The Pantheon, constructed in 126 AD, is one of the structural marvels of all times. This adoption of Pantheon rotunda is based upon the use of volcanic ash from near Pozzuoli, which has been combined with the lime to provide concrete far stronger than anything previously produced. Nowadays usage of pozzolans is also very important in the case of mortars for repairs, which are more resistant to cracking. Pure lime mortars can cause peeling of facade surface layers which has a negative aesthetic impact [21]. Pozzolanic additives are also very effective in reducing clotting [22], shrinkage and the subsequent creation of initial microcracks which reduce initial effective mortar stiffness [23, 24].

After a long period of lime-based mortars use, ancestors tried to find an alternative to natural pozzolans when there was no natural source available in the region. The Phoenicians were probably the first to add powdered clay products such as clay bricks [25], tiles or pieces of crushed earthenware to mortar, so as to increase their durability and strength. Crushed bricks were often added to the mortar used in load-bearing walls during the Roman Empire [26] and Romans called the material *cocciopesto* [27]. Cocciopesto mortars were widely used from the early Hellenistic period until the Ottoman water retaining structures to protect the walls from moisture, typically in the spa, canals, and aqueducts [28, 29]. Brick dust was mainly used for rendering, while large pebbles to of 25 mm in diameter appeared mainly in masonry walls, vaults, and foundations [25] and joint thickness often exceeded 40 mm (in case of Hagia Sofia even 70 mm thick joints are no exception).

Better effective mechanical properties such strength, improved resistance to weather conditions – durability and last but not least higher resistance to seismic load are attributed to the additional formation of hydration products. A few researchers suggest [22, 23, 30] that these products arise on the interface between crushed bricks and surrounding lime-based matrix.

1.3 Chemical Processes

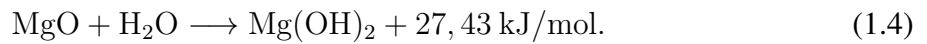
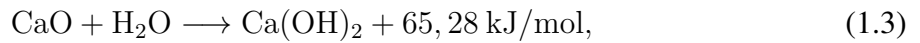
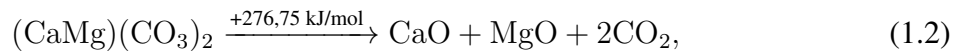
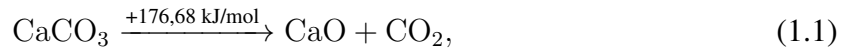
Knowledge of basic chemical processes is necessary for the deeper understanding of mortars behavior. There are basically two principal groups of binders: air and hydraulic binders. Typical representative air binder is well-known air lime and on the other hand as an exemplary hydraulic binder is considered lime with hydraulic properties or modern Portland cement. Hydraulic binders are demarcated by the ability to set and harden in a very humid environment, or completely under water.

1.3.1 Air Lime

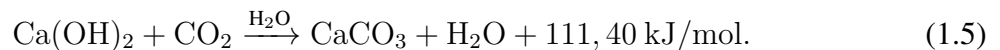
Air lime is produced from calcium carbonate (CaCO_3), referred to as calcite, with a varying level of calcium magnesium carbonate ($\text{CaMg}(\text{CO}_3)_2$ - dolomite. In the nature, calcite can be

found in a variety of forms, for example chalk or limestone. To convert the raw material into air lime, heating to temperatures below the needed range required for sintering, 900 – 1250 °C, must be ensured. At these temperatures, the limestone breaks down by giving off carbon dioxide (CO₂) leaving calcium oxide (CaO) and magnesium oxide (MgO). The compound needs to pass through grinding in ball or bar mills into a very fine powder (<0.09 mm). Mixture of these two components is known as quicklime. Basically two various forms of quicklime are possible to create, depending on the temperature of heating process and the speed of temperature increment. Fast heated calcite is transformed to hard quicklime, while the soft quicklime is heated slowly and in a lower temperature. Soft quicklime is suitable to use in lime mortars for its higher reactivity, higher porosity and consequent lower bulk density.

Quicklime is unstable and needs to be hydrated with water, this process is called slaking. Two ways of slaking are available: wet and dry. Wet slaking is accompanied with relatively high excess of water and this process is suitable to use in-situ on a construction sites. This reaction is exothermic and the temperature shall not exceed 100 °C. Dry slaking is done only in the lime-kilns with only small excess of water and the designation of the final product is lime hydrate. From a chemical point of view, the result of both methods is calcium hydroxide or easily said slaked lime. Whole chemical process of lime production could be described the following equations:



The process of air-lime hardening consists of two phases: desiccation of colloidal gel (evaporating the moisture from the mortar mix) and process of carbonation. Carbonation reaction involves the transformation of calcium hydroxide into calcium carbonate as a result of the reaction between calcium hydroxide and atmospheric carbon dioxide. This reaction is controlled by the diffusion of the CO₂ through the pores, dissolution of the CO₂ and calcium hydroxide in the water within the capillary pores, and reaction between Ca²⁺ and CO₃²⁻ ions forming insoluble calcium carbonate crystals. The reaction proceeds slowly and continues until either all calcium hydroxide has reacted. In a simplified form the process can be described by the following equation:



Purity of commercial produced limes is regulated by EN 459-1:2010 the European standard for Building Lime, which is not very strict. By the content of MgO or Mg(OH)₂ the quick lime is divided into two groups: quicklime with MgO ≤ 5% content is **calcium lime**, with a higher content is designated as **dolomitic lime**. Complete list of commonly produced building air limes is shown in Table 1.1.

Table 1.1: List of building air limes, reproduced from [31]

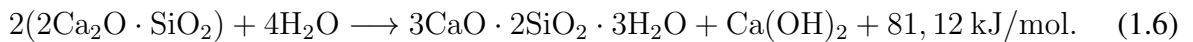
Designation	Notation	Values given as mass fraction in percent			
		CaO + MgO	MgO	CO ₂	SO ₃
Calcium lime 90	CL 90	≥ 90	≤ 5	≤ 4	≤ 2
Calcium lime 80	CL 80	≥ 80	≤ 5	≤ 7	≤ 2
Calcium lime 70	CL 70	≥ 70	≤ 5	≤ 12	≤ 2
Dolomitic lime 90-30	DL 90-30	≥ 90	≥ 30	≤ 6	≤ 2
Dolomitic lime 90-5	DL 90-5	≥ 90	≥ 5	≤ 6	≤ 2
Dolomitic lime 85-30	DL 85-30	≥ 85	≥ 30	≤ 9	≤ 2
Dolomitic lime 80-5	DL 80-5	≥ 80	≥ 5	≤ 9	≤ 2

1.3.2 Lime with Hydraulic Properties

Production of lime with hydraulic properties is very similar to the air lime production process. Main raw materials are argillaceous or siliceous limestones containing calcite and impurities such as dolomite and calcareous marls or other marlites. Marlites have a natural content of hydraulic agents, primarily silica (SiO₂) and alumina (AlO₃). These agents are major bearers of the hydraulic properties. As a result of the burning process, silica and alumina react with lime to form silicates and aluminates, especially dicalcium silicate - 2CaO·SiO₂ (C₂S in cement chemistry notation¹).

Tricalcium silicate - 3CaO·SiO₂ (C₃S) can be present as well, but in a very low amount (C₃S forms at higher than 1250 °C temperature).

Another way how to prepare lime with hydraulic properties is to mill the air lime together with additives (pozzoans). Burning and slaking procedures are thus more complex than those associated with the production of air lime, but the materials produced are far more versatile. Hardening of lime with hydraulic properties is a very complex problem, but at least one equation should be mentioned, hardening of C₂S phase:



Sub-families of limes with hydraulic properties are: natural hydraulic lime **NHL**, formulated lime **FL** and hydraulic lime **HL**. Their properties depend on the composition, burning and slaking.

- **NHL** lime is made by burning more or less argillaceous or siliceous limestones with reduction to powder by slaking with or without grinding. The hydraulic properties exclusively result from the special chemical composition of the natural raw materials.
- **FL** lime mainly consisting of air lime with NHL and/or with some pozzolanic material additives. Inclusion of any cement or cement clinker must be declared and present in a limited percentage.

¹Cement chemistry notation was developed to simplify expressions of complicated chemical compounds of cement. The notation does not have any relation with a ordinary chemistry elements. Individual abbreviations represent: C – CaO, S – SiO₂, A – Al₂O₃, F – Fe₂O₃, T – TiO₂, M – MnO, K – K₂O, N – Na₂O, H – H₂O.

- **HL** lime consists of by lime and other additives such as cement, fly ash, blast surface slag, limestone filler and other suitable materials.

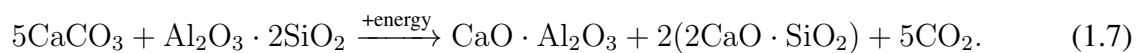
The standart ČSN EN 459 1 [31] divides the limes with hydraulic properties by volume mass of SO_3 and $\text{Ca}(\text{OH})_2$ and their compressive strengths in 7 and 28 days; the complete list is provided in Table 1.2. At first sight there is no difference between the FL A, B and C but applications of these limes are different.

Table 1.2: List of building limes with hydraulic properties, reproduced from [31]

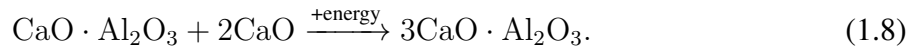
Designation	Notation	Mass fraction in percent		Compress. strg. [MPa]	
		SO_3	$\text{Ca}(\text{OH})_2$	7 days	28 days
Natural hydraulic lime 2	NHL 2	≤ 2	≥ 35	–	≥ 2 to ≤ 7
Natural hydraulic lime 3,5	NHL 3,5	≤ 2	≥ 25	–	$\geq 3,5$ to ≤ 10
Natural hydraulic lime 5	NHL 5	≤ 2	≥ 15	≥ 2	≥ 5 to ≤ 15
Formulated lime A	FL A 2	≤ 2	≥ 40 to < 80	–	≥ 2 to ≤ 7
	FL A 3,5	≤ 2	≥ 25 to < 50	–	$\geq 3,5$ to ≤ 10
	FL A 5	≤ 2	≥ 15 to < 40	≥ 2	≥ 5 to ≤ 15
Formulated lime B	FL B 2	≤ 2	≥ 40 to < 80	–	≥ 2 to ≤ 7
	FL B 3,5	≤ 2	≥ 25 to < 50	–	$\geq 3,5$ to ≤ 10
	FL B 5	≤ 2	≥ 15 to < 40	≥ 2	≥ 5 to ≤ 15
Formulated lime C	FL C 2	≤ 2	≥ 40 to < 80	–	≥ 2 to ≤ 7
	FL C 3,5	≤ 2	≥ 25 to < 50	–	$\geq 3,5$ to ≤ 10
	FL C 5	≤ 2	≥ 15 to < 40	≥ 2	≥ 5 to ≤ 15
Hydraulic lime 2	HL 2	≤ 3	≥ 10	–	≥ 2 to ≤ 7
Hydraulic lime 3,5	HL 3,5	≤ 3	≥ 8	–	$\geq 3,5$ to ≤ 10
Hydraulic lime 5	HL 5	≤ 3	≥ 4	≥ 2	≥ 5 to ≤ 15

1.3.3 Portland Cement

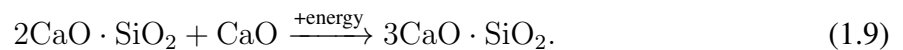
Portland cement is the basic ingredient of cement-based mortars and modern concrete. The first manufacturing step is combining a variety of raw ingredients so that the resulting cement attains the desired chemical composition. Materials used for manufacturing the Portland cement include limestone, shells, and chalk or marl combined with with additives as shale, clay, slate, blast furnace slag, silica sand, and iron ore. Most commonly the Portland cement is produced using so called "dry method" which consists of crushing the ingredients, their mixing and finally heating in the cement kiln up to level of sintering which is around 1550°C . The major chemical reaction is dehydroxylation of limestone and clay minerals at temperatures between 450 to 600°C :



In the next stage around 900 to 950 °C the formation of C₃A from the previous stage product (CA) is dominant and calcium oxide (created by thermal decomposition of calcium carbonate as in case of lime). The process can be described by the following equation:



Above the temperature 1250 °C, the melted minerals emerge in the form of liquid phase and among others C₃S is formed:



Eventually, clinker is formed and the cooling phase follows. The high rate of cooling to about 1100 °C is important to provide highly reactive cement rich in C₃S and avoid formation C₂S and CaO. Once the nodules of cement clinker have cooled, they are ground into a fine powder in a large grinding ball or bar mills. At the same time, a small amount of calcium sulfate such as gypsum (calcium sulfate dihydrate) is blended into the cement. The calcium sulfate is added to control the rate of early reaction of the cement.

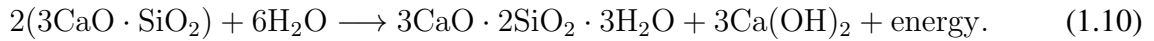
About 90 – 95% of a Portland cement is comprised of the four main cement minerals, which are C₃S, C₂S, C₃A, and C₄AF, with the remainder consisting of calcium sulfate, alkali sulfates, unreacted (free) CaO, MgO, and other minor constituents left over from the clinkering and grinding steps [32]. The four cement minerals play very different roles in the hydration process that converts the dry cement into hardened cement paste. Five main groups of Portland cement are distinguished according to the ratio of the individual minerals, see Table 1.3 for detailed description.

Table 1.3: General features of the main types of Portland cement, reproduced from [33]

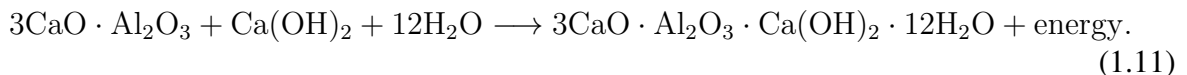
Type	Characteristics	Applications
CEM I	Fairly high C ₃ S content for good early strength development	General construction (most buildings, bridges, mortars, precast units, etc.)
CEM II	Low C ₃ A content (< 8%)	Structures exposed to soil or water containing sulfate ions
CEM III	Ground more finely, may have slightly more C ₃ S content	Rapid construction, cold weather concreting
CEM IV	Low content of C ₃ S (< 50%) and C ₃ A	Massive structures such as dams or huge foundations
CEM V	Very low C ₃ A content (< 5%)	Structures exposed to high levels of sulfate ions

Each of the four main cement minerals reacts at a different rate and tends to form different solid phases when it hydrates. The whole hydration process is a complex problem as in the case of limes with hydraulic properties. Hydration of C₃S, which is the most abundant and important cement mineral in Portland cements and mostly contributes to the early strength gain

of C-S-H gel (calcium-silicate-hydrate gel), is described by the following equation:



C_2S hardens slowly and contributes largely to strength increases at ages beyond 7 days. By the reaction of C_3A a large amount of heat during the first day of hardening is released. This reaction, together with C_3S and C_2S development, is mainly responsible for the early strength gain and the hydration process can be described by the following equation:



More detail informations about the hydration of Portland cement can be found in [32].

1.3.4 Pozzolans

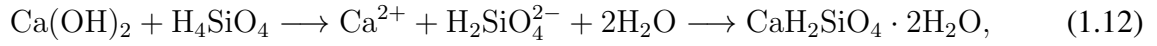
Pozzolanic materials are natural substances or industrial by-products having an amorphous or partially crystalline structure formed by silica, silico-aluminium compounds or a combination of both. Pozzolans do not harden when mixed with water, but when they are finely powdered and in presence of water, they are able to react with the calcium hydroxide at ambient temperature to form hydrated calcium silicates, enhancing the strength and durability of the lime-based mortars. In fact the pozzolan-lime reaction is activated even in the case of high air humidity and therefore these are referred to as a hydraulic binders. Main hydration product is C-S-H gel (like in the case of Portland cement). There are five major sources of pozzolans provided in the list below.

- Naturally occurring pozzolan deposits, an ash like product of volcanic activity, can be found in Europe and the Middle East, among other regions. This type of pozzolan is very suitable for use in mortars cured in wet conditions.
- Pozzolanic material also can be derived from fired and crushed clay, such as bricks or brick dust. Kaolinite can be used as the fired product, too, and the formed product is referred to as metakaolin. This variety is more durable than volcanic pozzolan.
- Furnace slag from industrial processes such manufacturing steel, this type is currently used as a concrete admixture.
- Fly ash, collected from the exhaust gases during the burning coal or lime by electrostatic precipitators or bag filters. It is weaker than the other pozzolans and generally not suitable for brick-and-mortar construction.
- Some pozzolans have been produced by crushing rock and sand, and these have been used in mortars throughout history but are not commonly used today [34].

Nowadays, the addition of pozzolanic additives to aerial lime mortars is recommended because they are responsible for the enhancement of mechanical properties in the early age, high values of mechanical strength, low water permeability, good cohesion between binders and aggregates, and increased durability [9, 13].

1.3.4.1 Pozzolanic Reaction

The acid-based pozzolanic reaction involves calcium hydroxide and silicic acid and can be schematically represented as follows:



or using the established cement chemistry nomenclature as

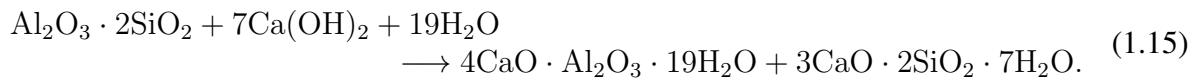


The ratio between calcium and silica, Ca/Si, and the number of water molecules can vary. Silicic acid, H_4SiO_4 , is a product of hydration by the simple equation:



1.3.4.2 Metakaolin

Metakaolin, $\text{Al}_2\text{O}_3 \cdot 2\text{SiO}_2$, is a dehydroxylated form of the clay mineral kaolinite. It belongs to a group of natural pozzolans and industrially produced by heat treatment of kaolinite clays. Kaolinite has a chemical composition of $\text{Al}_2\text{O}_3 \cdot 2\text{SiO}_2 \cdot 2\text{H}_2\text{O}$. When heat treated at the temperature within the range of 600 to 900 °C, the chemically bound water is driven away to form an amorphous aluminosilicate called metakaolin. The calcination temperature depends on the characteristics of the parent kaolin clay, such as degree of crystallinity and particle size. At higher temperatures, it recrystallizes, resulting in the formation of mullite ($\text{Al}_6\text{Si}_2\text{O}_{13}$) or spinel (MgAl_2O_4) and amorphous silica [35] that reduces its pozzolanic reactivity. The reactivity of metakaolin is dependent upon the amount of kaolinite contained in the original clay material. The average particle size of metakaolin varies and can be controlled during processing to change its properties. Metakaolin is typically white or gray in color and traditionally used in the manufacture of porcelain. Hydration of metakaolin can be expressed by following equation:



1.3.4.3 Crushed Bricks

Natural (volcanic) pozzolans were the primary additive to lime mortars in ancient Rome, crushed brick was used as an alternative when pozzolans were not available, as was mentioned in Section 1.2. This fact is cited in Vitruvius's Ten Books on Architecture and has been evidenced in analysis of samples of ancient mortar found throughout the Roman Empire as demonstrated in Figure 1.2.

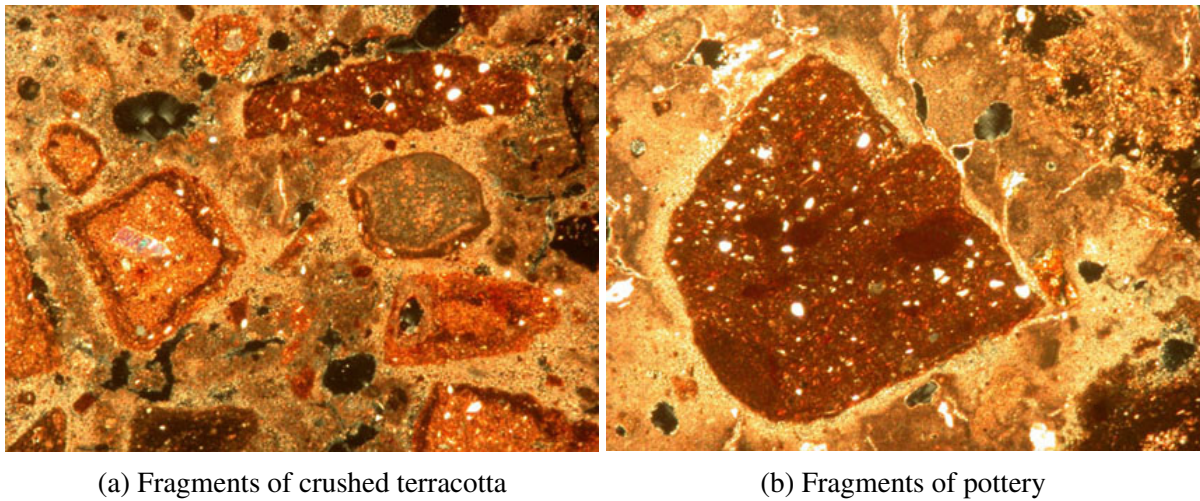


Figure 1.2: Fragments of pottery in ancient samples of cocciopesto mortar, reproduced from [1].

The observed reactions could be attributed to the calcium silicate formations at the interface along the brick or pottery fragments and lime, which makes the interfacial surface alkaline and causes chemical reaction. The penetration of lime into the ceramic and the consequent reaction transforms the microstructure of the ceramic by shifting the pore radii into smaller pores [36]. The reaction product fills the discontinuities of the structure, thus eliminating discontinuities between the mortar and the brick. Small fragments of brick also seem to penetrate the adjacent mortar [25]. This transformation matches with the hydraulic character of the mortar matrix, imparting to the mortar high physico-chemical resistance as well as high strength [36].

Chapter 2

Experimental Analysis

The experimental analysis consisted of preparation and testing of mortar samples. The experimental study included two major stages – first, an investigation of the basic material parameters via three-point bending and compression tests and consequent reproduction using FE analysis. The second stage consisted of full-scale testing of masonry piers.

2.1 Basic Testing of Mortars

2.1.1 Composition of Tested Mortars

Commonly available white air-slaked lime (CL 90-Q) Čertovy schody of a very high purity (98.98% of CaO + MgO), produced near the village Tmaň, in Czech Republic was selected in the study. The size distribution of particles was balanced and the most frequent diameter was around 15 μm . The specific area, investigated by the air permeability based on Blaine method, was equal to 16.5 m^2/g .

Metakaolin was chosen as a suitable pozzolanic material, because of its high reactivity and good availability. Metakaolin, with its commercial name Mefisto L05, produced by České lupkové závody Inc., Nové Strašecí, Czech Republic is composed mainly from silicates and aluminates, namely SiO_2 (52.1 %) and Al_2O_3 (43.4 %) but also contains Fe_2O_3 (1.1 %), TiO_2 (1.8 %) and MgO (0.18 %). Control values of granulometry analysis were determined by the manufacturer as $D_{50}=3\mu\text{m}$ and $D_{90}=10\mu\text{m}$. Portland cement CEM I 42.5 R produced in Radotín cement plant, Czech Republic was used as an pozzolanic binder alternative to metakaolin to provide a comparison. Composition of selected Portland cement was following: CaO (66 %), SiO_2 (20 %), Al_2O_3 (4 %), Fe_2O_3 (3 %), SO_3 (3 %) and MgO (2 %), as provided by XRF analysis.

This work is aimed on the investigation of the metakaolin and cement influence on the mechanical properties of lime-based mortars. Beside this, the study is also focused on the influence of aggregate composition. Previous FE simulations indicate that the mortars with angular aggregates exhibits higher fracture energy because the shape of grains works as an efficient obstacle against the crack propagation [3]. As a principal filler river sand of grain size ranging between 0 and 4 mm from Zálezlice was selected. This choice was based on the

experience from previous projects [3, 22, 24] as the most suitable for the application as the bed joint mortar.

Crushed brick particles were also used as a part of the filler as a substitution of river sand. Previous studies indicate [3, 24] influence of aggregate stiffness on fracture-mechanical properties – not so rigid aggregates are able to better cooperate with surrounding lime matrix. Further reason for the use of crushed brick fragments are the results of previous analyses of ancient samples [6, 25, 37], justifying their use in order to increase the mortar strength. Crushed brick particles from a brick plant Bratronice, Czech Republic, of grain-size distribution between 2 – 5 mm were used. Particle size distribution curves of river sand and crushed brick obtained by sieve analysis in accordance with the norm ČSN EN-1015-1 [38] are shown in Figure 2.1.

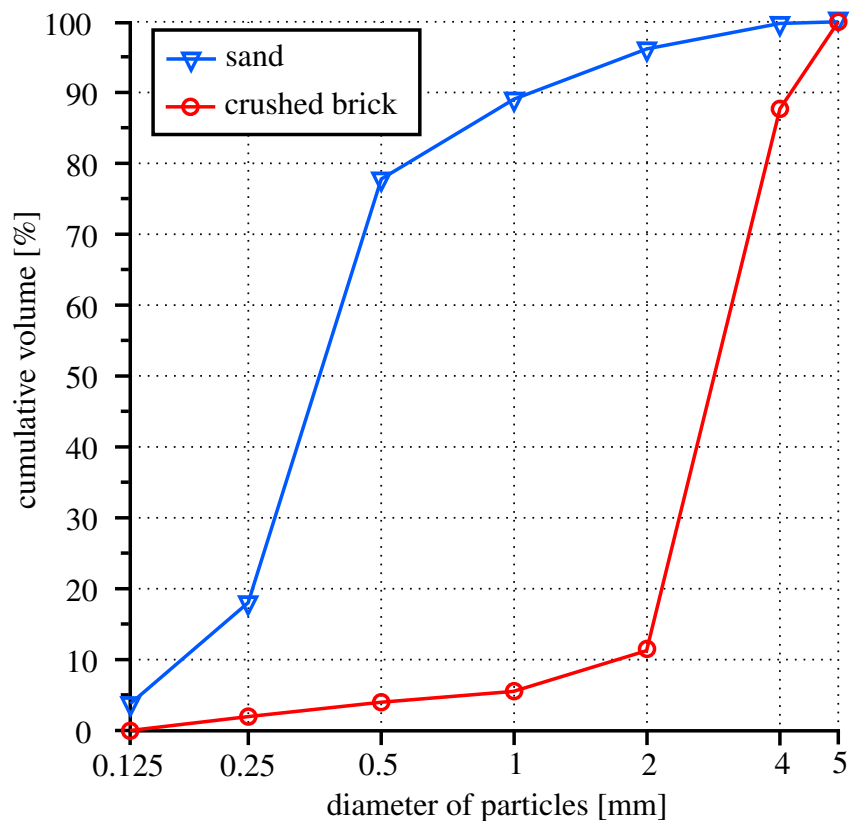


Figure 2.1: Grading curves of sand and crushed brick aggregates.

The mass proportion ratio between lime and metakaolin or Portland cement was equal to 7:3 in all mortar mixtures. The water / binder (w/b) ratio was optimized with the respect of workability test of mortar in accordance with ČSN EN 1015-3 [39]. The mortar cone expansion reached 13.5 ± 0.3 cm in all cases. One of the priorities was to keep the water to binder ratio as low as possible to avoid initial cracking induced a high shrinkage. We also experimented with the use of plasticizer to reduce w/b ratio, but this attempt did not lead to the desired improvement of mechanical properties. Cohesion between burnt bricks and mortar containing plasticizer was really poor and it was decided to exclude these mortar samples from further tests. The amount of aggregates was based on previous studies [9, 40, 41] and results of micromechanical modeling [23]. Summarized composition of all tested mortar specimens is shown in Table 2.1.

It is important to note that the mortar mixtures containing crushed brick particles retain

Table 2.1: Mass ratios of individual constituents.

mix	binder			aggregate		water / dry mass (water / binder)
	lime	Portland cem.	metakaolin	sand	crushed bricks	
LC-S	0.7	0.3	–	3	–	0.175 (0.704)
LMK-S	0.7	–	0.3	3	–	0.180 (0.714)
LMK-SCB	0.7	–	0.3	1	1.5	0.250 (0.875)
L-SCB	1.0	–	–	1	1.5	0.320 (0.940)

more water than with sand only (see the water / dry mass ratio records in Table 2.1). This phenomenon is caused by open porosity system within the brick fragments. Water absorbed by brick particles can be responsible for a future development of hydraulic phases in the pozzolan-rich mortars, and consequent strength and stiffness gain [30]. We also tried to prepare mortar sample containing only aggregate in form of crushed bricks, but the enormous shrinkage and bad cohesion with the brick substrate were unacceptable.

2.1.2 Acquisition of Basic Material Parameters

The basic material parameters were obtained from the basic material tests following the methods in ČSN EN 1015-11 [42]. These experiments, namely three-point bending and compression tests, were carried out to obtain primarily tensile strength f_t and compression strength f_c . Acquisition of these parameters was also important in the case of common fired clay brick as a masonry unit used in the full-scale tests of columns mentioned in further text. Beside of these tests, the dynamic Young's modulus, E_{dyn} , was assessed by means of the resonance method. Fracture energy, G_f , was obtained by the interpretation of results of three-point bending tests.

2.1.2.1 Samples Preparation and Curing

After mixing all mortar components in the pre-determined ratios, the mixing process was accomplished according to ČSN EN 1015-2 [43] and at least six specimens from each batch were cast into $160 \times 40 \times 40$ mm prismatic molds and compacted using a shaking table to get rid of excessive air bubbles. Specimens were removed after 48 hours from the molds and stored in the laboratory conditions with constant temperature 20 ± 1 °C and relative humidity ranging between 60 and 80 % for 90 days. During the hardening process, longitudinal shrinkage of samples was measured. Total averaged values after 90 day period are: LMK-SCB – 0.64 %, LC-S – 0.71 %, LMK-S – 0.83 %, L-SCB – 1.10 %. In case of brick six $140 \times 40 \times 40$ mm prisms were cut from the common bricks with dimensions $290 \times 140 \times 65$ mm produced in brick plant Štěrboholy, Czech Republic.

2.1.2.2 Resonance Method

Non-destructive resonance method provides the determination of the dynamic elastic properties of elastic materials. The method is based on the assumption that the measured specimens exhibit specific mechanical resonant frequencies that are predetermined by the elastic modulus,

mass and geometry. This method is specifically appropriate for materials that are homogeneous and isotropic while not satisfactory for specimens that have cracks or voids forming major discontinuities in the specimen [44, 45].

Resonance method was chosen to access the dynamic Young's modulus, E_{dyn} , of both types of samples – mortars and brick. This procedure was chosen to overcome the inconvenience connected to the measurement of the static Young's modulus arising from the load-dependent compliance of the loading frame during the destructive tests. According to Malaikah et al. [46] the discrepancy between dynamic and static moduli measured on the same sample, respective material, within the range $\pm 10\%$.

Young's modulus calculation is based on the equation for a longitudinal vibration of the tested beam with a continuously distributed mass and free-free boundary conditions, following

$$E_{\text{dyn}} = \frac{4Lmf_1^2}{bt}, \quad (2.1)$$

where L is the length of the specimen [m], m is the mass of the specimen [kg], f_1 is the first fundamental longitudinal resonant frequency of the specimen [Hz], b is the width [m] and t is the thickness of the specimen [m]. Impact was applied by the impact hammer and on the other side acceleration transducer was attached (Figure 2.2a) – Brüel & Kjær measurement device was used. Evaluation of results was carried out by the special PULSE ReflexTM software – see Figure 2.2b presenting the plot of FFT frequency response of the tested sample with highlighted first fundamental resonant frequency. All measured values of dynamic elastic modulus for each sample are summarized in Table 2.2.

Table 2.2: Calculated values of dynamic Young's moduli, in [GPa].

sample	LC-S	LMK-S	LMK-SCB	L-SCB	brick
a	6.97	7.19	10.01	2.55	15.01
b	7.17	7.76	10.03	2.09	14.12
c	7.06	7.43	10.22	2.34	13.75
d	7.22	7.33	9.31	2.67	15.26
e	6.89	8.12	10.05	2.23	13.92
f	7.12	7.22	9.95	2.16	14.37

The obtained values of the dynamic Young modulus were used for scaling the displacements when evaluating the load-displacement diagrams provided by the three-point bending and uniaxial compression tests. Scaling were done by the recalculations of measured displacements in the ratio of Young's moduli by the following equation

$$d_r = \frac{E}{E_{\text{dyn}}} d_m, \quad (2.2)$$

where d_r is recalculated displacement [m], E is the tangential Young's modulus from load-displacement diagram obtained during the destructive tests [Pa], E_{dyn} is the dynamic Young's modulus [Pa], and d_m is measured displacement during the tests [m].

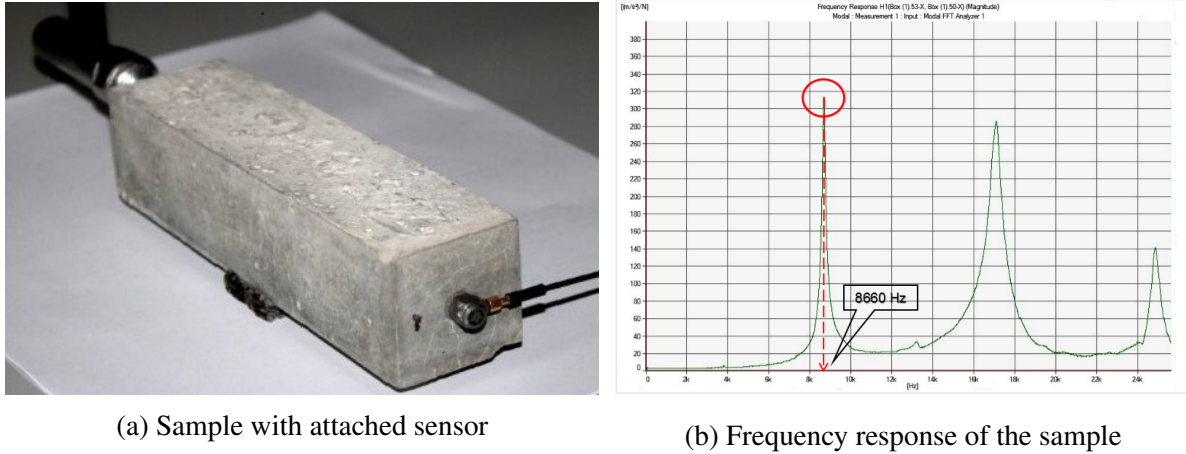


Figure 2.2: Processing of modal analysis by resonance method.

2.1.2.3 Three Point Bending

The three point bending flexural test provided values of maximum tensile strength by the following equation

$$f_t = \frac{3FL}{2bt^2}, \quad (2.3)$$

where F is the maximum force achieved during the test [N] and L is the span between supports [m]. Displacement-controlled three-point bending tests were performed on the unnotched $160 \times 40 \times 40$ mm beams with distance between supports equal to 100 mm. The loading of simply supported beams was accomplished in the midspan and the rate of loading was 0.025 mm/min in order to capture the descending part of the load-displacement diagram and monitored using MTS Alliance RT 30 kN load cell. The three-point flexure fixture produces its peak stress at the specimen in mid-point with reduced stress elsewhere.

Fracture energy calculations were based on the following formula

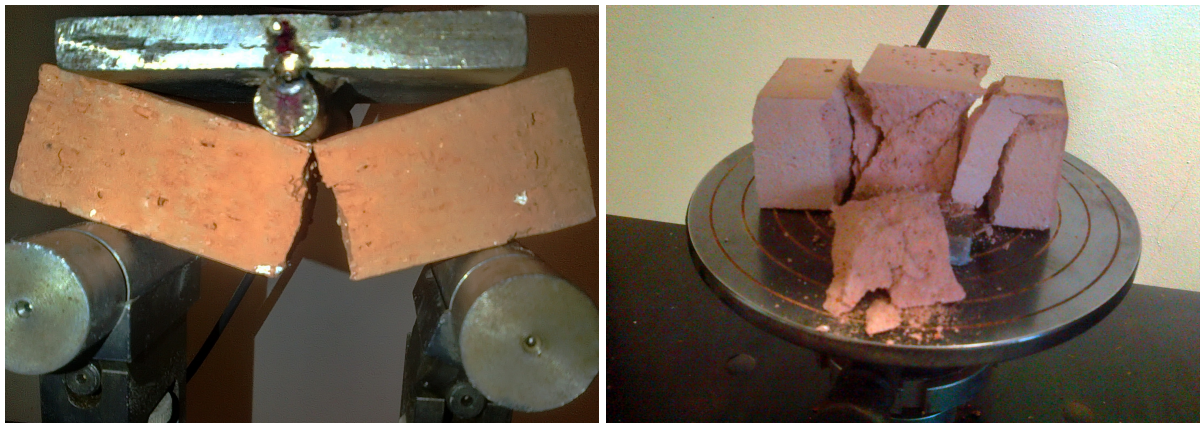
$$G_f = \frac{g_f}{A_c} = \frac{\int_0^\infty F(d_r) dd_r}{bt}, \quad (2.4)$$

where g_f is the area under the rescaled force-displacement diagram obtained by Equation (2.2) [J] and A_c is the cross section of the tested specimen [m²]. In Figure 2.3a the test setup and state of the specimen after the test is illustrated.

2.1.2.4 Uniaxial Compression

The compression test was utilized to investigate the behavior of the material when subjected to uniaxial compression. The test provides two basic material parameters – compressive strength, being the ratio between the maximum force and area of the loaded side, and tangent modulus. Since the Young's modulus was determined using the resonance method, only compressive strength was determined based on results of the uniaxial compression test.

The test was carried out on cubic $40 \times 40 \times 40$ mm specimens, cut off the halves of the cracked beams from the three-point bending tests, and the same device as for the three-point



(a) Sample of brick after three point bending test (b) Sample of mortar after compression test

Figure 2.3: Sample of brick as documentation of three-point-bending test and sample of LMK-SCB mortar as an example of compression test.

bending tests was used. A uniform force distribution was accomplished by steel washers, and the load was applied on the lateral sides (these sides were in contact with the mold during the preparation of specimens) in order to ensure perfectly smooth and parallel contact. To prevent skewing of results by the presence of bending moment, the load was applied through the ball joint assembly (Figure 2.3b). The loading was displacement-controlled with the rate of 0.3 mm/min.

Maximum compression strength was calculated by the following equation

$$f_c = \frac{F_{\max}}{A}, \quad (2.5)$$

where A is the area [m^2] and F_{\max} is the maximum applied load [N].

2.1.2.5 Adhesive Strength

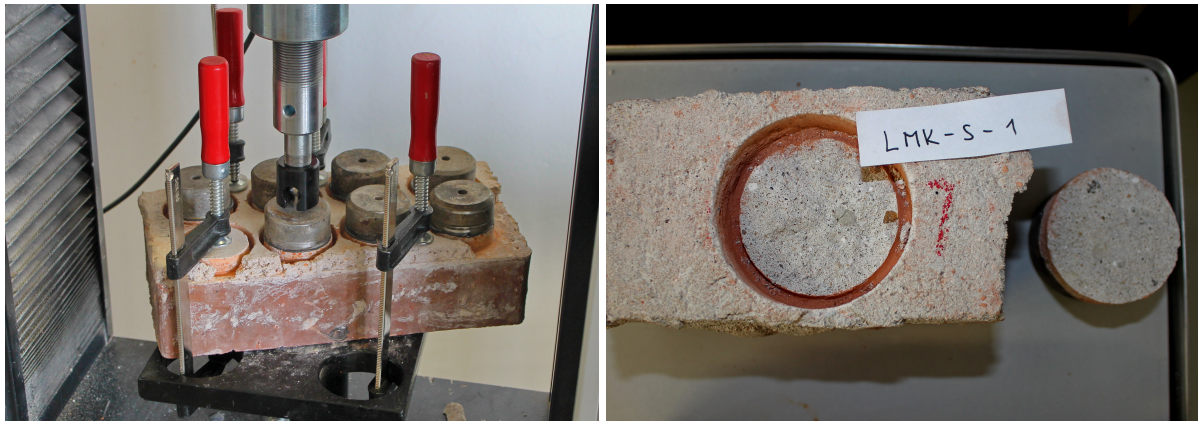
The test of adhesive strength strictly followed the norm ČSN EN 1015-12 [47]. The adhesive strength f_u was determined as the maximum tensile stress applied by a direct load perpendicular to the surface of the mortar on a substrate – in our case fired clay brick. The tensile load was applied by means of a pull-head plate with diameter of 50 mm, glued to the test area of the mortar surface. The adhesive strength of the mortar-brick interface was determined according to the following equation

$$f_u = \frac{F_u}{A}, \quad (2.6)$$

where F_u is the failure load [N] and A is the test area of the cylindrical loading plates [m^2].

In total six specimens representing all the tested mortars, specified in Table 2.1, were prepared. Preparation consisted of placing 10 mm thick mortar layers on the fired clay bricks, followed by curing for 7 days in a sealed polyethylene bags at a temperature 20 ± 1 °C and then removed from the bags and stored for another 80 days in laboratory conditions as described in Section 2.1.2.1. Storing in the plastic bags was important to prevent fast drying responsible for shrinkage cracking. Second step consisted of separating the mortar circles of a diameter equal

to 50 mm by a diamond trepanner, and gluing the aluminium plates onto the separated mortar discs by epoxy resin. Loading was displacement-controlled with the rate of loading 0.03 mm/s and was accomplished by the same machine as in case of three-point bending and compression tests. Figure 2.4a shows the configuration during the experiment and Figure 2.4b documents the typical fracture pattern – all patterns were in the layers of mortar, that means the values are equal to theoretical tensile strength of mortars. Table 2.3 shows the results of the experiments – calculated values of tensile strength of mortars at the interface.



(a) Samples of LMK-SCB during the testing

(b) Sample after test with typical fracture pattern

Figure 2.4: Execution of adhesive strength tests.

Table 2.3: Calculated values of tensile strength of mortars.

sample	LC-S	LMK-S	LMK-SCB	L-SCB
interface strenght [MPa]	0.606	1.442	1.838	0.211

2.1.3 Results

In this section a comparison of individual force-displacement diagrams for all destructive tests is presented. Figure 2.6 provides the comparison of behavior of individual mortar mixes during the compression tests while Figure 2.7 during the three-point-bending tests. Note that the staircase character of Figures 2.7b and 2.7c is caused by the inappropriate evaluating of the displacements by the measuring device used during the tests. In Figure 2.5 results for individual tests of brick are presented.

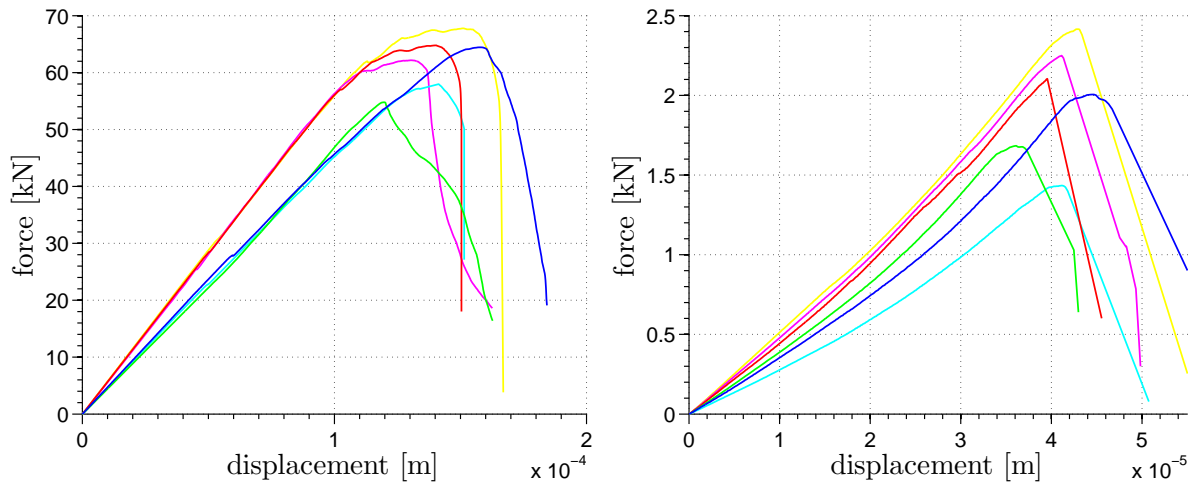


Figure 2.5: Individual force-displacement diagrams for compression (left) and three-point-bending (right) tests of brick.

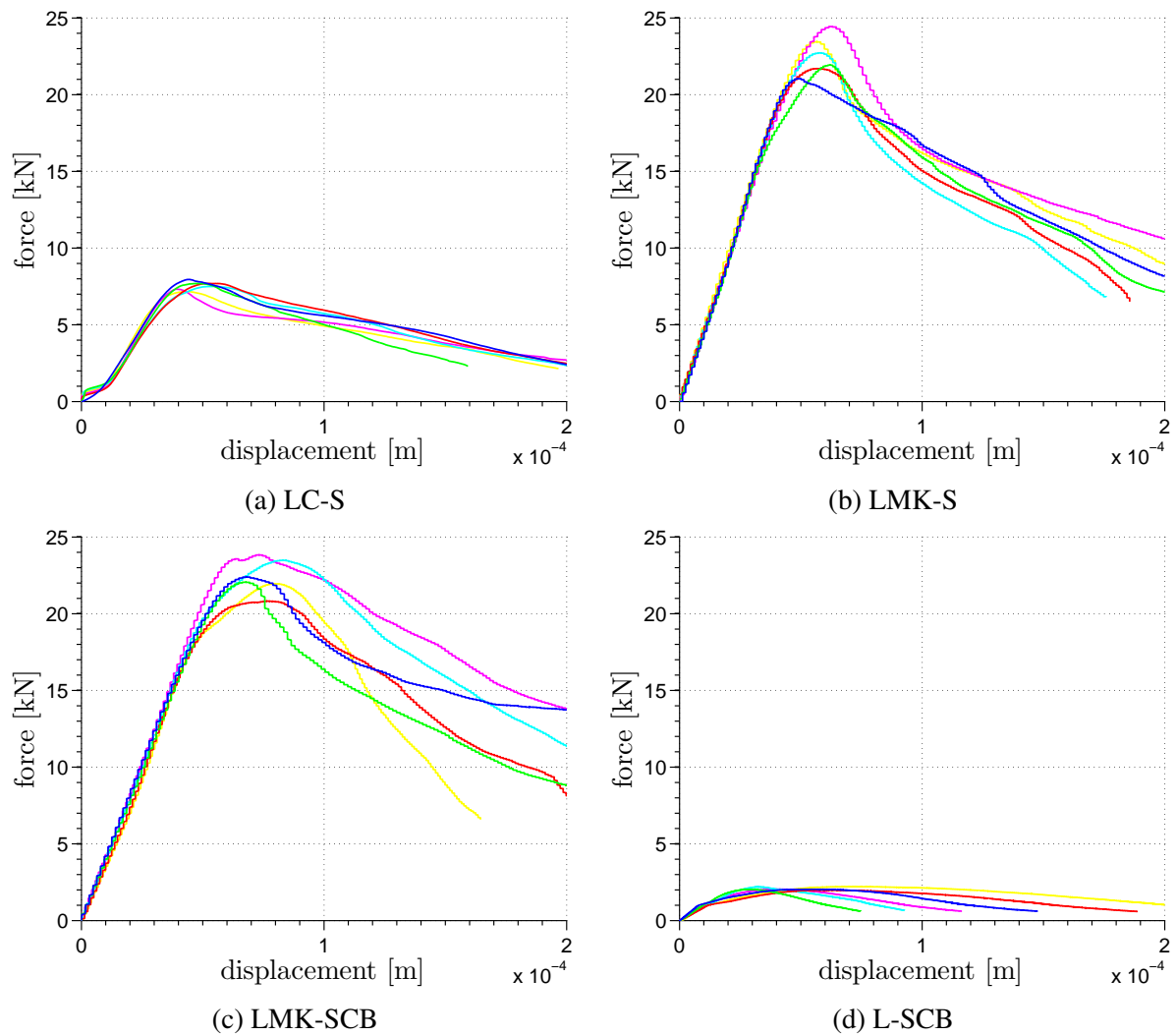


Figure 2.6: Individual force-displacement diagrams for compression tests of mortars.

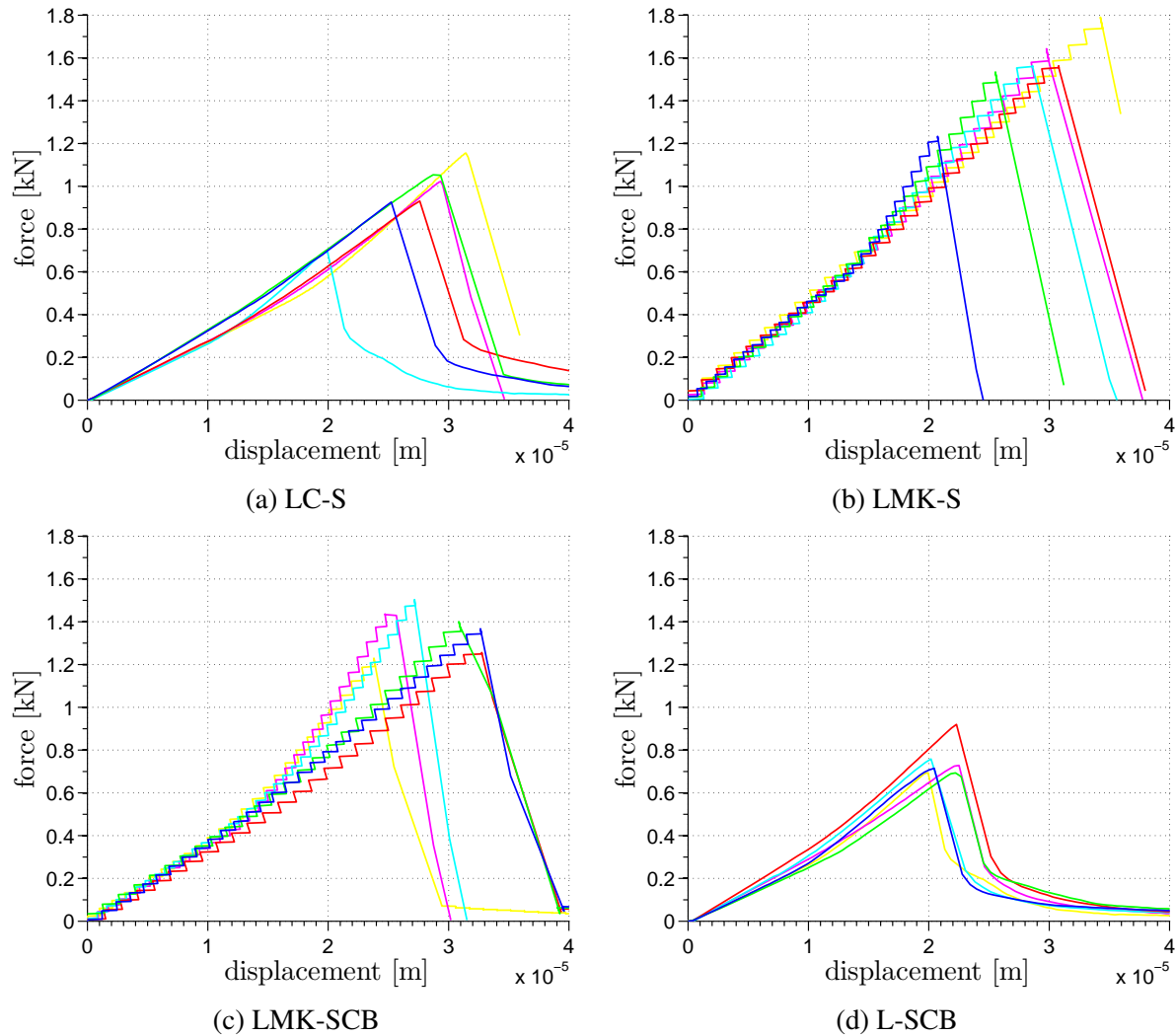


Figure 2.7: Individual force-displacement diagrams for three-point-bending tests of mortars.

2.2 Experimental Testing of Masonry Piers

2.2.1 Specimen Preparation

Geometry of tested samples is described by Figure 2.8. Common fired clay bricks from Bratronice brick plant with standard dimensions mentioned in Section 2.1.2.1 were used. The thickness of bed joints was equal to 15 mm (15 mm high plastic pads were placed in the corners to maintain the constant joint thickness) while vertical joints were 10 mm thick. Bricks were arranged in five layers to make a proper cross bond. The study was focused only on the influence of the mortar in joints; the geometry, loading, boundary conditions and the masonry material (clay bricks) were same for all tested piers. Piers were stored for 90 days in laboratory conditions at constant temperature 20 ± 1 °C and relative humidity ranging between 60 and 80 %. Two weeks before tests 10 mm thick layers were applied on the column caps to ensure parallel surfaces during the tests – anhydrite floor screed with 20 MPa compression strength was used for its

easy workability and for the self-leveling ability.

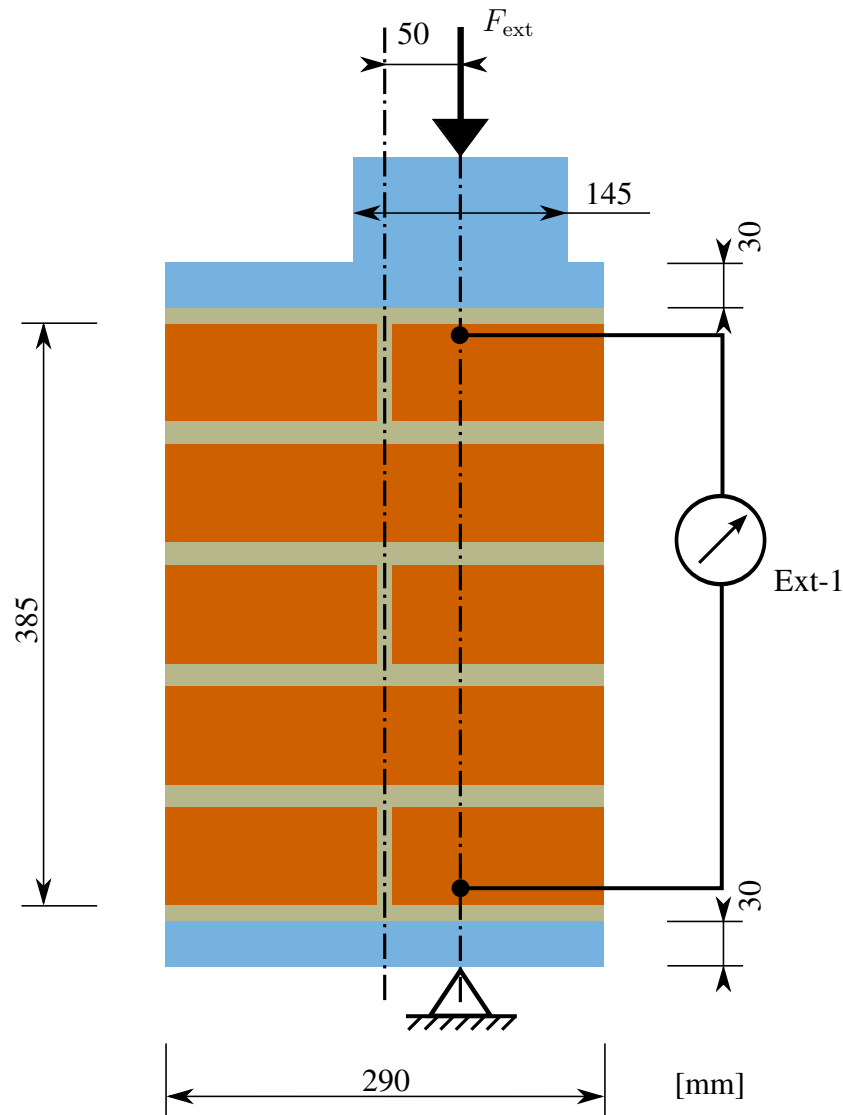


Figure 2.8: Loading of the tested piers and placement of virtual extensometers.

2.2.2 Destructive Testing

The pier loading was accomplished by means of a hydraulic accumulator with 1 MN loading capacity. Load was distributed through the 30 mm thick steel plates to ensure a uniform distribution of stresses and was applied with 5 cm eccentricity. Every pier was fixed on its position using a special steel frame that enables free rotation of pier stub in perpendicular direction from eccentricity. The masonry piers were subjected to a displacement-controlled quasi-static compression to introduce a combination of bending and compression. 1 mm/min loading rate was chosen in order to capture the descending part of the force-displacement diagram after the loss of pier integrity. For measuring different displacement on the less and more loaded side pair of extensometers was attached on each side. The measured displacement was averaged and used a comparison with optical measurements by means of DIC, see Figure 2.12a.

In order to capture the failure mechanisms a full-field digital image correlation (DIC) method was employed. DIC, or better DIC-2D, can provide detailed information about the development of in-plane deformation field, major strain localizations, and evolution of cracks. Full field measurement by means of DIC allows us to track the strain-field over the region of interest (ROI) and capture the damage initiation and progression until the complete loss of structural integrity [48]. Such strain-field measurement cannot be accomplished with ordinary extensometers or strain-gauges attached at predescribed discrete locations.

2.3 Digital Image Correlation

2D Digital Image Correlation (DIC) method was employed for the measurement and evaluation of the deformation fields. Such approach allowed to compare the experimentally acquired data with the results of the FE simulations. The method is particularly suitable for capturing the localization phenomena such as localization of plastic strains into the compliant mortar joints or development of cracks.

DIC was firstly mentioned in the work of Yamaguchi [49] and Peters and Ranson [50], who were among the first to introduce its principles. DIC is widely used because of its low requirements on equipment, easy application, wide range of measurement resolution and, above all, high accuracy. In principle, DIC is an optical measurement based on digital image processing and numerical computing. It directly provides information about the full-field displacement and deformation fields by comparing the digital images of a surface texture or a stochastic pattern applied artificially on the sample [51, 52] taken during the destructive test.

In the beginning DIC suffered from insufficient computational power and also ineffective evaluating algorithms – these reasons led to investigating only small Regions of Interests (ROIs) (in the order of millimeters), but in the last years efficient numerical methods [53, 54] together with a sufficient computational power allowed to use DIC in case of macro problems, such as formation of cracking various patterns in masonry walls [55, 56], to investigate deformation of textiles [57] or fatigue failure of polymer materials [58].

In our study, we used an open source software Ncorr v1.1 [59] for the evaluation of the displacement and deformation fields. The program was developed by Justin Blaber on Georgia Institute of Technology and post-processing of results was carried out by Ncorr_post tool [60]. Both programs operate in MATLAB [61] environment and are platform independent – able to work under the Windows operating systems as well as Linux systems.

2.3.1 DIC principles

The main idea of DIC is to find a one-to-one correspondence between material points in the reference and current image. This is accomplished by taking small subsections of the reference image, called subsets, and determining their locations in the current image. For each subset, we obtain displacement and strain information through the transformation used to match the location of the subset in the current (deformed) image. Several subsets are selected in the reference configuration, often with a spacing parameter to reduce computational cost (also note that subsets typically overlap as well). The calculation output is provided in the form of a

grid containing displacement and strain information with respect to the reference configuration. The strain/displacement fields can be then either reduced or interpolated to form a continuous strain/displacement field.

Subsets are essentially a group of coordinate points, the main idea of subsets in the reference and current image is shown in Figure 2.9, where the reference image "Ref" is denoted as and "Cur" is the current (deformed) image.

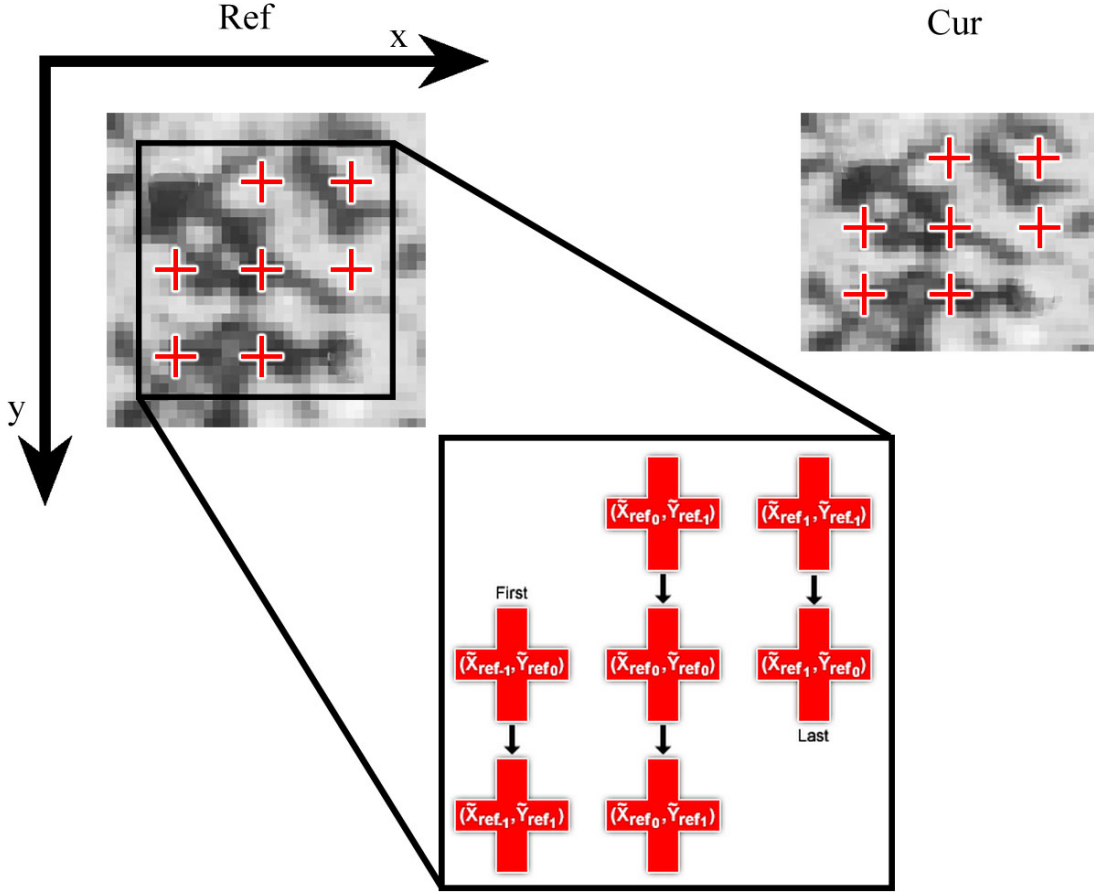


Figure 2.9: The reference and current image, the subset's coordinates are shown as red crosses.

It is possible to establish \mathbf{S} as a set which contains all of the subset points

$$\mathbf{S} = \{(-1, 0), (-1, 1), (0, -1), (0, 0), (0, 1), (1, -1), (1, 0)\}, \quad (2.7)$$

given as an example in Figure 2.9. The transformation of the initial reference subset points to the current location is typically constrained to a linear, first-order displacement mapping function and given as

$$\begin{aligned} \tilde{x}_{cur,i} &= x_{ref,i} + u_{rc} + \frac{\partial u}{\partial x_{rc}}(x_{ref,i} - x_{ref,c}) + \frac{\partial u}{\partial y_{rc}}(y_{ref,j} - y_{ref,c}), \\ \tilde{y}_{cur,j} &= y_{ref,j} + v_{rc} + \frac{\partial v}{\partial x_{rc}}(x_{ref,i} - x_{ref,c}) + \frac{\partial v}{\partial y_{rc}}(y_{ref,j} - y_{ref,c}), \end{aligned} \quad (2.8)$$

where $(i, j) \in \mathbf{S}$, $x_{ref,i}$ and $y_{ref,j}$ are the x and y coordinates of an initial reference subset point, $x_{ref,c}$ and $y_{ref,c}$ are the x and y coordinates of the center of the initial reference subset, $\tilde{x}_{cur,i}$

and $\tilde{y}_{\text{cur},j}$ are the x and y coordinates of a final current subset point and $\partial u/\partial x_{\text{rc}}$, $\partial u/\partial y_{\text{rc}}$, $\partial v/\partial x_{\text{rc}}$, $\partial v/\partial y_{\text{rc}}$ are displacement gradient components and u , v are translations of the center of the subset image in the x and y directions, respectively. The subscript denotation "rc" used in Equation (2.8) indicates that the transformation is from the reference to the current coordinate system.

A general form of the displacement-deformation matrix is considered as follows

$$\mathbf{p} = \left\{ u \quad v \quad \frac{\partial u}{\partial x} \quad \frac{\partial u}{\partial y} \quad \frac{\partial v}{\partial x} \quad \frac{\partial v}{\partial y} \right\}^T \quad (2.9)$$

and the geometrical meaning of individual entries is illustrated in Figure 2.10. Any linear combination of the 6 parameters shown in Figure 2.10 could be described by a warp function w , which is used to describe the deformations of subset. Equation (2.8) can be also rewritten into the matrix form

$$\xi_{\text{ref},c} + w(\Delta\xi_{\text{ref}}, \mathbf{p}_{\text{rc}}) = \begin{Bmatrix} x_{\text{ref},c}^T \\ y_{\text{ref},c}^T \\ 1 \end{Bmatrix} + \begin{bmatrix} 1 + \frac{\partial u}{\partial x_{\text{rc}}} & \frac{\partial u}{\partial y_{\text{rc}}} & u_{\text{rc}} \\ \frac{\partial v}{\partial x_{\text{rc}}} & 1 + \frac{\partial v}{\partial y_{\text{rc}}} & v_{\text{rc}} \\ 0 & 0 & 1 \end{bmatrix} * \begin{Bmatrix} \Delta x_{\text{ref}}^T \\ \Delta y_{\text{ref}}^T \\ 1 \end{Bmatrix}, \quad (2.10)$$

where ξ is an augmented vector which contains the x and y coordinates of subset points, Δx and Δy are the distances between the subset points and the center of the subset and w is a warp function. Also it is necessary to allow the reference subset to deform within the reference configuration, as shows Equation (2.11).

$$\begin{aligned} \tilde{x}_{\text{ref},i} &= x_{\text{ref},i} + u_{\text{rr}} + \frac{\partial u}{\partial x_{\text{rr}}}(x_{\text{ref},i} - x_{\text{ref},c}) + \frac{\partial u}{\partial y_{\text{rr}}}(y_{\text{ref},j} - y_{\text{ref},c}), \\ \tilde{y}_{\text{ref},j} &= y_{\text{ref},j} + v_{\text{rr}} + \frac{\partial v}{\partial x_{\text{rr}}}(x_{\text{ref},i} - x_{\text{ref},c}) + \frac{\partial v}{\partial y_{\text{rr}}}(y_{\text{ref},j} - y_{\text{ref},c}), \end{aligned} \quad (2.11)$$

where $\tilde{x}_{\text{ref},i}$ and $\tilde{y}_{\text{ref},j}$ are the x and y coordinates of the final reference subset point. The subscript denotation "rr" is meant to represent the transformation from the reference coordinate system to the reference coordinate system.

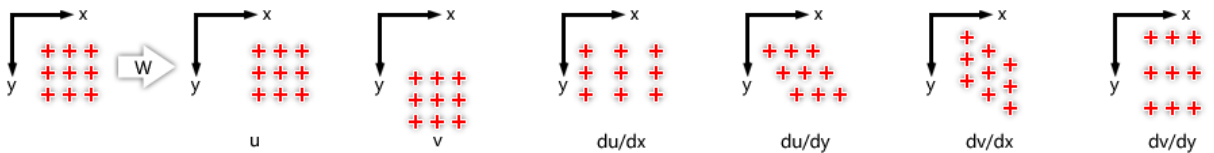


Figure 2.10: Linear transformations for subset coordinates, reproduced from [2].

The purpose of the analyzing scripts in Ncorr is to find the optimal \mathbf{p}_{rc} when $\mathbf{p}_{\text{rr}} = 0$ such that the evaluated coordinates $\tilde{x}_{\text{ref},i}$ and $\tilde{y}_{\text{ref},j}$ preferably match the coordinates $\tilde{x}_{\text{cur},i}$ and $\tilde{y}_{\text{cur},j}$.

The next major step is to define a geometric similarity between the reference subset and the current subset. This is done by comparing gray scale values between the reference subset points

with the gray scale values at the final subset points. In Equations (2.12) and (2.13), there are two metrics which are used by Ncorr, but there are also alternative equations [54].

$$C_{CC} = \frac{\sum_{(i,j) \in S} (f(\tilde{x}_{ref,i}, \tilde{y}_{ref,j}) - f_m)(g(\tilde{x}_{cur,i}, \tilde{y}_{cur,j}) - g_m)}{\sqrt{\sum_{(i,j) \in S} [f(\tilde{x}_{ref,i}, \tilde{y}_{ref,j}) - f_m]^2 \sum_{(i,j) \in S} [g(\tilde{x}_{cur,i}, \tilde{y}_{cur,j}) - g_m]^2}}, \quad (2.12)$$

$$C_{LS} = \sum_{(i,j) \in S} \left[\frac{f(\tilde{x}_{ref,i}, \tilde{y}_{ref,j}) - f_m}{\sqrt{\sum_{(i,j) \in S} [f(\tilde{x}_{ref,i}, \tilde{y}_{ref,j}) - f_m]^2}} - \frac{g(\tilde{x}_{cur,i}, \tilde{y}_{cur,j}) - g_m}{\sqrt{\sum_{(i,j) \in S} [g(\tilde{x}_{cur,i}, \tilde{y}_{cur,j}) - g_m]^2}} \right]^2. \quad (2.13)$$

These equations, widely known as correlation criteria, involve f and g , the reference and current image functions, or rather gray scale values corresponding to the specified (x,y) point and f_m and g_m are the mean gray scale values of the reference and current subset.

$$f_m = \frac{\sum_{(i,j) \in S} f(\tilde{x}_{ref,i}, \tilde{y}_{ref,j})}{n(\mathbf{S})}, \quad (2.14)$$

$$g_m = \frac{\sum_{(i,j) \in S} g(\tilde{x}_{cur,i}, \tilde{y}_{cur,j})}{n(\mathbf{S})},$$

where $n(\mathbf{S})$ is the number of elements in \mathbf{S} .

Optimal \mathbf{p}_{rc} is found by the use of iterative nonlinear least squares optimization scheme which minimizes Equation (2.13). Nonlinear optimization scheme mainly uses the inverse compositional Gauss-Newton method (IC-GN) which is more faster than commonly used forward additive Gauss-Newton method (FA-GN) [54]. Full descriptions of these methods is complex and is beyond the scope of this work.

After the evaluation of displacement field at all discrete points, the displacements are interpolated to obtain continuous field. Obtaining the strain field is more complex because it involves differentiation, which is sensitive to noise. The noise, respectively noisy displacements are always presented which is caused by many effects. These are for instance small change of the light conditions during the test, compressing methods used during the *RAW* to *jpg* conversion or resizing of images. Noise in the displacements field magnifies the errors in the strain field. The type of strain field calculated by Ncorr is Green-Lagrangian strain, which is obtained using the four displacements gradients as demonstrated by the following equations:

$$\varepsilon_{xx} = \frac{1}{2} \left(2 \frac{\partial u}{\partial x} + \left(\frac{\partial u}{\partial x} \right)^2 + \left(\frac{\partial v}{\partial x} \right)^2 \right),$$

$$\varepsilon_{xy} = \frac{1}{2} \left(\frac{\partial u}{\partial y} + \frac{\partial v}{\partial x} + \frac{\partial u}{\partial x} \frac{\partial u}{\partial y} + \frac{\partial v}{\partial x} \frac{\partial v}{\partial y} \right), \quad (2.15)$$

$$\varepsilon_{yy} = \frac{1}{2} \left(2 \frac{\partial v}{\partial y} + \left(\frac{\partial u}{\partial y} \right)^2 + \left(\frac{\partial v}{\partial y} \right)^2 \right).$$

The displacement gradients are directly obtained through the IC-GN scheme, but the noisy values have to be smoothed before calculating the strain field. Idea implemented in the Ncorr is

to evaluate the displacement gradients directly from the displacement field according to Equations (2.15) [62], ignoring the values provided by IC-GN scheme.

The DIC procedure basically consists of the following steps:

1. Preparation of stochastic contrast pattern on the investigated column surface.
2. Taking photos of the investigated surface with a digital camera during the destructive experiment.
3. Processing and adjusting the photos.
4. Evaluating the photos by the DIC software to obtain full-field strains.

2.3.2 Contrast Pattern

The DIC technique relies on a contrasting speckle pattern applied on the surface of the test specimen [52, 63, 64, 65]. This pattern can be in the form of a natural texture or it can be artificially applied. The pattern quality has a dominant influence on the spatial resolution and accuracy of DIC results. In general, to achieve effective correlation, the pattern must be random, isotropic, i.e. must not exhibit a bias to one orientation, and highly contrasting, i.e. must show dark blacks and bright whites [66]. In addition to the above requirements, speckles should be neither too small nor too large. If the pattern is too large, we may find that certain subsets are just a black or white fields. This does not allow to make a good match [52]. Such issue could be solved by increasing the subset size, but at the cost of the spatial resolution. On the other hand, too small speckles can cause the aliasing effect resulting in images that often show a pronounced Moiré pattern in the measurement results [66]. As a rule, speckles should be 3-8 pixels in size to achieve effective correlation [67].

In our case a common white wall-paint was used to create a white background. After drying of the white paint black dots were applied using spray. It is necessary to have the white pattern sufficiently bonded to the surface and keep the paint layer thin enough to see the initial cracking – this is not ensured for example by synthetic varnishes or enamels [64]. Final pattern with a real scale is shown in Figure 2.11.

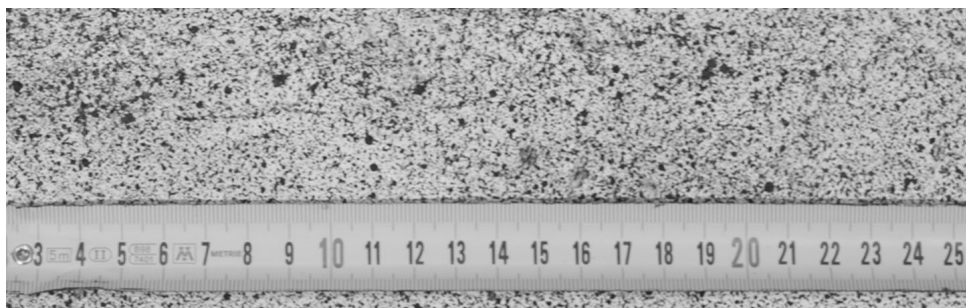


Figure 2.11: Artificial stochastic contrast pattern.

2.3.3 Acquisition of Input Images

For purpose of image acquisition a high-resolution digital DSLR camera was used – Canon EOS 70D equipped with EF-S 18-135mm f/3.5-5.6 IS STM zoom lens. Canon 70D has a APS-C sensor with crop factor 1.6 and its size is 22.5×15.0 mm with effective 20.2 MP resolution, yielding the maximum photo size 5472×3648 px. Camera was fixed on a tripod in 1 m distance. Very high attention was paid to the placement of the camera.

To avoid distortion of results, the camera had to be placed parallel to the specimen surface and in line with the specimen axes. The distance was chosen in such a way to minimize the lens distortion effect [54] – 55 mm focal length was set ($55 \times 1.6 = 88$ mm equal to full-frame). The light sensitivity of the camera chip, ISO number, was manually set to 100 to avoid excessive noise. Perfect light conditions (ensured by the pair of halogen lights, with power of 250 W of each) allowed to use short exposure time – $1/125$ and aperture number was chosen to obtain proper exposition of images – $f/8.0$. These settings were kept constant for all images in a series. For each specimen one reference image with a real scale was shot prior to its loading. Than 5-second time interval was set equally for all tested specimens and the start of photo-sequence was synchronized with the start of loading to proper match of force-displacement diagrams measured by hydraulic accurator. Totally 210 – 260 images of one pier were taken to document the whole process of pier loading until its complete failure. RAW file format of files was chosen to obtain uncompressed quality of digital pictures.



(a) Contrast pattern and attached extensometers

(b) Experiment setup with DSLR camera

Figure 2.12: Experimental testing of columns.

2.3.4 Processing of Acquired Images

The recorded digital images in RAW (.CR2) format were processed in Adobe Photoshop Lightroom 5 64-bit software. Firstly, transformation into 8-bit grey scale was done and then contrast, exposition and tint parameters were slightly changed to obtain the best possible quality of contrast pattern. The last step of processing consisted of cropping the images to save the computer memory. The changed values were saved and applied on all pictures from one batch. Export into .jpg format was carried out by the same software, with resizing at the same time because of insufficient computational power of the available computer. Bigger size of photos, or more precisely their high resolution, results in higher computational cost [54]. The original size of photos was 3648×5472 px, cropped images 3168×4752 px and resized photos were in scale of 50 %, 1584×2376 px and the resulting DIC real scale resolution was equal to 0.202 mm/pixel. Export was done with 60 % quality of .jpg compression. The amount of compression is usually the main source of low precision or rather low sensitivity of DIC in comparison with ordinary contact measurements. The demonstration of image compression is provided in Figure 2.13. In particular the contrast between very low 5 %, used 60 % and very similar 100 % compression. It is obvious that during the high level of compression an unadvisable pixelation effect occurs – pixels are grouped into periodic matrices, which is unsuitable for the needs of DIC. The file size of the exported images was around 2.70 MB per single file.

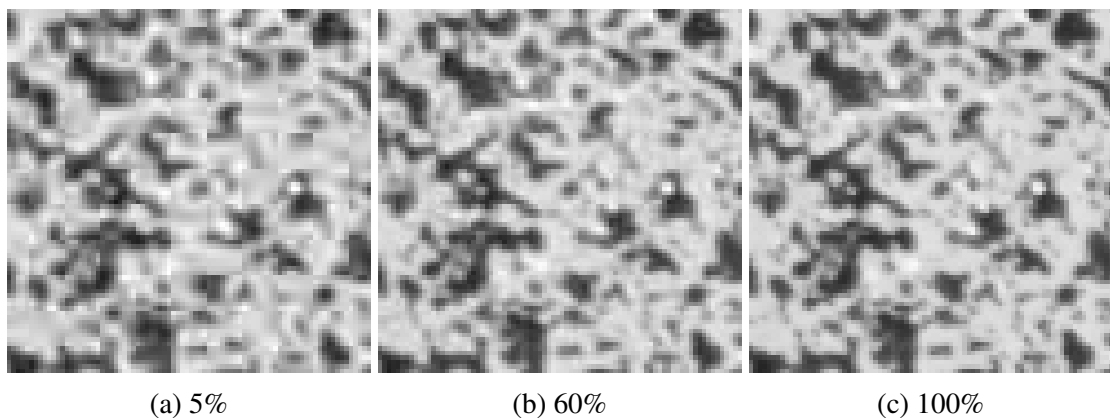


Figure 2.13: Comparison of .jpg compression ratio.

2.3.5 DIC Processing

DIC processing was carried out by Ncorr program to which the author provides a full manual [68], but at least the generalized workflow of program is mentioned in the present thesis. Main steps of DIC analysis in Ncorr consist of:

1. Setting of Reference Image

Undeformed, reference image has to be loaded first. Ncorr provides two ways how to set the image. One is through the Ncorr GUI by choosing the picture as a file, the other way is directly in MATLAB terminal by loading the matrix of type doubles, which contains gray-scale values.

2. Setting of Current Images

Current or deformed images are loaded next. Ncorr enables two ways of loading the images. Options of "Load All" or "Load Lazy". Loading of all images can be problematic when a large number of images needs to be processed, because all of these loaded images are stored in the RAM memory. Lazy loading stores only the path to the folder with images and during the DIC analysis images are loaded one by one. Program also needs to have an order in the batch of files, so it is recommended to rename the images into the following format:

$$name_#\text{.ext},$$

where *name* is the custom name of the image set and *#* is the number of loading step associated with the image and *ext* is an image extension. Ncorr supports *.jpg*, *.tif*, *.png* and *.bmp* files. Overall main program menu window is shown in Figure 2.14.

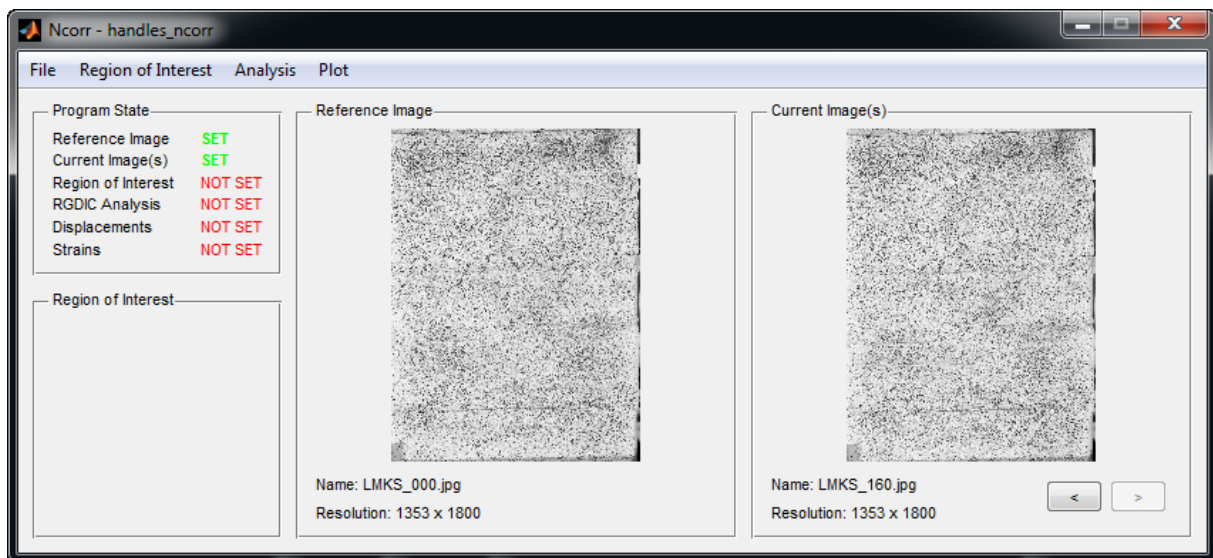


Figure 2.14: Main menu window in Ncorr.

3. Setting Region of Interest

There are three ways how to set ROI: in Ncorr menu by loading the ROI image, to draw it directly in Ncorr GUI environment or by loading the matrix of logical values of the same size as the reference image.

ROI image is the image processed in some image processing software – desirable ROI is represented by white color (255 grayscale value) and unclaimed area is black (0). Drawing in GUI is simple by putting the polygon on the desired area.

4. Setting DIC Parameters

The main evaluating algorithm in Ncorr is based on the Bi-Pan's RG-DIC framework (for more information see [2, 54]) and several key parameters of DIC analysis have to be set up, example of window with settings is provided in Figure 2.15.

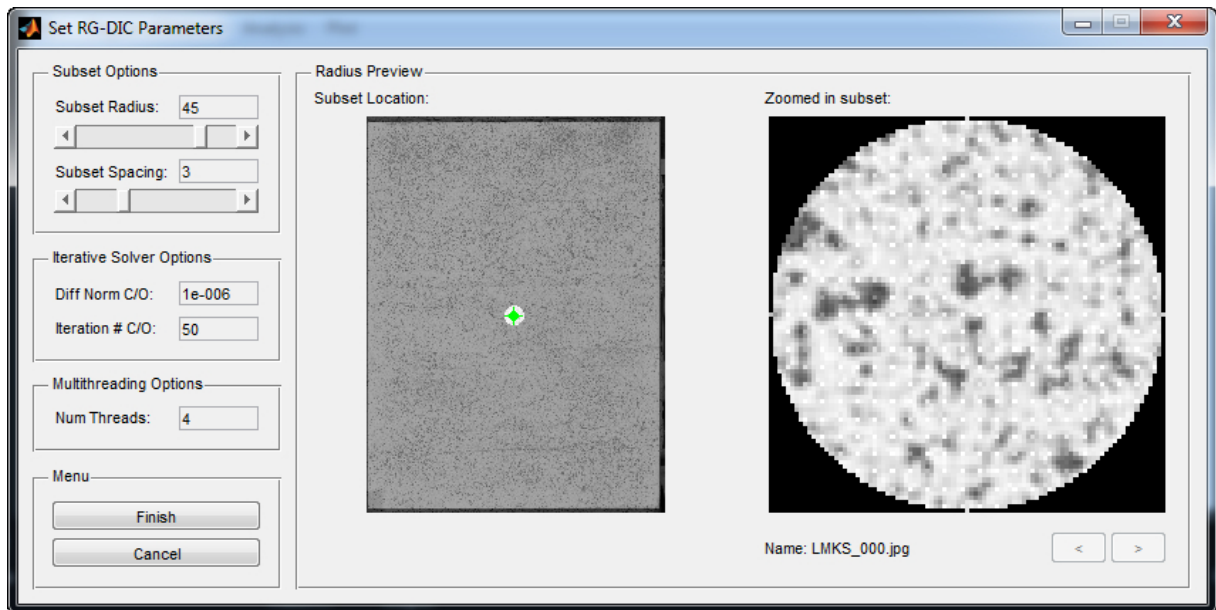


Figure 2.15: Window with settings of DIC in Ncorr.

Subset Options are the main components of DIC analysis – subset size (subset radius) and subset spacing. The main idea is to select smallest subset as it possible to obtain non-noisy displacement data, but too small subsets in high-resolution ROI leads to demanding calculations, which require very high computational power.

Iterative Solver Option defines the criteria to terminate iterations. Two criteria are used – norm of the difference vector or maximal number of iterations. Increasing the norm or reducing the number of iteration number can lead to much faster analysis, but result in less precise results of DIC.

Multithreading Options allow Ncorr to use more than one CPU core to speed up computation process.

5. DIC Analysis

The important option is seed placement. Number of seeds depends on the available computational cores set up in previous step. Seeds provide the initial guesses of the RG-DIC analysis and divide the ROI into partitions to parallel computation of each partition. Seeds have to be set in a way to divide the ROI into the partitions of more or less same size. After setting the seeds is possible to run the RG-DIC analysis. Optimal setting of seeds is shown in Figure 2.16

6. Formatting Displacements

In Formatting Displacements menu preview of calculated displacements are provided and it is possible to set many options to provided results.

At first the relationship between the pixel scale and real scale by choosing the Get Unit Conversion button can be set. It is important to get absolute displacement in the real scale, not only relative in pixels.

Formatting Options is a filter with possibility to cut-off noisy, low or very high displacements. This filter can be applied to all images.

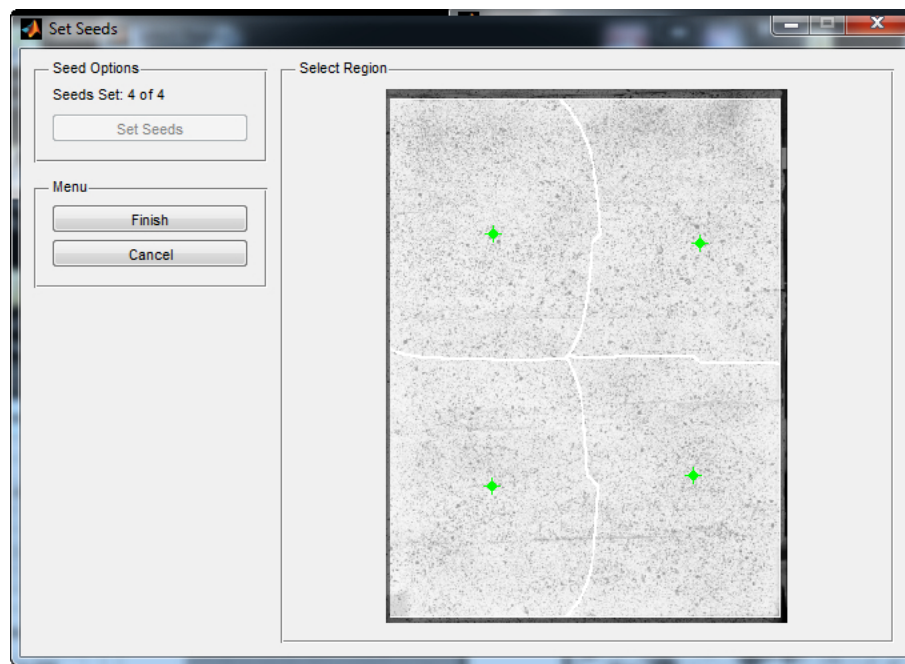


Figure 2.16: Optimal distribution of seeds (green dots) in Ncorr.

Lens Distortion Options is the option to correct the image for errors caused by lens distortion effect. The correction algorithm assumes the distortion center in the center of image.

Example of displacement settings dialogue window is shown in Figure 2.17.

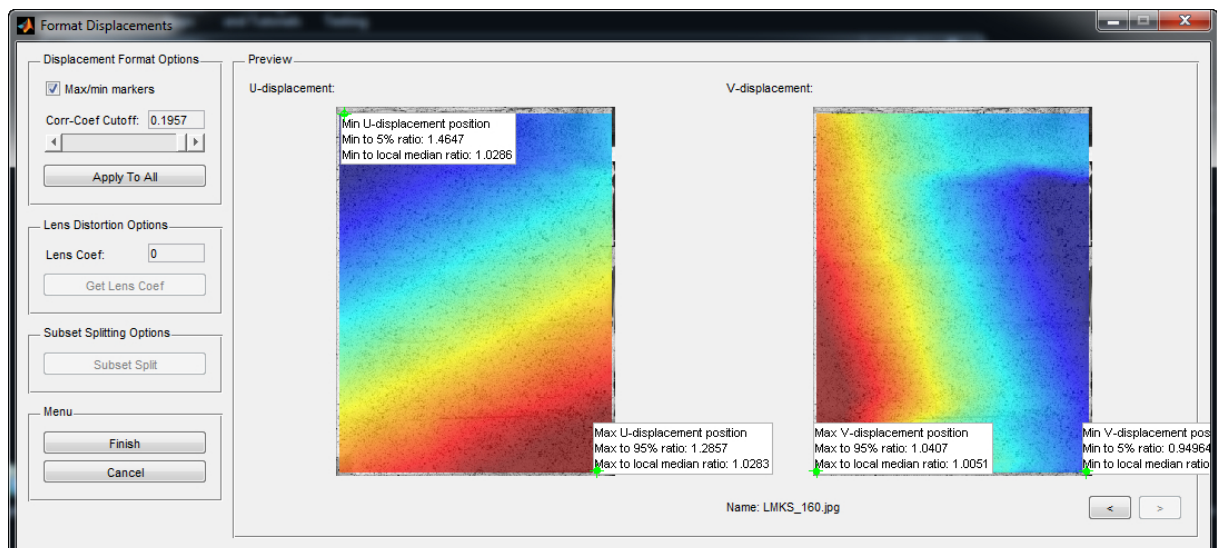


Figure 2.17: Displacement formatting window in Ncorr.

7. Strain Analysis

As mentioned above, strains in Ncorr are calculated from the displacement data based on square plane fit to a local group of data points (circles). Then the averaged displacement gradients are used to calculate the Green-Lagrangian strains.

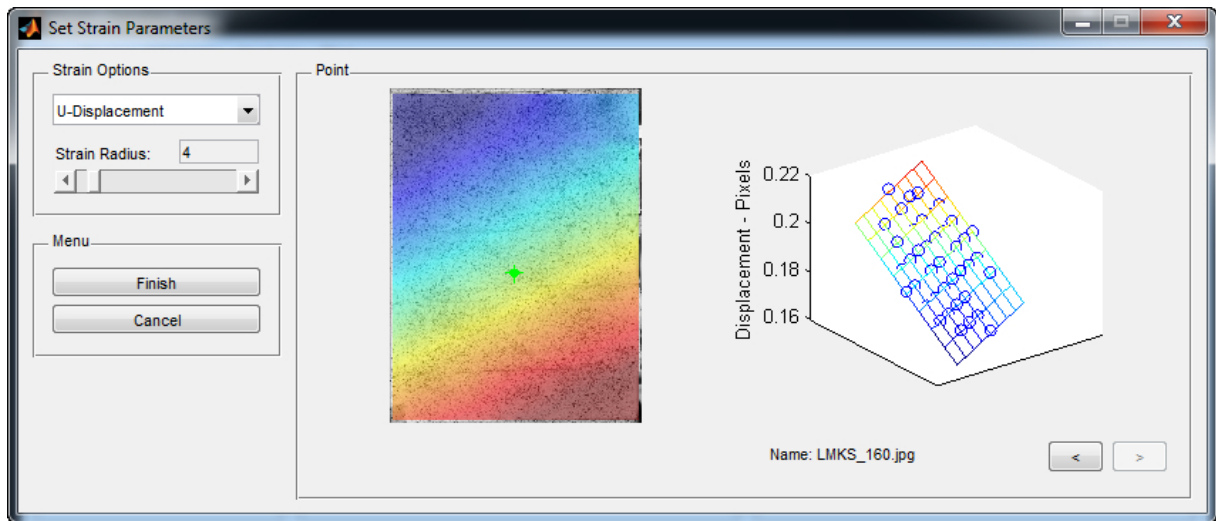


Figure 2.18: Strain Analysis window in Ncorr.

Strain Options – strain radius is an option to set up the radius of the circle which selects the group of points to fit the plane to. This selection is similar to subset radius setup, the smaller radius leads to obtain non-noisy strain data. Example of calculated strains is demonstrated in Figure 2.18.

8. Plotting

At this step, displacements together with strains have been calculated. Plotting menu provides possibility to use the calculated deformations / strains color map with various transparency together with the analyzed image. Also provides the option of showing the scale, axes and scalebar on the images. Eventually, the figure can be exported, but the software lacks some useful abilities such as saving the set options for further export or mass exporting of all images in the series. To that purpose the Ncorr_post tool has been developed [69].

Plotting menu dialogue is shown in Figure 2.19.

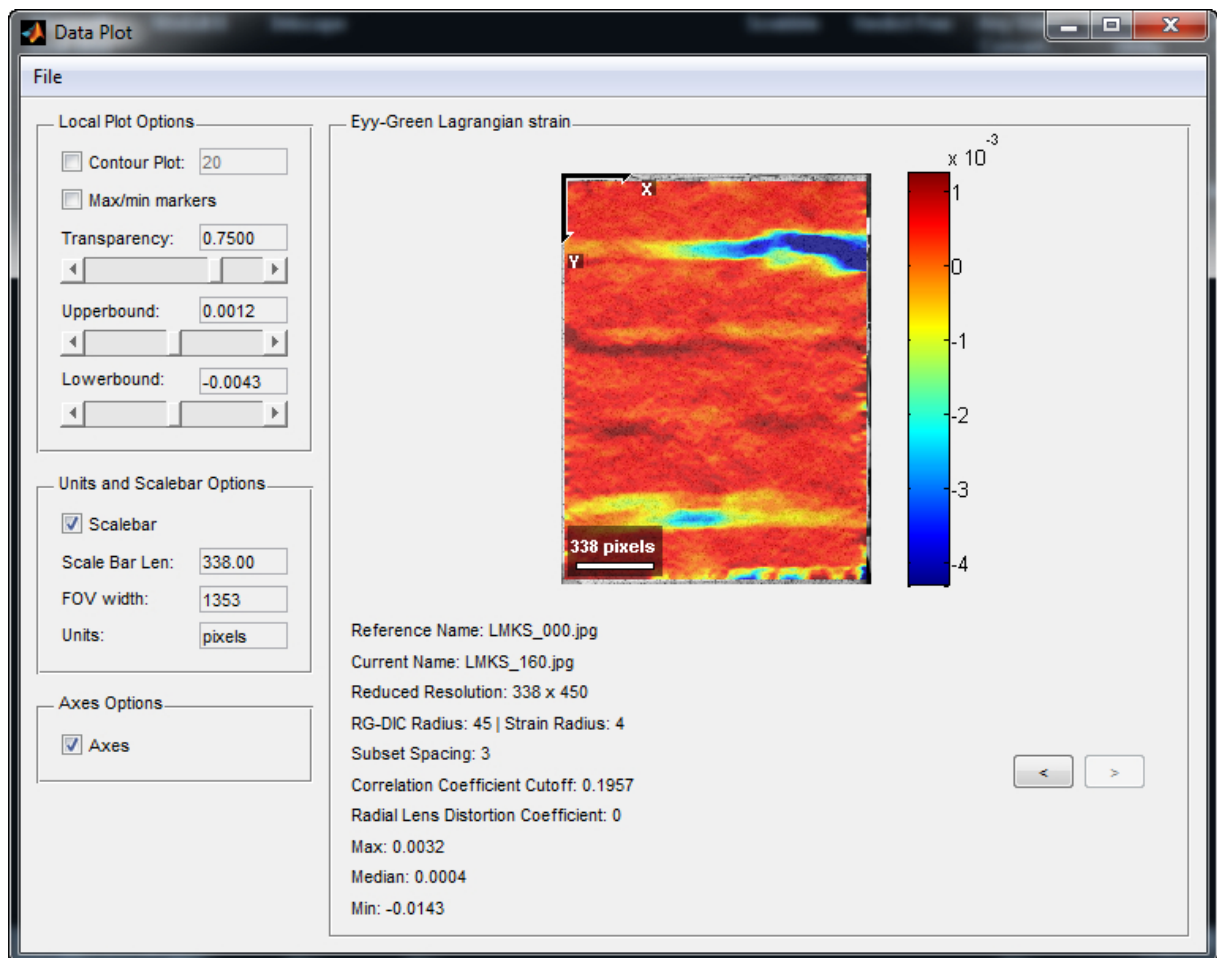


Figure 2.19: Ncorr plotting options.

2.3.5.1 Ncorr_post

Ncorr_post is opensource DIC post-processing tool developed by Václav Nežerka at the Department of Mechanics, Faculty of Civil Engineering, CTU in Prague. Ncorr_post operates in MATLAB environment as well as Ncorr and is capable of loading the *handles_ncorr* data structure which contains the strain and displacement data.

Ncorr_post provides the same abilities as the post-processing menu in Ncorr, namely scaling the displacements and adjusting the graphical output plots, but adds new features such as placing virtual extensometers and plotting the figure of displacement or putting the arrows of magnitude and orientation of principal strains instead of color map to the image. Main advantage of this tool is possibility to save the current project with all settings to be loaded in future or the indispensable ability to apply setting to all images in a series with mass exporting of all images or direct video export. The main application window appears in Figure 2.20. Figure 2.21 demonstrates the plot of displacement obtained by calculations in Ncorr_post and Figure 2.22 provides an example of arrow mode to represent principal strains.

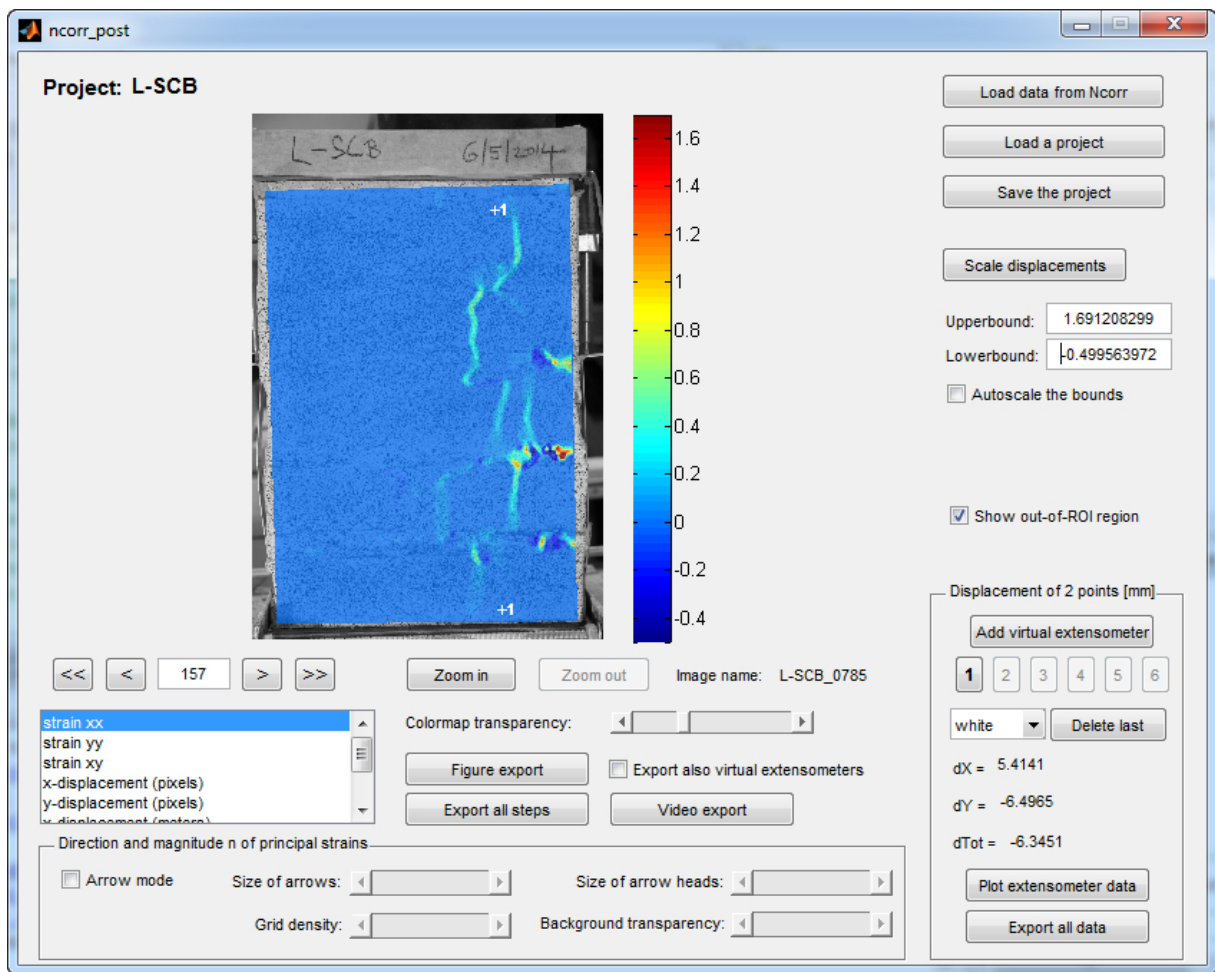


Figure 2.20: Main window of Ncorr_post application.

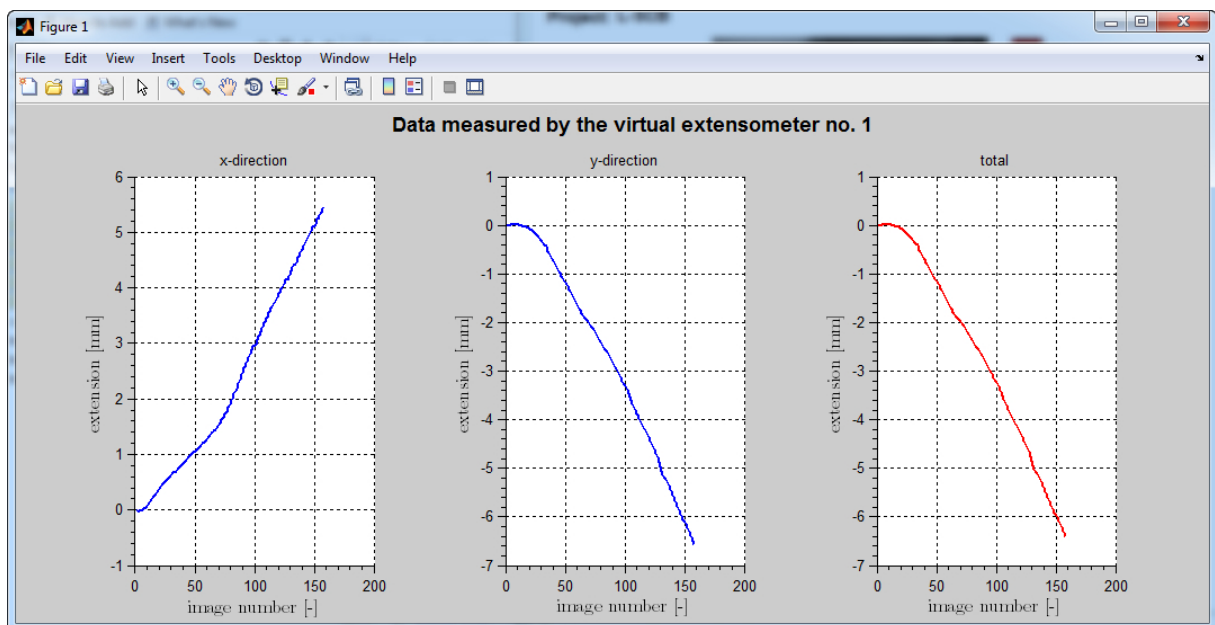


Figure 2.21: Example of virtual extensometers data plotting provided by Ncorr_post.



Figure 2.22: Direction and magnitude of principal strains; L-SCB pier in 410 seconds of the test.

2.3.6 Results of DIC

The capabilities of DIC are presented in this section and the development of maximum principal strains was chosen for the illustration. The presented sequence of images illustrates the development of principal tensile strains and clearly demonstrates the strain localization to the compliant joints, followed by the development of cracks passing through bricks.

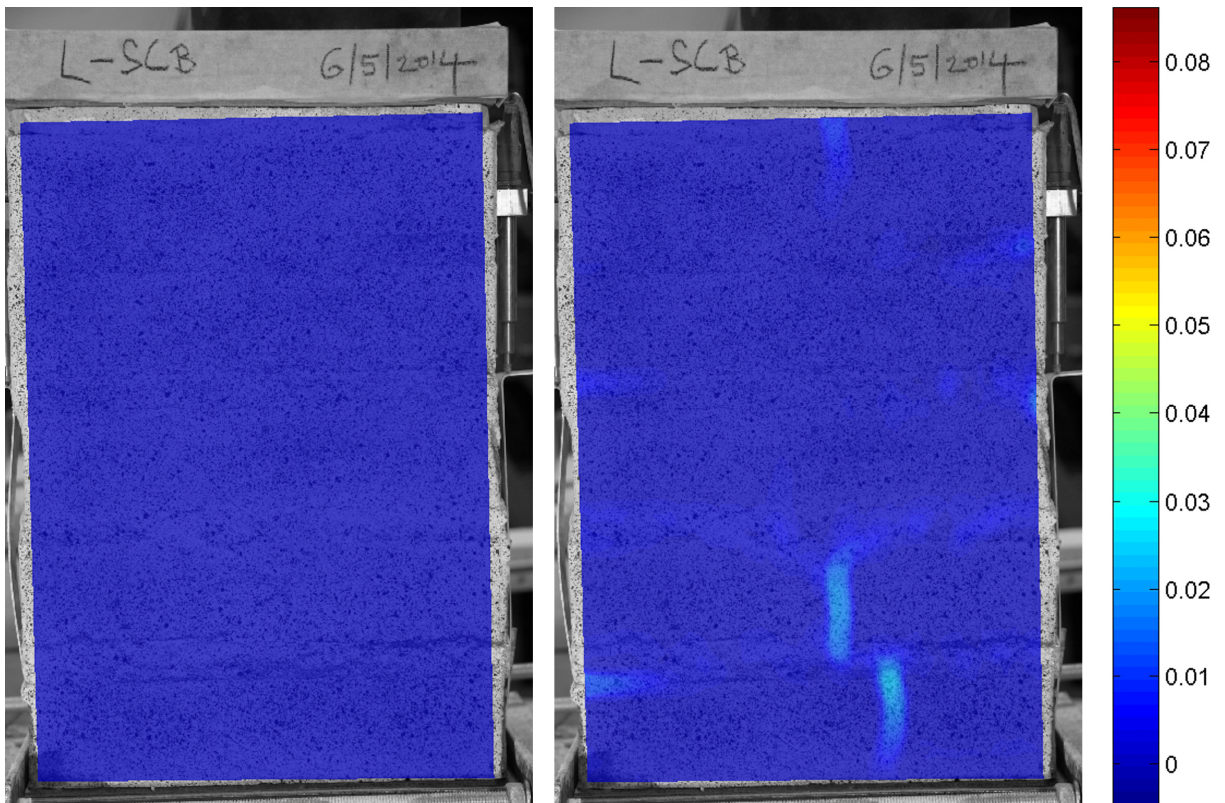


Figure 2.23: Time step: 0s (left) 200s (right).

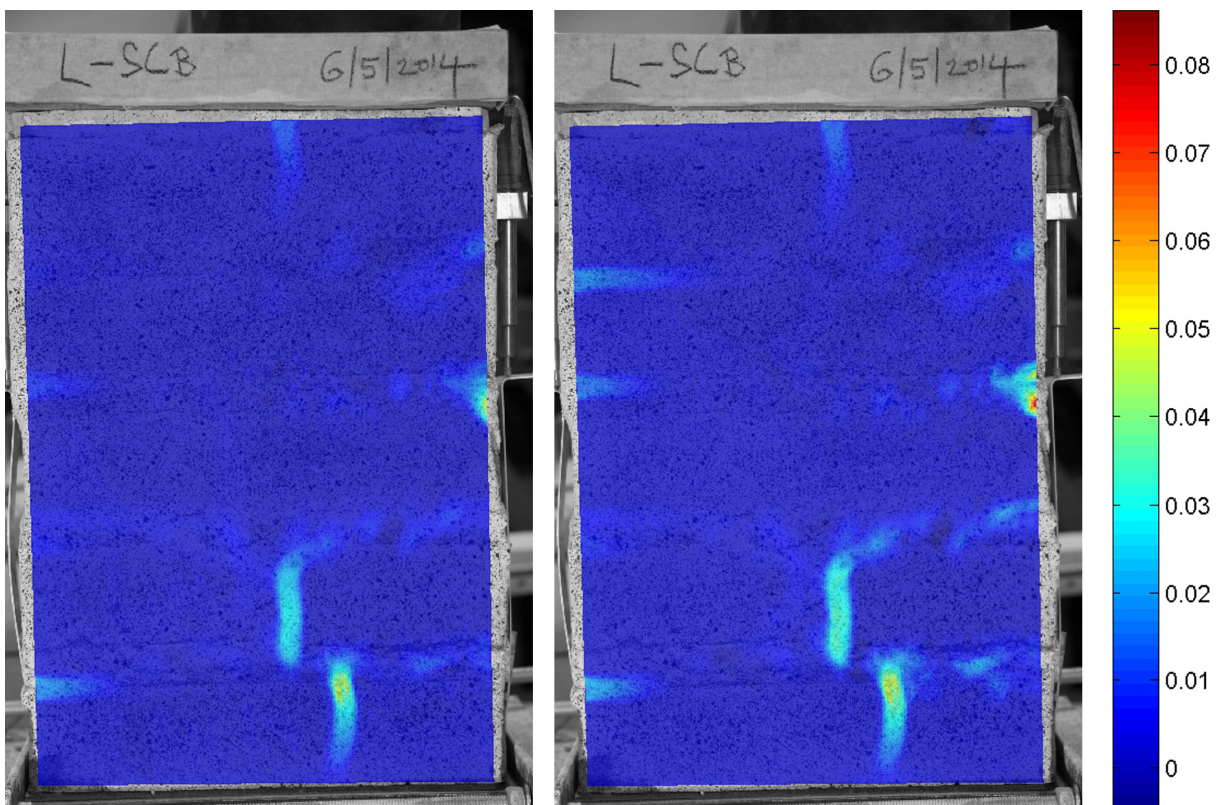


Figure 2.24: Time step: 300s (left) 400s (right).

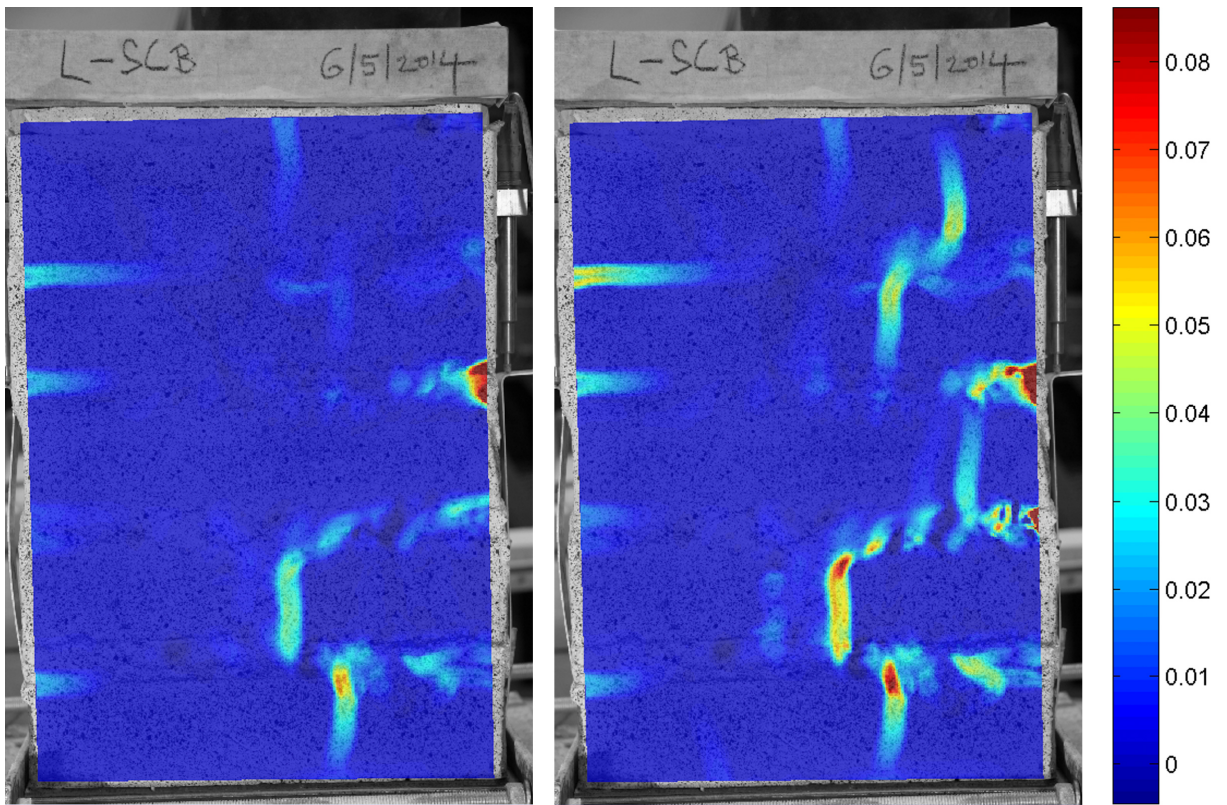


Figure 2.25: Time step: 500s (left) 600s (right).

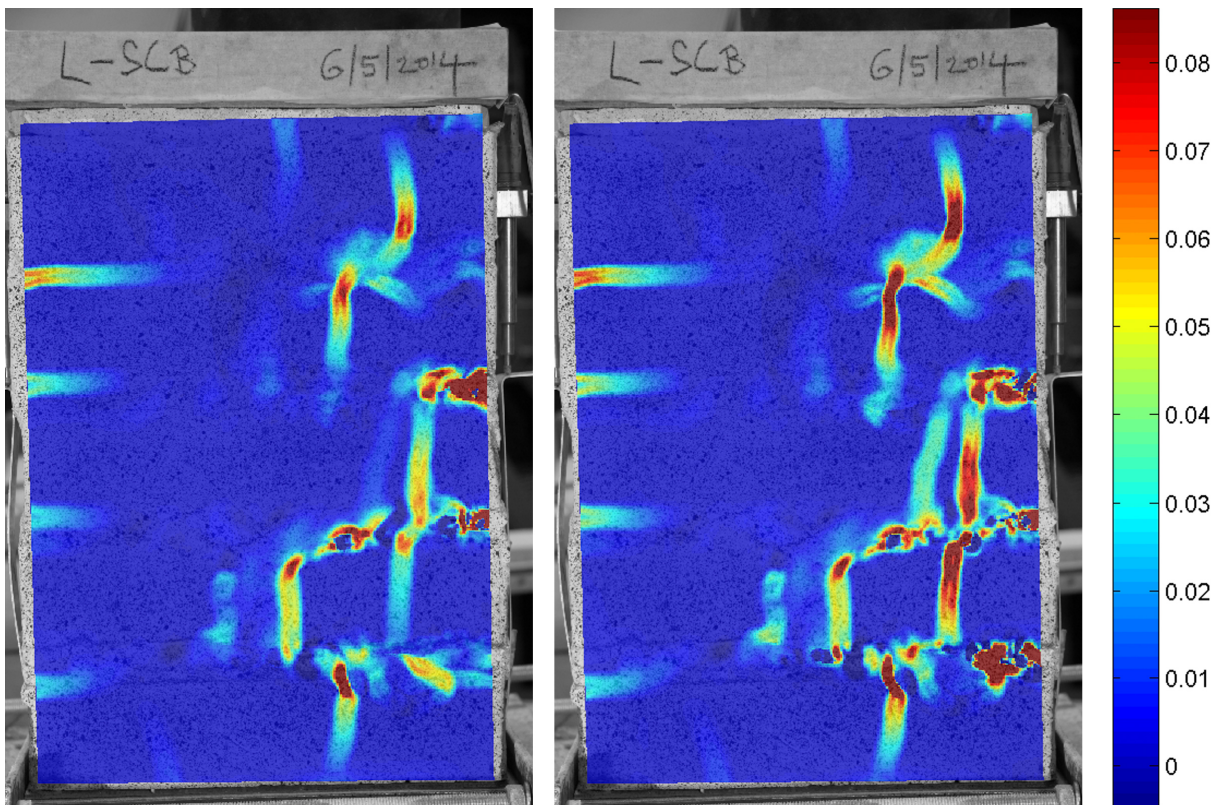


Figure 2.26: Time step: 650s (left) 700s (right).

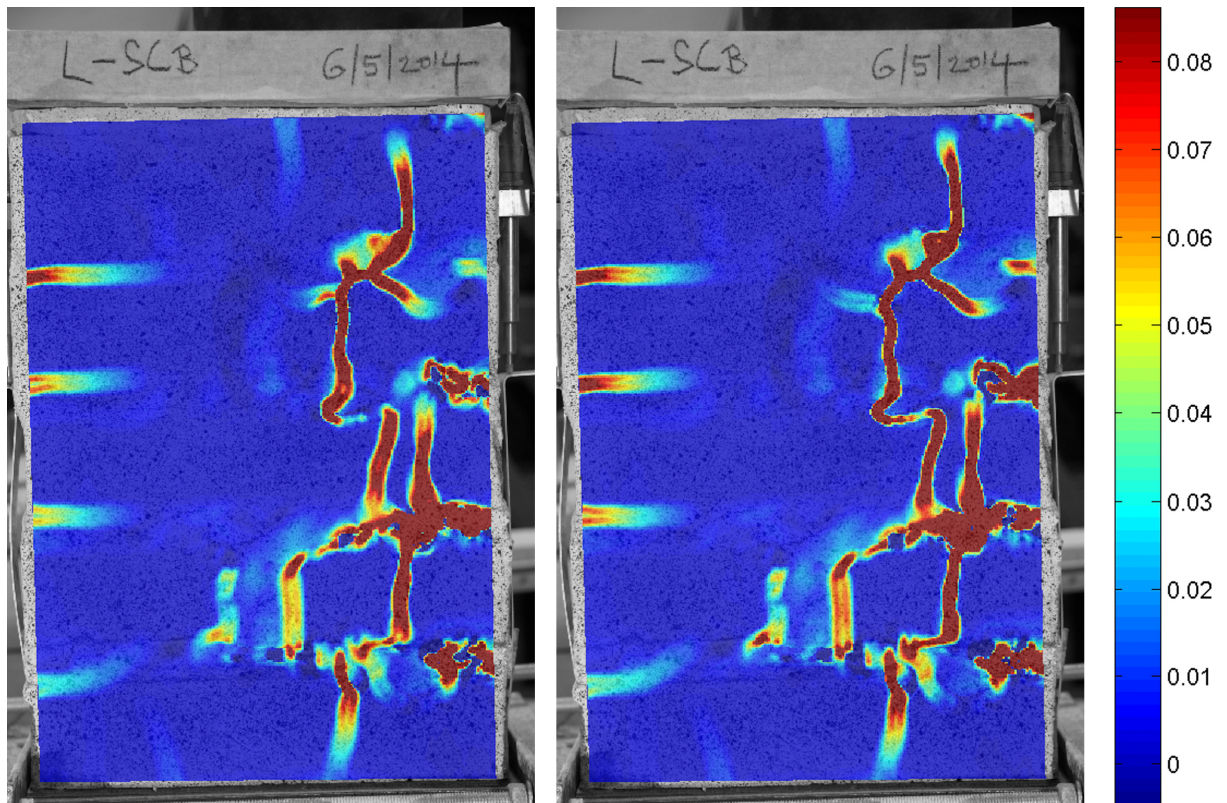


Figure 2.27: Time step: 750s (left) 790s (right).

Chapter 3

Numerical Simulations

The traditional design of masonry structures was based on empirical formulas and experience of masons, while nowadays it is sometimes replaced by a numerical approach, usually the Finite Element Method (FEM) [70]. We employed numerical simulations to find the optimum properties of bed joint mortars used in masonry piers exposed to a combination of compression and bending moment, which are often present in masonry load-bearing elements. This chapter is focused on the description of well-known equations of the theory of elasticity, brief explanation of FEM history, and FEM principles. In the second part of the chapter, our approach to numerical modeling is described.

3.1 Summary of the Theory of Elasticity

The fundamental assumptions of linear elasticity are:

- the body deforms reversibly, after unloading the solid returns to its original state (shape),
- the strain in the specimen depends only on the applied stress, it does not depend on the previous history of loading, neither the rate of loading,
- stress is a linear function of strain,
- heating the homogenous and isotropic material will result in the volumetric change of body without change in shape.

In the engineering terminology the limit state of elasticity of the body (in according to validity of Hooke's law) is such a state above which irreversible deformations occur. The summary of the fundamental elasticity equations is summarized in the diagram provided next.

3.1.1 Kinematic Equations

3.1.1.1 Displacements

A displacement field is an assignment of displacement vectors for all points in a region or body that is displaced from one state to another. A displacement vector specifies the position of a

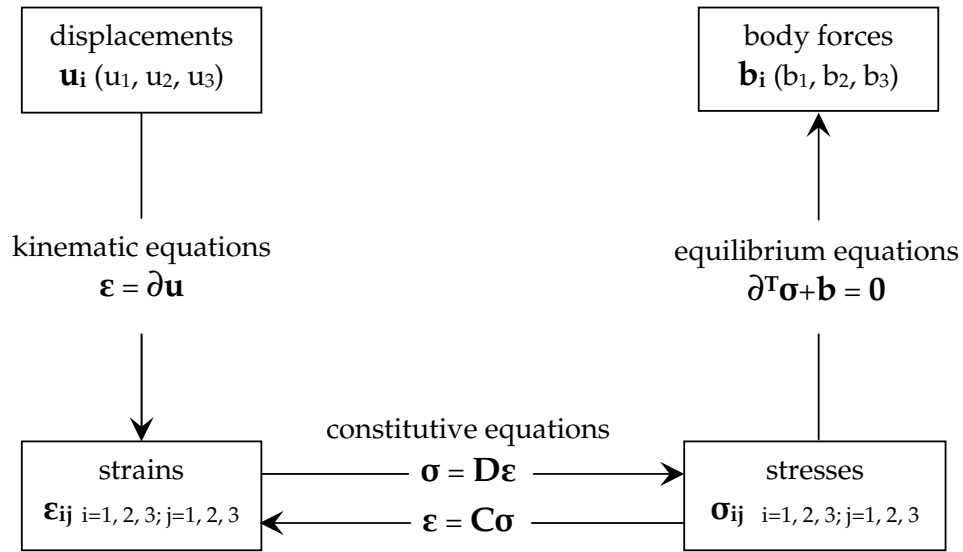


Figure 3.1: Governing equations of elasticity, reproduced from [3].

point or a particle in reference to an origin or to a previous position. The displacements at each point is described by three components (u_x, u_y, u_z), all of them dependent on the position in the Cartesian coordinate system (x_1, x_2, x_3). In a matrix notation, the displacement field can be arranged in a vector and written as

$$\mathbf{u}(x) = \begin{Bmatrix} u_x(x_1, x_2, x_3) \\ u_y(x_1, x_2, x_3) \\ u_z(x_1, x_2, x_3) \end{Bmatrix}. \quad (3.1)$$

3.1.1.2 Strains

Strains describe the deformation of a rigid body. Strains can be also classified as normal strain - acting perpendicular to the face of element or shear strain - acting along the face of element. For an isotropic material normal stresses will cause normal strains. Figure 3.2 presents the meaning of individual deformations on a two-dimensional infinitesimal rectangular material element with dimensions $dx \times dy$, which after deformation takes the form of a rhombus. This transformation relies on the theory of infinitesimal strain or also so-called engineering strain.

Based on the Pythagoras's theorem it is possible to calculate $\text{lenght}(ab)$ as follows

$$\begin{aligned} \text{lenght}(ab) &= \sqrt{\left(dx + \frac{\partial u_x}{\partial x} \partial x\right)^2 + \left(\frac{\partial u_y}{\partial x} \partial x\right)^2} \\ &= dx \sqrt{1 + 2 \frac{\partial u_x}{\partial x} + \left(\frac{\partial u_x}{\partial x}\right)^2 + \left(\frac{\partial u_y}{\partial x}\right)^2}. \end{aligned} \quad (3.2)$$

Because of very small displacement gradients the squares of the derivatives are negligible,

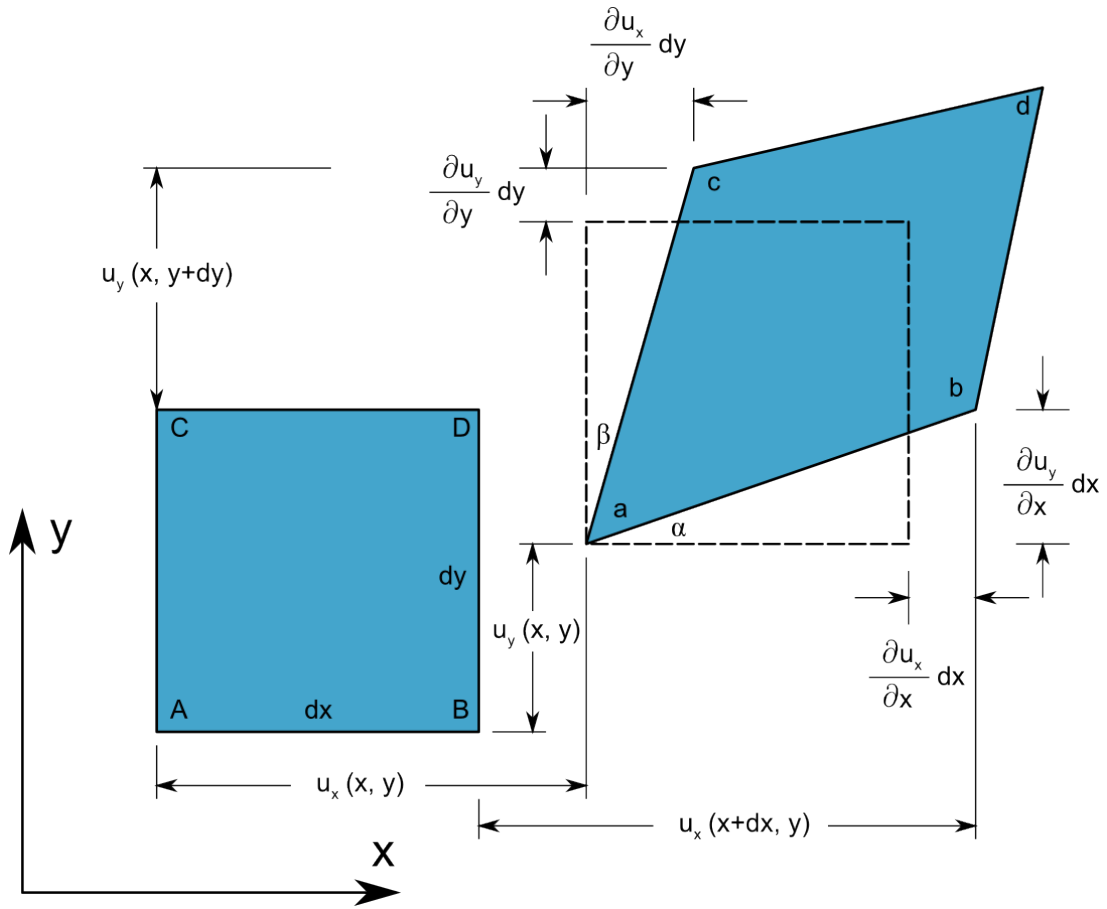


Figure 3.2: Two-dimensional geometric deformation of an infinitesimal material element, reproduced from [4].

$\sqrt{2\frac{\partial u_x}{\partial x}} \approx \frac{\partial u_x}{\partial x}$ and thus is possible to simplify Equation (3.2) into

$$\text{lenght}(ab) \approx dx + \frac{\partial u_x}{\partial x} dx, \quad (3.3)$$

than is the normal strain in the x -direction defined as

$$\varepsilon_{xx} = \frac{\text{lenght}(ab) - \text{lenght}(AB)}{\text{lenght}(AB)} = \frac{dx + \frac{\partial u_x}{\partial x} dx - dx}{dx} = \frac{\partial u_x}{\partial x}. \quad (3.4)$$

Similarly the normal strains in y -direction and z -direction can be expressed in the following form

$$\varepsilon_{yy} = \frac{\partial u_y}{\partial y}, \quad \varepsilon_{zz} = \frac{\partial u_z}{\partial z}. \quad (3.5)$$

The engineering shear strain γ_{xy} represents the changes of angles between lines \overline{AC} and \overline{AB} as the material distorts in response to shear stress. To define shear strains it is necessary to look

at two directions that form the plane that undergoes shear distortion. Therefore,

$$\gamma_{xy} = \alpha + \beta \quad (3.6)$$

and from the geometry provided by Figure 3.2 we obtain

$$\begin{aligned} \tan \alpha &= \frac{\frac{\partial u_y}{\partial x} dx}{dx + \frac{\partial u_x}{\partial x} dx} = \frac{\frac{\partial u_y}{\partial x}}{1 + \frac{\partial u_x}{\partial x}}, \\ \tan \beta &= \frac{\frac{\partial u_x}{\partial y} dy}{dy + \frac{\partial u_y}{\partial y} dy} = \frac{\frac{\partial u_x}{\partial y}}{1 + \frac{\partial u_y}{\partial y}}. \end{aligned} \quad (3.7)$$

We assume that strains are infinitesimal. Consequently

$$\frac{\partial u_x}{\partial x} \ll 1, \quad \frac{\partial u_y}{\partial y} \ll 1. \quad (3.8)$$

For small angle changes it is possible to consider

$$\tan \alpha \approx \alpha \approx \frac{\partial u_x}{\partial x}, \quad \tan \beta \approx \beta \approx \frac{\partial u_y}{\partial y}. \quad (3.9)$$

Introducing simplifications (3.8) and (3.9) into Equation (3.7) yields

$$\gamma_{xy} = \alpha + \beta = \frac{\partial u_x}{\partial x} + \frac{\partial u_y}{\partial y} \quad (3.10)$$

and for other two distortions the same reasoning can be used so that

$$\gamma_{yz} = \gamma_{zy} = \frac{\partial u_y}{\partial z} + \frac{\partial u_z}{\partial y}, \quad \gamma_{zx} = \gamma_{xz} = \frac{\partial u_z}{\partial x} + \frac{\partial u_x}{\partial z}. \quad (3.11)$$

The strain is a second order tensor¹ and components of the infinitesimal strains can then be arranged in the matrix form as follows

$$\boldsymbol{\epsilon} = \begin{bmatrix} \frac{\partial u_x}{\partial x} & \frac{1}{2} \left(\frac{\partial u_x}{\partial y} + \frac{\partial u_y}{\partial x} \right) & \frac{1}{2} \left(\frac{\partial u_x}{\partial z} + \frac{\partial u_z}{\partial x} \right) \\ \frac{1}{2} \left(\frac{\partial u_x}{\partial y} + \frac{\partial u_y}{\partial x} \right) & \frac{\partial u_y}{\partial y} & \frac{1}{2} \left(\frac{\partial u_y}{\partial z} + \frac{\partial u_z}{\partial y} \right) \\ \frac{1}{2} \left(\frac{\partial u_x}{\partial z} + \frac{\partial u_z}{\partial x} \right) & \frac{1}{2} \left(\frac{\partial u_y}{\partial z} + \frac{\partial u_z}{\partial y} \right) & \frac{\partial u_z}{\partial z} \end{bmatrix}. \quad (3.12)$$

In the tensorial notation shear strains (distortions) are expressed as halves of the engineering strains. Individual components of stress and strain tensors can be for convenience arranged in a

¹Tensors are used to represent correspondences between sets of geometric vectors. Because they express a relationship between vectors, tensors themselves must be independent of a particular choice of coordinate system.

pseudovector form and the ordering of elements is basically arbitrary, but conventional is order (1,1), (2,2), (3,3), (2,3), (1,3), (1,2) [71] and this arrangement is the so-called Voigt notation. The strain pseudovector can be also written in terms of the displacement vector and proper operator as

$$\varepsilon = \partial \mathbf{u},$$

$$\begin{Bmatrix} \varepsilon_{xx} \\ \varepsilon_{yy} \\ \varepsilon_{zz} \\ \gamma_{yz} \\ \gamma_{xz} \\ \gamma_{xy} \end{Bmatrix} = \begin{bmatrix} \frac{\partial}{\partial x} & 0 & 0 \\ 0 & \frac{\partial}{\partial y} & 0 \\ 0 & 0 & \frac{\partial}{\partial z} \\ 0 & \frac{\partial}{\partial z} & \frac{\partial}{\partial y} \\ \frac{\partial}{\partial z} & 0 & \frac{\partial}{\partial x} \\ \frac{\partial}{\partial y} & \frac{\partial}{\partial x} & 0 \end{bmatrix} \begin{Bmatrix} u_x \\ u_y \\ u_z \end{Bmatrix}. \quad (3.13)$$

3.1.2 Static Equations

The main goal of stress analysis is determining the variation of stress. The components are functions of position within the interior of a body. Combined stresses cannot be described by a single vector. Even if the material is stressed in the same way throughout the volume of the body, the stress across any imaginary surface will depend on the orientation of that surface. The force equilibrium of an infinitesimal cube yields the following equations

$$\begin{aligned} \frac{\partial \sigma_{xx}}{\partial x} + \frac{\partial \tau_{yx}}{\partial y} + \frac{\partial \tau_{zx}}{\partial z} + b_x &= 0, \\ \frac{\partial \tau_{xy}}{\partial x} + \frac{\partial \sigma_{yy}}{\partial y} + \frac{\partial \tau_{zy}}{\partial z} + b_y &= 0, \\ \frac{\partial \tau_{xz}}{\partial x} + \frac{\partial \tau_{yz}}{\partial y} + \frac{\partial \sigma_{zz}}{\partial z} + b_z &= 0, \end{aligned} \quad (3.14)$$

where b_i are body forces. The equilibrium can be expressed in the matrix form as

$$\begin{bmatrix} \frac{\partial}{\partial x} & 0 & 0 & 0 & \frac{\partial}{\partial z} & \frac{\partial}{\partial y} \\ 0 & \frac{\partial}{\partial y} & 0 & \frac{\partial}{\partial z} & 0 & \frac{\partial}{\partial x} \\ 0 & 0 & \frac{\partial}{\partial z} & \frac{\partial}{\partial y} & \frac{\partial}{\partial x} & 0 \end{bmatrix} \begin{Bmatrix} \sigma_{xx} \\ \sigma_{yy} \\ \sigma_{zz} \\ \tau_{yz} \\ \tau_{xz} \\ \tau_{xy} \end{Bmatrix} + \begin{Bmatrix} b_x \\ b_y \\ b_z \end{Bmatrix} = \begin{Bmatrix} 0 \\ 0 \\ 0 \end{Bmatrix}. \quad (3.15)$$

Stress tensor, completely describes the stress state of a continuum body. The stress tensor can be represented in any chosen Cartesian coordinate system by the 3×3 matrix of real numbers in

the following form:

$$\boldsymbol{\sigma} = \begin{bmatrix} \sigma_{xx} & \tau_{xy} & \tau_{xz} \\ \tau_{yx} & \sigma_{yy} & \tau_{yz} \\ \tau_{zx} & \tau_{zy} & \sigma_{zz} \end{bmatrix}. \quad (3.16)$$

By Newton's laws of motion, any external forces being applied to such a system must be balanced by internal reaction forces [72]. Equilibrium of the stress and surface traction expressed by Cauchy's formula requests the equilibrium of the external traction forces with internal stress. The traction vector \mathbf{t} is associated with any plane characterized by its normal n . This is called stress on the surface of the body and it is defined by following equation

$$\mathbf{t} = \lim_{\Delta A \rightarrow 0} \frac{\Delta \mathbf{F}}{\Delta A}, \quad (3.17)$$

where $\Delta \mathbf{F}$ is external force and ΔA is the magnitude of the area on which external force acts. Traction is a force vector and in 3-D is completely defined by three components associated with the coordinate planes:

$$\mathbf{t}^{(x)} = \begin{Bmatrix} \sigma_{xx} \\ \tau_{xy} \\ \tau_{xz} \end{Bmatrix} \quad (3.18)$$

and for an arbitrary normal plane n it holds that

$$\mathbf{t}^{(n)} = \mathbf{t}^{(x)} n_x + \mathbf{t}^{(y)} n_y + \mathbf{t}^{(z)} n_z, \quad (3.19)$$

which can be written in a compact form as

$$\mathbf{t} = \boldsymbol{\sigma} \mathbf{n}, \quad (3.20)$$

or in a matrix form as follows

$$\begin{Bmatrix} t^{(x)} \\ t^{(y)} \\ t^{(z)} \end{Bmatrix} = \begin{bmatrix} \sigma_{xx} & \tau_{xy} & \tau_{xz} \\ \tau_{yx} & \sigma_{yy} & \tau_{yz} \\ \tau_{zx} & \tau_{zy} & \sigma_{zz} \end{bmatrix} \begin{Bmatrix} n_x \\ n_y \\ n_z \end{Bmatrix}. \quad (3.21)$$

The principle of conservation of angular momentum implies that the stress tensor is symmetric, that leads to equality of following identities: $\tau_{xy} = \tau_{yx}$, $\tau_{xz} = \tau_{zx}$ and $\tau_{yz} = \tau_{zy}$. Therefore, the stress state of the medium at any point and instant can be specified by only six independent parameters, rather than nine. Elements σ_{xx} , σ_{yy} , σ_{zz} are called the orthogonal normal stresses and τ_{xy} , τ_{xz} , τ_{yz} the orthogonal shear stresses.

3.1.2.1 Principal Stresses

Rotating the compounds of stresses around the axis provides different values of stress for different angles. However, the principal stresses, being invariants independent of the coordinate system, provide the true stress-state measure. As mentioned in Equation (3.16), stress tensor $\boldsymbol{\sigma}$ can be rewritten into the following form

$$\boldsymbol{\sigma} = \sigma_{ij} = \begin{bmatrix} \sigma_{xx} & \sigma_{xy} & \sigma_{xz} \\ \sigma_{yx} & \sigma_{yy} & \sigma_{yz} \\ \sigma_{zx} & \sigma_{zy} & \sigma_{zz} \end{bmatrix}, \quad (3.22)$$

where the element of the i^{th} row and j^{th} column represents the stress on the i^{th} face in the j^{th} direction. The principal stress values can be then calculated as the eigenvalues of the 3×3 matrix:

$$\begin{vmatrix} \sigma_{xx} - \lambda & \sigma_{xy} & \sigma_{xz} \\ \sigma_{yx} & \sigma_{yy} - \lambda & \sigma_{yz} \\ \sigma_{zx} & \sigma_{zy} & \sigma_{zz} - \lambda \end{vmatrix} = 0. \quad (3.23)$$

The computed values λ are equal to the principal values of stress tensor and the Equation (3.23) can be expanded to

$$\begin{aligned} & (\sigma_{xx} - \lambda)[(\sigma_{yy} - \lambda)(\sigma_{zz} - \lambda) - \sigma_{yz}^2] - \sigma_{xy}[\sigma_{xy}(\sigma_{zz} - \lambda) - \sigma_{yz}\sigma_{xz}] + \\ & \sigma_{xz}[\sigma_{xy}\sigma_{yz} - (\sigma_{yy} - \lambda)\sigma_{xz}] = 0 \end{aligned} \quad (3.24)$$

and after expansion

$$\begin{aligned} & \lambda^3 - (\sigma_{xx} + \sigma_{yy} + \sigma_{zz})\lambda^2 + (\sigma_{xx}\sigma_{yy} + \sigma_{yy}\sigma_{zz} + \sigma_{zz}\sigma_{xx} - \sigma_{xy}^2 - \sigma_{xz}^2 - \sigma_{yz}^2)\lambda - \\ & (\sigma_{xx}\sigma_{yy}\sigma_{zz} - \sigma_{xx}\sigma_{yz}^2 - \sigma_{yy}\sigma_{xz}^2 - \sigma_{zz}\sigma_{xy}^2 + 2\sigma_{xy}\sigma_{xz}\sigma_{yz}) = 0. \end{aligned} \quad (3.25)$$

Equation (3.25) can be rewritten into the following form

$$\lambda^3 - I_1\lambda^2 + I_2\lambda - I_3 = 0, \quad (3.26)$$

where invariants I_1, I_2, I_3 are defined as:

$$\begin{aligned} I_1 &= \sigma_{xx} + \sigma_{yy} + \sigma_{zz}, \\ I_2 &= \sigma_{xx}\sigma_{yy} + \sigma_{yy}\sigma_{zz} + \sigma_{zz}\sigma_{xx} - \sigma_{xy}^2 - \sigma_{xz}^2 - \sigma_{yz}^2, \\ I_3 &= \sigma_{xx}\sigma_{yy}\sigma_{zz} - \sigma_{xx}\sigma_{yz}^2 - \sigma_{yy}\sigma_{xz}^2 - \sigma_{zz}\sigma_{xy}^2 + 2\sigma_{xy}\sigma_{xz}\sigma_{yz}, \end{aligned} \quad (3.27)$$

which can be alternatively written as:

$$\begin{aligned} I_1 &= \text{tr}(\boldsymbol{\sigma}), \\ I_2 &= \begin{vmatrix} \sigma_{xx} & \sigma_{xy} \\ \sigma_{xy} & \sigma_{yy} \end{vmatrix} + \begin{vmatrix} \sigma_{xx} & \sigma_{xz} \\ \sigma_{xz} & \sigma_{zz} \end{vmatrix} + \begin{vmatrix} \sigma_{yy} & \sigma_{yz} \\ \sigma_{yz} & \sigma_{zz} \end{vmatrix}, \\ I_3 &= \det(\boldsymbol{\sigma}). \end{aligned} \quad (3.28)$$

For the sake of material modeling it is convenient to introduce two quantities, Q and R

$$Q = \frac{3I_2 - I_1^2}{9}, \quad R = \frac{2I_1^3 - 9I_1I_2 + 27I_3}{54}, \quad (3.29)$$

so that so called Lode angle θ can be expressed as

$$\theta = \cos^{-1} \left(\frac{R}{\sqrt{-Q^3}} \right). \quad (3.30)$$

The values of principal stresses being the eigenvalues of the matrix representing the stress tensor as defined in Equation (3.22) can be found as

$$\begin{aligned} \lambda_1 &= 2\sqrt{-Q} \cos\left(\frac{\theta}{3}\right) + \frac{1}{3}I_1, \\ \lambda_2 &= 2\sqrt{-Q} \cos\left(\frac{\theta + 2\pi}{3}\right) + \frac{1}{3}I_1, \\ \lambda_3 &= 2\sqrt{-Q} \cos\left(\frac{\theta + 4\pi}{3}\right) + \frac{1}{3}I_1. \end{aligned} \quad (3.31)$$

3.1.3 Constitutive Equations

In previous sections the relationships between kinematics (geometry) and statics equilibrium of body were explained, but these equations do not provide any description of the real material. The kinematic equations relate strains to displacements and the static equations relate stresses within a rigid body to the external forces. The six constitutive equations relate the strains to stresses.

Isotropic elastic material exhibits the same properties in all directions and the response of the material in terms of stress to the applied strains can be described by the generalized form of Hooke's law:

$$\boldsymbol{\sigma} = \mathbf{D}\boldsymbol{\varepsilon}, \quad (3.32)$$

where \mathbf{D} is the stiffness matrix of the isotropic material. Based on the previous statements it can be assumed that \mathbf{D} contains 81 independent components. However, since the stress and strain tensors are symmetric, \mathbf{D} has to be also symmetric. These symmetries reduce the number of \mathbf{D} components to 36 and the following equation

$$\begin{Bmatrix} \sigma_{xx} \\ \sigma_{yy} \\ \sigma_{zz} \\ \tau_{yz} \\ \tau_{xz} \\ \tau_{xy} \end{Bmatrix} = \begin{bmatrix} D_{11} & D_{12} & D_{13} & D_{14} & D_{15} & D_{16} \\ D_{21} & D_{22} & D_{23} & D_{24} & D_{25} & D_{26} \\ D_{31} & D_{32} & D_{33} & D_{34} & D_{35} & D_{36} \\ D_{41} & D_{42} & D_{43} & D_{44} & D_{45} & D_{46} \\ D_{51} & D_{52} & D_{53} & D_{54} & D_{55} & D_{56} \\ D_{61} & D_{62} & D_{63} & D_{64} & D_{65} & D_{66} \end{bmatrix} \begin{Bmatrix} \varepsilon_{xx} \\ \varepsilon_{yy} \\ \varepsilon_{zz} \\ \gamma_{yz} \\ \gamma_{xz} \\ \gamma_{xy} \end{Bmatrix} \quad (3.33)$$

demonstrates that the \mathbf{D} matrix is also symmetric, which leads only 21 independent elements.

In the simplest case of the isotropic elastic material having the same stiffness in all directions, the \mathbf{D} matrix can be further reduced, because here are only two independent material constants, e.g. Young's modulus (E) and Poisson's ratio (ν) and from these two elements, so-called shear modulus (G) can be calculated as

$$G = \frac{E}{2(1 + \nu)}. \quad (3.34)$$

A uniaxially loaded body by the stress σ_{xx} will result in elongation inversely proportional to applied stress and Young's modulus $\varepsilon_{xx} = \sigma_{xx}/E$ in the direction of x -axis and in other two orthogonal axis y and z it will exhibit contraction $\varepsilon_{yy} = \varepsilon_{zz} = -\nu\varepsilon_{xx} = -\nu\sigma_{xx}/E$. In a general stress-state the other normal strain components can be obtained analogically

$$\begin{aligned} \varepsilon_{xx} &= \frac{1}{E}(\sigma_{xx} - \nu\sigma_{yy} - \nu\sigma_{zz}), \\ \varepsilon_{yy} &= \frac{1}{E}(-\nu\sigma_{xx} + \sigma_{yy} - \nu\sigma_{zz}), \\ \varepsilon_{zz} &= \frac{1}{E}(-\nu\sigma_{xx} - \nu\sigma_{yy} + \sigma_{zz}). \end{aligned} \quad (3.35)$$

In case of isotropic material the shear deformations are dependent on shear stresses and shear

modulus

$$\begin{aligned}\gamma_{yz} &= \frac{\tau_{yz}}{G} = \frac{2(1+\nu)}{E}\tau_{yz}, \\ \gamma_{xz} &= \frac{\tau_{xz}}{G} = \frac{2(1+\nu)}{E}\tau_{xz}, \\ \gamma_{xy} &= \frac{\tau_{xy}}{G} = \frac{2(1+\nu)}{E}\tau_{xy}.\end{aligned}\tag{3.36}$$

The six constitutive equations for isotropic materials can be written in the matrix form as

$$\begin{Bmatrix} \varepsilon_{xx} \\ \varepsilon_{yy} \\ \varepsilon_{zz} \\ \gamma_{yz} \\ \gamma_{xz} \\ \gamma_{xy} \end{Bmatrix} = \frac{1}{E} \begin{bmatrix} 1 & -\nu & -\nu & 0 & 0 & 0 \\ -\nu & 1 & -\nu & 0 & 0 & 0 \\ -\nu & -\nu & 1 & 0 & 0 & 0 \\ 0 & 0 & 0 & 2(1+\nu) & 0 & 0 \\ 0 & 0 & 0 & 0 & 2(1+\nu) & 0 \\ 0 & 0 & 0 & 0 & 0 & 2(1+\nu) \end{bmatrix} \begin{Bmatrix} \sigma_{xx} \\ \sigma_{yy} \\ \sigma_{zz} \\ \tau_{yz} \\ \tau_{xz} \\ \tau_{xy} \end{Bmatrix},\tag{3.37}$$

or in compact form as

$$\varepsilon = \mathbf{C}\sigma,\tag{3.38}$$

where \mathbf{C} represents the elastic compliance matrix. By inversion of the compliance matrix obtain the elastic isotropic material stiffness matrix

$$\mathbf{D} = \frac{E}{(1+\nu)(1-2\nu)} \begin{bmatrix} 1-\nu & \nu & \nu & 0 & 0 & 0 \\ \nu & 1-\nu & \nu & 0 & 0 & 0 \\ \nu & \nu & 1-\nu & 0 & 0 & 0 \\ 0 & 0 & 0 & 0.5-\nu & 0 & 0 \\ 0 & 0 & 0 & 0 & 0.5-\nu & 0 \\ 0 & 0 & 0 & 0 & 0 & 0.5-\nu \end{bmatrix}.\tag{3.39}$$

3.2 Introduction to FEM

The origin of FEM can be traced back to the first half of 20th century. A paper by R. L. Courant, who used triangular elements with variational principles to solve vibration problems [73, 74], is considered to be the first FEM reference. Since then many researchers have contributed to develop the method as we know it nowadays, namely M. J. Turner, R. W. Clough, E. L. Wilson, K. J. Bathe, J. H. Argyris, T. Belytschko and O. Zienkiewicz. In the late 1960s the interest in FEM grew rapidly and Edward L. Wilson did a first widely accepted computer package for structural analysis. Than research continued mainly at NASA, and their engineers founded a project to develop a program for general-purpose finite element analysis, NASTRAN, firstly mainly for needs of aeronautics.

At nearly the same time, a finite element program at Westinghouse Electronics Corp. was developed and primarily used for the analysis of nuclear reactors. This software was released to market in 1969 and sold under the commercial name ANSYS. Many non-commercial and open-source software packages were also developed, for example OOFEM [75] by professor Bořek Patzák at the Department of Mechanics, Faculty of Civil Engineering, CTU in Prague.

FEM computations are indispensable in today's world and needed almost in all scientific areas like structural mechanics, stress and thermal analysis, seismic analysis, analysis of dynamics problems, fluid and flow analysis, electromagnetic field study but also for instance metrology models for weather prediction or analysis of surgical procedures and many others fields of interest.

3.2.1 Principle of FEM

FE method was originally developed as matrix method of structural analysis. FEM subdivides the whole domain into finite number of simple parts, called elements, and these elements are connected at points called nodes. This method was first used for discrete structures only - trusses and frames and later it was extended for 2D/3D continuum.

FEM is considered to be an extension of Rayleigh-Ritz method, eliminating the difficulty of dealing with a large polynomial representing a suitable displacement field valid over the entire structure [76]. Cornerstone of this method consists of choosing a displacement field over the entire component, usually in the form of a polynomial function, and evaluating unknown coefficients of the polynomial for minimum potential energy by Lagrangian principle: Of all kinematically admissible states of the elastic body takes one that gives the potential energy minimum of the system: $\Pi = \min$. Total potential energy of deformation Π consists of a sum of potential energies of internal forces E_i and potential energy of external forces E_e .

$$E_i = \int_{\Omega} \frac{1}{2} \boldsymbol{\varepsilon}^T \boldsymbol{\sigma} d\Omega, \quad (3.40)$$

$$E_e = - \int_{\Omega} \mathbf{d}^T \bar{\mathbf{X}} d\Omega - \int_{\Gamma_t} \mathbf{d}^T \bar{\mathbf{p}} d\Gamma, \quad (3.41)$$

where Ω is a volume of the body, $\boldsymbol{\varepsilon}$ is array of strains, $\boldsymbol{\sigma}$ is array of stresses, \mathbf{d} is a vector of displacements, $\bar{\mathbf{X}}$ is a vector of body forces and $\bar{\mathbf{p}}$ is the vector of distributed forces acting on the boundary Γ_t of the body. Total potential energy of deformation is the

$$\Pi = E_i + E_e. \quad (3.42)$$

The minimum of the potential energy is expressed by means of functional $\delta\Pi$, which must be equal to zero as declared by the following equation

$$\delta\Pi = \int_{\Omega} \delta\boldsymbol{\varepsilon}^T \underbrace{\frac{\delta W}{\delta \boldsymbol{\varepsilon}}}_{\boldsymbol{\sigma}} d\Omega - \int_{\Omega} \delta\mathbf{d}^T \bar{\mathbf{X}} d\Omega - \int_{\Gamma_t} \delta\mathbf{d}^T \bar{\mathbf{p}} d\Gamma = \mathbf{0}. \quad (3.43)$$

It is necessary to note that kinematically admissible displacement field must be continuous, must have piecewise continuous derivatives throughout the entire domain and must comply with kinematic boundary conditions on the boundary Γ_t [77]. As the result an approximated solution to the boundary value problem for partial differential equations is obtained.

The theory related to FEM is in detail discussed in the author's bachelor thesis [3], where a particular attention devoted to:

- division elements into groups: Discrete 1D elements and continuum 2D and 3D elements,
- classification of elements: Simplex, Complex and Multiplex,
- elements aspect ratio,
- inter-element compatibility.

3.2.2 Convergence Conditions

While the approximation function is chosen to represent the displacement field over the entire element, several convergence criteria should be ensured:

1. the function should be continuous and differentiable (to obtain e.g. strains) within the element,
2. the displacement polynomial should include constant term, representing e.g. rigid body displacement in solid mechanics,
3. the polynomial should include linear terms, which on differentiation give constant terms,
4. compatibility of the displacement and its derivatives, up to the required order, must be satisfied across inter-element boundaries. Otherwise the displacement solution may result in separated or overlapped inter-element boundaries when the displacement patterns of deformed elements with a common boundary are plotted separately.

3.2.3 Linearity / Nonlinearity

In the previous Section 3.1 a linear relationship between stress or strain and displacement was explained. Linear response to loading represents the most simple constitutive behavior but in a reality almost all materials exhibit nonlinear characteristics even before reaching the elastic limit defined by Hooke's law. Other nonlinearities could be characterized by slight geometrical inhomogeneities and imperfections – this variation is named as geometrical nonlinearity. When the stress-strain diagram exhibits nonlinear relationship, it is possible to consider that in the every load step the structural stiffness changes too.

In nonlinear structural analysis the following consequences have to be recognized:

- the principle of superposition cannot be applied, results of several load case cannot be combined or scaled too,
- loading history cannot be neglected,
- the initial stress-state, e.g. in concrete residual stresses from shrinkage, must be also important.

In the nonlinear FE analysis the applied load is divided into small load increment steps because the relationship between global vector of nodal forces equivalent stresses acting in the

elements \mathbf{f}_{int} and nodal displacements \mathbf{d} is nonlinear. We assume that discretized weak form of the governing equations is

$$\mathbf{f}_{\text{int}} = \mathbf{f}_{\text{ext}} . \quad (3.44)$$

Equation (3.44) can be rewritten in the following form

$$\mathbf{K}\mathbf{d} = \mathbf{f}_{\text{ext}} , \quad (3.45)$$

where \mathbf{K} is the stiffness matrix, \mathbf{d} is an array of nodal displacement values and \mathbf{f}_{ext} is a vector of nodal loads representing surface and volume forces. Where the matrix of internal forces, \mathbf{f}_{int} , is a function of nodal displacements, denoted $\bar{\mathbf{d}}$, and these have to be found in order to fulfil the condition

$$\mathbf{f}_{\text{int}}(\bar{\mathbf{d}}) = \mathbf{f}_{\text{ext}} . \quad (3.46)$$

The task is solved step by step in small increments. Initial solution in step t is known, for example from the previous calculation or it is represented initial (unloaded) balanced state as

$$\mathbf{f}_{\text{int}}(\mathbf{d}) = \bar{\mathbf{f}}_{\text{ext}} \quad (3.47)$$

and after incremental change of load (load controlled simulations) we can rewrite the Equation (3.47) into following form

$$\mathbf{f}_{\text{int}}(\mathbf{d} + \Delta\mathbf{d}) = \bar{\mathbf{f}}_{\text{ext}} + \Delta\mathbf{f}_{\text{ext}} . \quad (3.48)$$

The principal task is to calculate the vector $\Delta\mathbf{d}$ to meet (at least approximately) condition (3.48). The values of $\bar{\mathbf{f}}_{\text{ext}} + \Delta\mathbf{f}_{\text{ext}}$ are known, because the load increment is known. Problem is that the vector of internal forces \mathbf{f}_{int} cannot be found analytically because of nonlinear dependence \mathbf{f}_{int} on \mathbf{d} .

There are several methods developed to solve the non-linear system equations, and the following three are among the most frequently used:

1. incremental solution without iterations (Euler method),
2. iterative solution based on the Newton-Raphson method,
3. other iterative methods, such as BFGS (Broyden-Fletcher-Goldfarb-Shann).

The further text will be focused on the deeper explanation of the Newton-Raphson method since it was used in our simulations. The emphasis will be placed to describe difference between normal Newton-Raphson method and its modified form. Developing of this method is attributed to Isaac Newton (1643-1727) and Joseph Raphson (1648-1715).

Newton-Raphson method (NR) sometimes so-called tangent method is one of the most used numerical methods to solve the systems of nonlinear equations. NR is also referred to as method of tangents, because the solution of the general equation $f(x) = 0$ is sought using differentiation of original function $f(x)$. Using the incremental step-by-step analysis it is possible to rewrite equation (3.48) into following form

$$\mathbf{K}(\mathbf{d})\Delta\mathbf{d} = \bar{\mathbf{f}}_{\text{ext}} - \mathbf{f}_{\text{int}}(\mathbf{d}) , \quad (3.49)$$

where $\mathbf{K}(\mathbf{d})$ is the stiffness matrix dependent on the loading increment of deformation, \mathbf{d} are initial deformations, obtained in the previous step of calculation. The difference between values

$\bar{\mathbf{f}}_{\text{ext}}$ and $\mathbf{f}_{\text{int}}(\mathbf{d})$ represents out-of-balance forces due to the load increment. The stiffness matrix \mathbf{K} is highly dependent on \mathbf{d} , but in one incremental step we assume it as a linear problem. The stiffness matrix is calculated based on the value of \mathbf{d} which is connected with nonlinearity of internal forces and it can be expressed by following equation

$$\mathbf{f}_{\text{int}}(\alpha\mathbf{d}) \neq \alpha\mathbf{f}_{\text{int}}(\mathbf{d}), \quad (3.50)$$

where α is an arbitrary constant. The nonlinearity can be also illustrated on the stiffness matrix relationship before and after the load step

$$\mathbf{K}(\mathbf{d}) \neq \mathbf{K}(\mathbf{d} + \Delta\mathbf{d}). \quad (3.51)$$

The main difference between ordinary Newton-Raphson and Modified Newton-Raphson (MNR) method is the stiffness matrix re-calculation. In normal NR the tangential \mathbf{K} matrix is updated in every iteration, but in the MNR it is updated only in each load-step. Three iterations of one time-step and difference between the methods is illustrated in Figures 3.3 and 3.4.

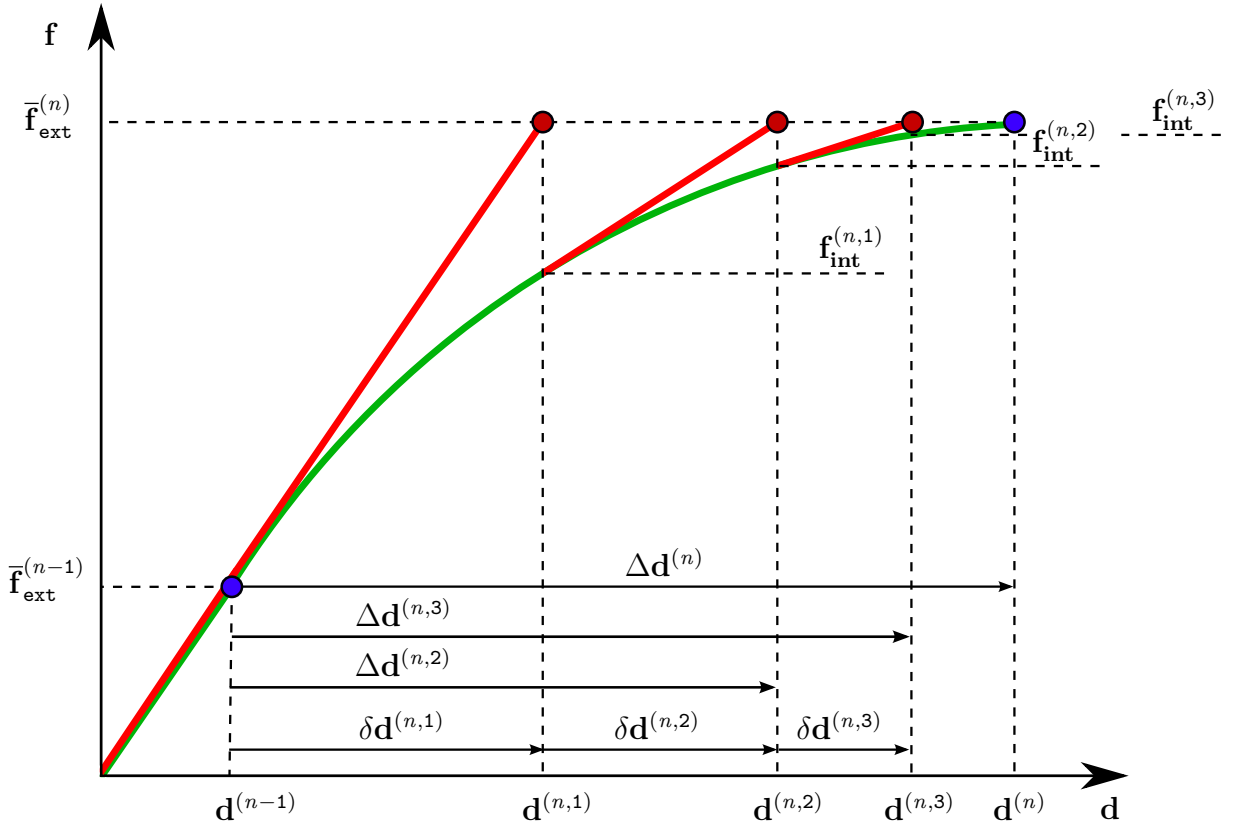


Figure 3.3: Illustration of Newton-Raphson method.

Based on the provided figures the reassigned values are: $\bar{\mathbf{f}}_{\text{ext}}^{(n,1)}$, $\bar{\mathbf{f}}_{\text{ext}}^{(n,2)}$, $\bar{\mathbf{f}}_{\text{ext}}^{(n,3)}$, ... and $\mathbf{d}^{(n,1)}$, $\mathbf{d}^{(n,2)}$, $\mathbf{d}^{(n,3)}$, ... needs to be solved to satisfy the Equation (3.47), which can be rewritten with indexes as $\mathbf{f}_{\text{int}}(\mathbf{d}^{(n)}) = \bar{\mathbf{f}}_{\text{ext}}^{(n)}$, $n = 1, 2, 3, \dots$. Where n denotes the number of solved load-step.

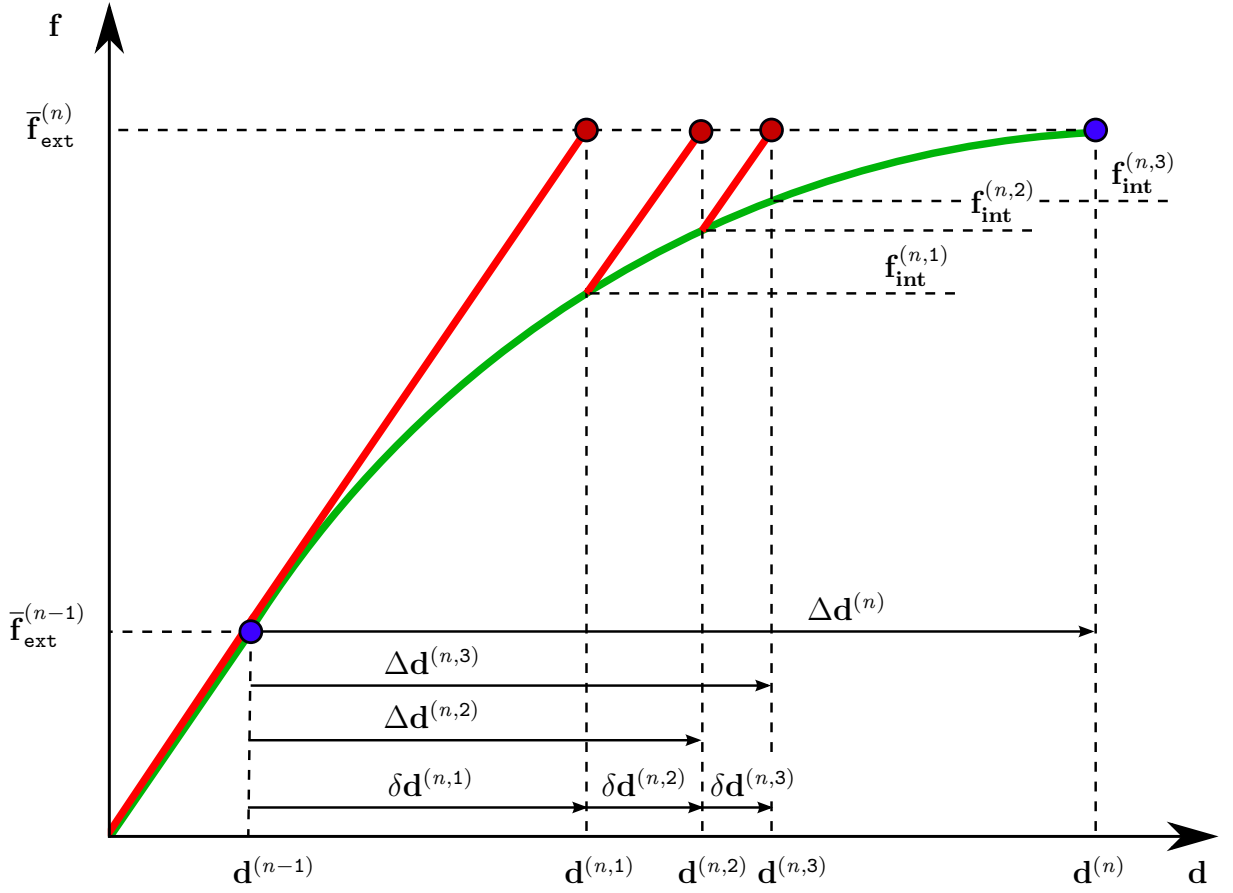


Figure 3.4: Illustration of Modified Newton-Raphson method.

In summary NR iteration algorithm can be written as

$$\left. \begin{aligned} \mathbf{K}^{(n,i-1)} \delta \mathbf{d}^{(n,i)} &= \bar{\mathbf{f}}_{\text{ext}}^{(n)} - \bar{\mathbf{f}}_{\text{int}}^{(n,i-1)} \\ \mathbf{d}^{(n,i)} &= \mathbf{d}^{(n,i-1)} + \delta \mathbf{d}^{(n,i)} \end{aligned} \right\} i = 1, 2, 3, \dots \quad (3.52)$$

and for MNR as

$$\left. \begin{aligned} \mathbf{K}^{(n,0)} \delta \mathbf{d}^{(n,i)} &= \bar{\mathbf{f}}_{\text{ext}}^{(n)} - \bar{\mathbf{f}}_{\text{int}}^{(n,i-1)} \\ \mathbf{d}^{(n,i)} &= \mathbf{d}^{(n,i-1)} + \delta \mathbf{d}^{(n,i)} \end{aligned} \right\} i = 1, 2, 3, \dots, \quad (3.53)$$

where i represents number in sequence of iteration. NR method converges in smaller amount of steps, compared to MNR, but the recalculation of stiffness is required, increasing the computational cost. Therefore, it cannot be concluded which of the two methods is generally faster.

For every iterative solution strategy, it is necessary to select suitable convergence criteria (preset tolerances for reaching equilibrium) for the termination of the iteration process. These criteria, or only a single one criterion, have to be set up in regard to reach effective solution, because too tight convergence tolerances may lead to unjustified increase of computational cost spent to arrive at the results of superfluous accuracy.

The corresponding criterions are:

1. **Displacement error tolerance:** tolerance for the change of displacement increment norm ϵ_D .

$$\frac{\|\Delta \mathbf{d}^{(i)}\|_2}{\|{}^{t+\Delta t} \mathbf{d}\|_2} \leq \epsilon_D \quad (3.54)$$

2. **Out-of-balanced forces tolerance:** tolerance for the change of out-of-balance force norm ϵ_F .

$$\frac{\|{}^{t+\Delta t} \mathbf{f}_{\text{ext}} - {}^{t+\Delta t} \mathbf{f}_{\text{int}}^{(i)}\|_2}{\|{}^{t+\Delta t} \mathbf{f}_{\text{ext}} - {}^t \mathbf{f}_{\text{int}}\|_2} \leq \epsilon_F \quad (3.55)$$

3. **Energy error tolerance:** tolerance of the change of internal energy ϵ_E .

$$\frac{\Delta \mathbf{d}^{(i)T} \cdot \|{}^{t+\Delta t} \mathbf{f}_{\text{ext}} - {}^{t+\Delta t} \mathbf{f}_{\text{int}}^{(i-1)}\|_2}{\Delta \mathbf{d}^{(1)T} \cdot \|{}^{t+\Delta t} \mathbf{f}_{\text{ext}} - {}^t \mathbf{f}_{\text{int}}\|_2} \leq \epsilon_E \quad (3.56)$$

Many iterative solvers uses as default tolerance setting 0.01 for all criterions, but the value of this tolerance depends on the required accuracy of the calculation. In the majority of modern FE computer codes the maximum number of iterations is set up by the user.

3.3 Numerical Modeling

To provide reliable results from numerical simulations, the selected computational model has to be supported by proper material model, which concisely describes the material constitutive behavior. Our approach to verification was carried out through the comparison of failure modes and crack patterns with experimentally obtained data – DIC. According to the studies by Zhou et al. [78] and Wawrzynek and Cincio [79] isotropic damage-plastic models can provide a proper description of masonry response subjected to a mechanical loading. We used material model implemented in OOFEM, developed by Jirásek and Grassl [80]. The mesh generation was accomplished using the open-source platform Salome [81], boundary conditions were applied through MATLAB scripts, calculations were done by OOFEM, post-processing of results and plotting force-displacements diagrams was accomplished in MATLAB and graphical results were rendered in the open-source tool Paraview [82].

The following section will provide detailed information about the material model, process of obtaining the basic material parameters and steps of numerical modeling.

3.3.1 Material Model

The proposed material model was primarily developed for the description of concrete failure behavior subjected to general triaxial stress, but our results indicate that it can be successfully used for the prediction of constitutive behavior for lime-based mortars and clay bricks. The stress-strain law provided by model can be written in following form

$$\boldsymbol{\sigma} = (1 - \omega) \mathbf{D}_e : (\boldsymbol{\varepsilon} - \boldsymbol{\varepsilon}_p), \quad (3.57)$$

where σ is the stress tensor, ω is a scalar damage parameter describing the amount of isotropic damage [83], D_e is the elastic stiffness tensor, ε is the total strain and ε_p is the plastic strain. The plastic part of the model is dependent on the effective stress level and the criterion for the onset of the plastic deformation is defined by the three-invariant yield condition, non-associated flow rule and the evolution a pressure-dependent law for hardening.

For a proper description of the material behavior it is necessary to ensure mesh-size-independent softening. The localized part of strain is in the model transformed into an equivalent crack opening after it reaches the peak of the stress-strain diagram. The fracturing strain is depended on the element size obtained by projecting the element onto the direction of the maximum principal strain. Crack opening can be controlled by G_f parameter, which is called fracture energy and has a physical meaning of energy dissipated by a crack developing over a unit area of the material.

3.3.1.1 Identification of Material Model Parameters

In order to ensure satisfactory results it was necessary to supply the material model with proper material parameters, namely: tensile strength – f_t , compression strength – f_c , Young’s modulus – E , fracture energy – G_f , hardening and softening parameters – A_{hard} , A_{soft} . These values had to be set for individual mortars and brick. Our approach to obtain these values consisted of an inverse FE analysis which was used to reproduce the experimentally obtained data. This approach was chosen to obtain the input model parameters to be directly used because we used un-notched specimens, so it was not possible to measure fracture energy (due to the unstable crack propagation). The mesh for the FE models was prepared in Salome, see Figure 3.5. In case of three-point-bending test the mesh was refined in the area of expected crack initiation (local size 2.5 mm, width of refined area 40 mm) and other parts were meshed more coarse (local size 10 mm). Compression test specimen was meshed uniformly with mesh local size 2.5 mm and for both Netgen 1D-2D-3D meshing algorithm was used. Boundary

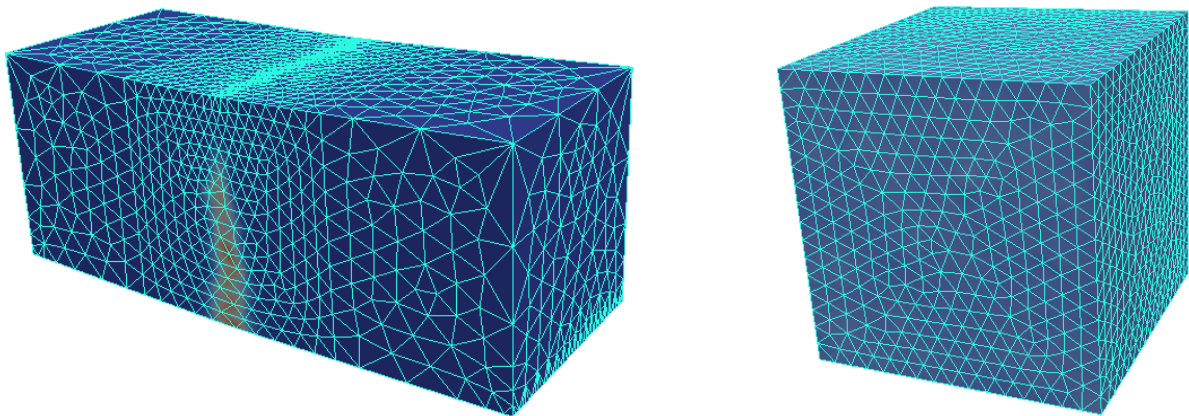


Figure 3.5: FE model of specimens for three-point bending (left) and uniaxial compression (right) tests.

conditions were added by MATLAB script. To prevent singularity in the case of three-point-bending test, bottom support was accomplished by supporting 1 mm wide plane area. Both tests were displacement-controlled and calculations were done in OOFEM, with the use of the above

mentioned damage-plastic material model.

Firstly E and the parameters to influence flexural strength - f_t and G_f were adjusted to achieve complying results of force-displacement diagram for case of three-point-bending. Than the material model parameters that influence the compression strength - f_c , A_{hard} and A_{soft} were calibrated by fitting the results of FE analysis from uniaxial compression tests. The Poisson's, ν , ratio was selected as 0.2 for both mortars and brick. This selection was not random, or intuitive, but it was based on other studies [23, 84, 85]. The influence of different Poisson's ratios was also tested. When set in range 0.1 and 0.3 it has a negligible impact on results, as confirmed by other studies [86, 87].

Natural materials contain a lot of discontinuities and other geometrical non-homogeneities which result in relatively high scatter of results. Result of fitting of three-point-bending and compression test for brick is provided by Figure 3.6. Complete results of fitting for mortars

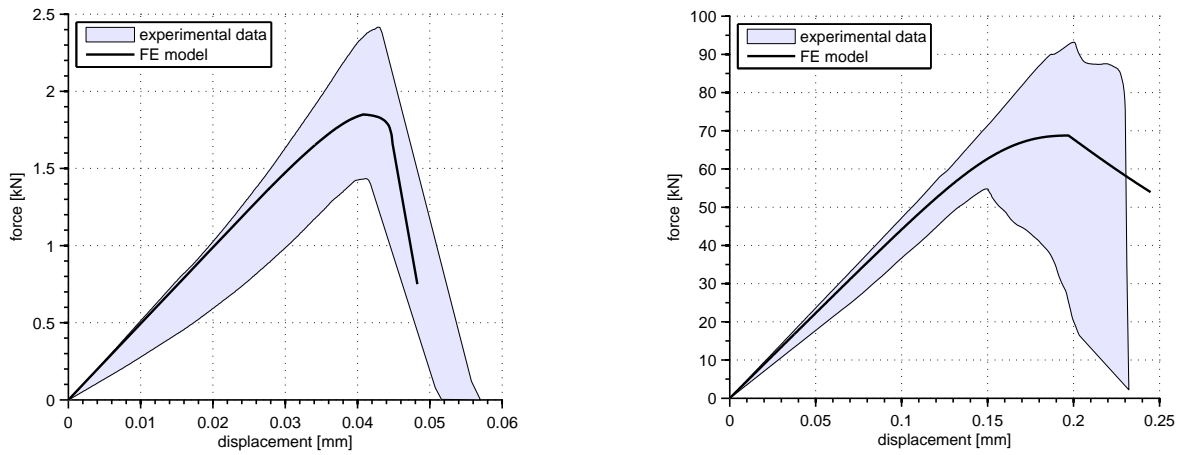


Figure 3.6: Fitting of the material model input parameters representing bricks on results of three-point bending (left) and uniaxial compression (right) tests.

samples is provided by Figures 3.7 and 3.8.

The summary of the material model input values for brick and all mortar samples is provided in Table 3.1.

Table 3.1: Key material input properties of bricks and the tested mortars; E , ν , f_c , f_t , and G_f denote the Young's modulus, Poisson's ratio, compressive strength, tensile strength, and fracture energy, respectively.

material	E [GPa]	ν [-]	f_c [MPa]	f_t [MPa]	G_f [J/m ²]	A_{soft} [-]	A_{hard} [-]
bricks	14.0	0.20	30.0	2.70	30.0	2.0	0.10
LC-S	7.10	0.20	4.80	0.55	3.20	1.0	0.08
LMK-S	7.40	0.20	11.3	1.53	13.5	3.0	0.08
LMK-SCB	10.0	0.20	14.7	1.92	26.0	1.0	0.08
L-SCB	2.45	0.20	1.30	0.26	1.55	1.0	0.08

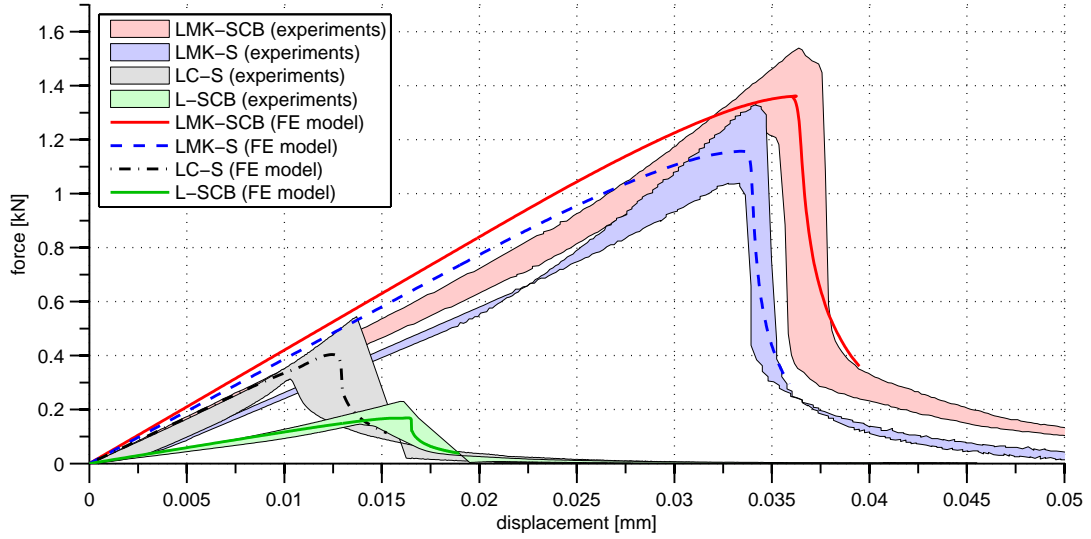


Figure 3.7: Fitting of the material model input parameters representing mortars on results of three-point bending tests.

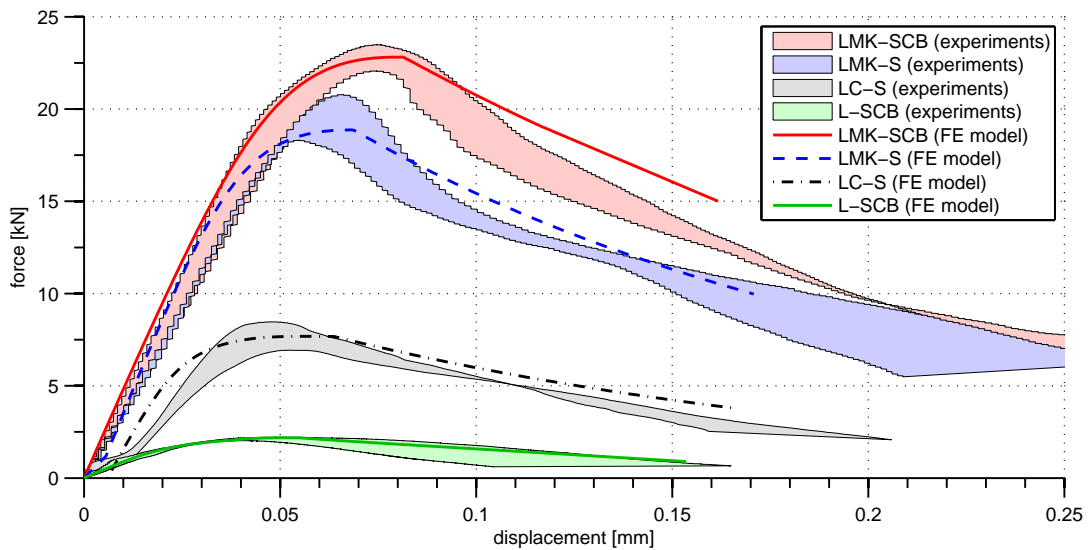


Figure 3.8: Fitting of the material model input parameters representing mortars on results of uniaxial compression tests.

3.3.2 Numerical Simulations of Masonry Pier Failure

Geometry of the masonry pier 3D FE model was same as in the cases of real destructive tests – geometry was presented in Figure 2.8. Meshing was carried out by the same program and algorithm as in case of basic FE models for obtaining basic material parameters – Netgen 1D-2D-3D implemented in Salome. General mesh was divided into sub-meshes to assure continuity of general mesh with sub-meshes meshed in different local sizes. Bricks were meshed with coarser elements (local size 10 mm) than in case of mortar joints (local size 6 mm). Loading of the piers was introduced to reproduce the experimental procedure realistically, so that the steel cylinder and steel slabs were also included in the model. Steel slabs and loading cylinder were modeled as an isotropic elastic continuum and local size of mesh elements was 10 mm.

The interface elements between bricks and surrounding mortar matrix was not defined, because interface was not the weakest link in the pull-out tests, for more detailed information see Section 3.1. The interface between steel slabs and mortar matrix was not modeled either, because modeling of this interface did not have any influence to the results. In total the mesh contained 63158 nodes and 396296 elements (2707 1D edges, 49415 2D faces, 344174 3D tetrahedron volumes). Figure 3.9 shows both – modeled geometry and meshed masonry pier.

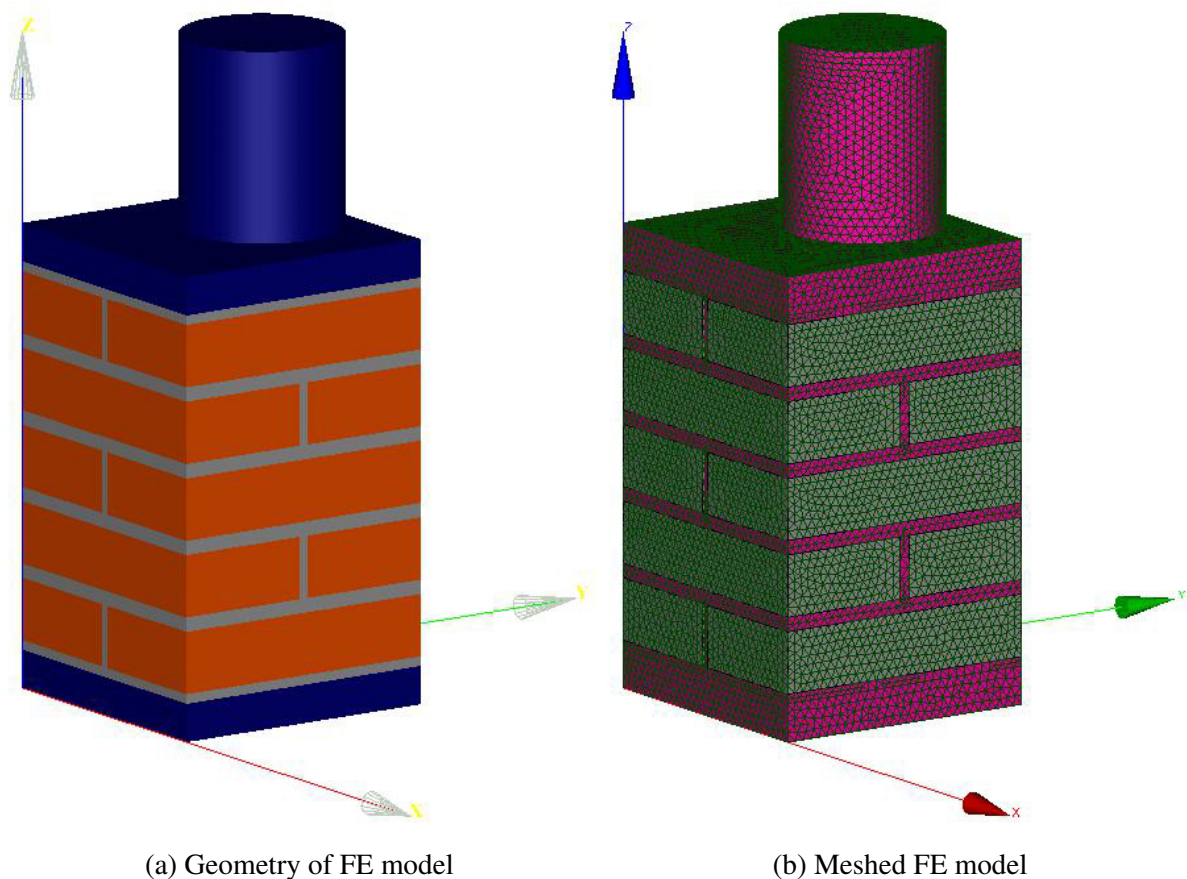


Figure 3.9: Geometry and FE mesh of investigated masonry pier.

Boundary conditions were applied through a MATLAB script. The script worked on the principle of detection desirable coordinates of nodes and putting the proper boundary conditions to these nodes. The boundary condition in the form of prescribed incremental z-displacement

was imposed upon the node in the center of the top base of the steel cylinder so that rotations were allowed around all axes. Second boundary condition ensured the support at the bottom – it was imposed onto a 1D line so that the rotations around all axes were allowed, see Figure 3.10.

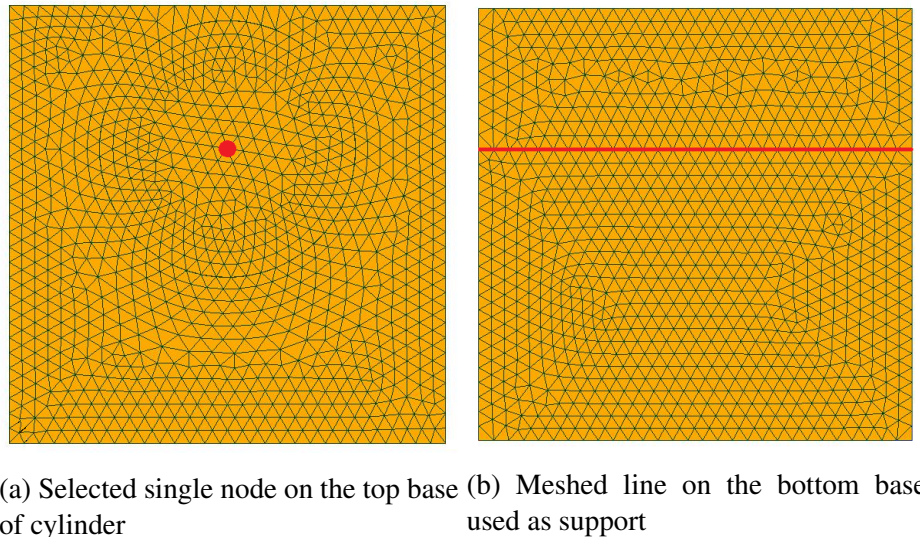


Figure 3.10: Boundary conditions of FE model.

Loading was defined by a time-function and load-step increments were chosen in to order minimize computational costs individually for each stage as shows example of the code snipped from OOFEM input bellow

```
nPoints 4 t 4 0 6 70 100 f(t) 4 0 0.6e-3 0.9e-3 1.5e-3
```

This example is for the pier where LMK-SCB mortar was used, for other piers with different mortar samples, function was defined with small differences. Time-function was defined by 4 points and totally contained 100 incremental steps. From 0 to 6 steps, the prescribed displacement was equal to 0.6×10^{-6} m, from 7 to 70 0.3×10^{-6} m, and from 71 step to 100 0.6×10^{-6} m. Steps were refined around the stage of initial cracks formation and propagation. MNR method of iteration together with a displacement error tolerance as a criterion to terminate iterations were used and maximum number of iterations was set to 1000, while minimum to 7. Full list of set up of calculation from OOFEM input file is presented below.

```
EC_column.out
EC_column_without_interface, nonlinear damage analysis
NonLinearStatic nSteps 100 rtolv 0.01 MaxIter 1000 MinIter 7
manrmsteps 50 stiffMode 0 controllmode 1 renumber 1 nmodules 1
profileOpt 1
vtxml timestep_all domain_all primvars 1 1 cellvars 1 102
vars 3 2 4 13 stype 1 nvr 3 vmap 4 1 2 3 0
domain 3d
OutputManager timestep_all dofman_all
ndofman 63158 nelem 396296 ncrosssect 3 nmat 3 nbc 2 nic 0 nltf 2
```

Computational procedures took approximately 54 hours each on a single core of six core Intel XEON X5680 with 32GB of RAM memory.

The FE model was validated by comparing the predicted and measured load-displacement diagrams during the real-scale destructive tests. The measurement of displacement during the tests was carried out by placing the virtual extensometers on the top and bottom of the pier in Ncorr_post environment, as shows Figure 2.8. Results obtained thought destructive tests, or more precisely evaluated by DIC are in a good accordance with the numerically obtained predictions. In Figure 3.11 the results of both – destructive tests and numerical simulations are summarized.

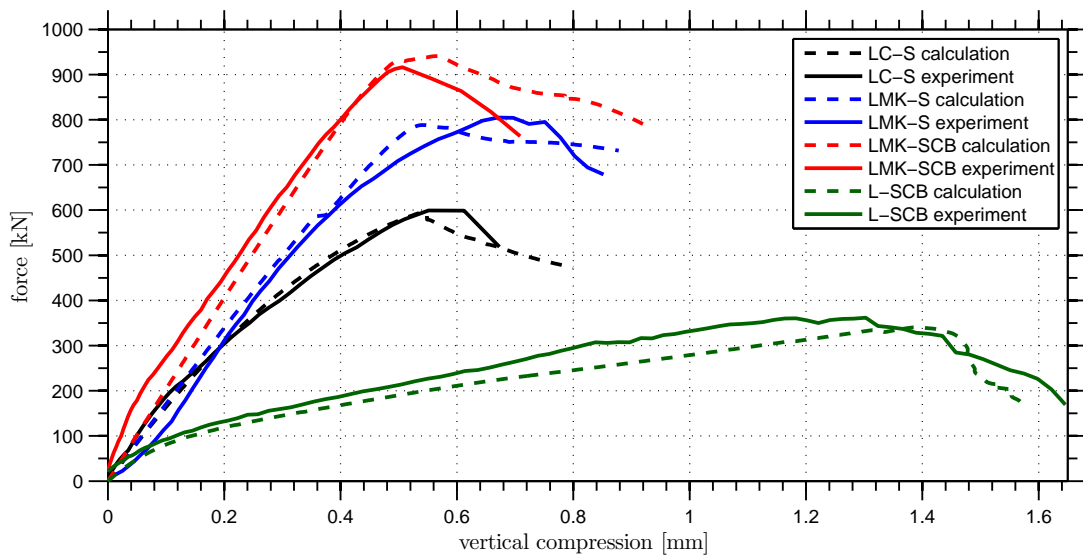


Figure 3.11: Comparison between the numerically and experimentally obtained load-displacement diagrams, describing the response of the tested masonry piers to the imposed vertical displacement at the crest of the loading cell.

Chapter 4

Results

This section provides the summarized results of both DIC and numerical simulations. In particular the crack patterns are compared and the differences are discussed. The results indicate the influence of different types of mortar on the load-bearing capacity of numerically modeled piers.

4.1 Comparison of Crack Patterns

Using DIC method the visualized maps of principal strains were evaluated and compared with the field of damage distribution provided by the FE model. Open-source program package Salome was used for evaluating the OOFEM *.vtu* output files. The DIC outputs were compared with the FE prediction at the same load-step. The predicted crack patterns by numerical simulations are not in a perfect match for all tested specimens. This could be caused by non-homogenous microstructure of mortars or neglecting some phenomena such as shrinkage.

In the case of lime-cement mortar, LC-S (Figure 4.1a), the model accurately predicted the mode of failure: dominant formation of major vertical cracks on the more loaded (compressed) side and formation of tensile cracks in mortar joints at the opposite side due to bending. In the case of lime-metakaolin mortar, LMK-S (Figure 4.1b) correspondence between DIC and FE model is not perfect. This was caused because the results of DIC were influenced by spalling the surface layer of contrast pattern at the bottom of the tested pier, probably due to bad cohesion with brick in this area. However, despite this limitation the major vertical crack formation in the middle of pier can be identified in both FE model and DIC results. On the other hand, a perfect agreement between FE model and DIC was obtained in case of LMK-SCB mortar, containing metakaolin and crushed bricks. Observed mode of failure was predominantly caused by formation of major splitting crack in the middle of pier (Figure 4.1c), probably due to the transverse expansion and exceeding the tensile strength of bricks. In the case of weak L-SCB mortar, a perfect correspondence between FE model and DIC was reached as well. Formation of dominant smeared cracking at the pier edge was observed in both (Figure 4.1d).

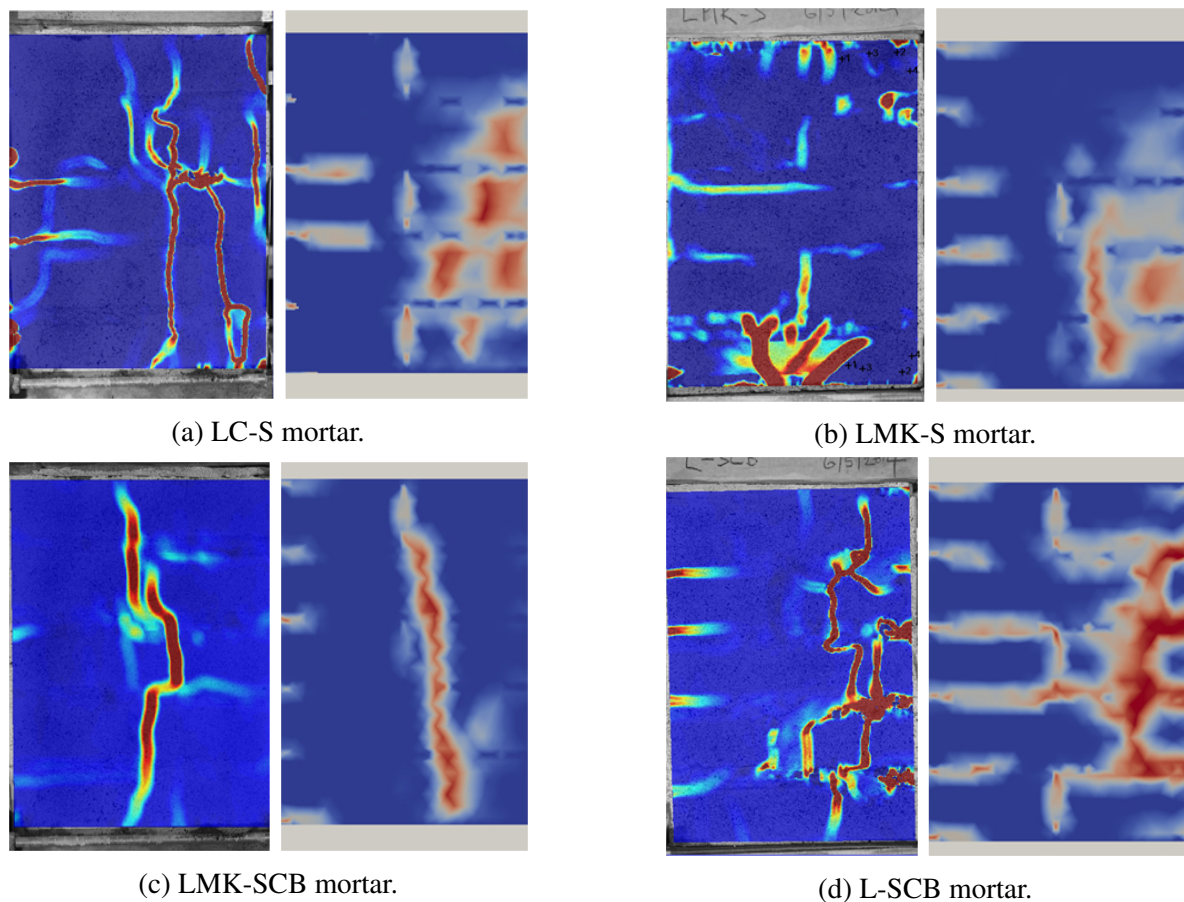


Figure 4.1: DIC map of maximum principal strain (left within the couple) and FE model damage prediction (right) on the face of the tested piers after reaching load-peak.

4.2 Influence of Mortar Properties on Mechanical Resistance of Masonry Piers

The aim of this section is to find the optimum mortar parameters to achieve the highest load-bearing capacity of the masonry piers loaded by a combination of compression and bending through the verified FE model. For that purpose the model configuration – geometry, FE mesh, materials, and boundary conditions – was considered the same as in the case of the verified model, except for the variable properties of the investigated mortars.

As the reference material lime-metakaolin mortar without crushed bricks (LMK-S) was chosen. For this type of mortar a single material parameter was changed at a time in order to examine its impact on the load-bearing capacity of the modeled masonry pier.

This analysis clearly indicates what material parameters have the major influence on the load-bearing capacity of the masonry, which can be considered in future design. A similar method of optimization was used e.g. in the study by Sandoval and Roca [87].

4.2.1 Influence of Mortar Young's modulus

It could be assumed that the mortar Young's modulus will have a major influence on the load-bearing capacity of studied pier, but an opposite conclusion was reached from the numerical model. There is even no abrupt change if the mortar change becomes stiffer than the masonry units. However, the failure mode has changed significantly. Figure 4.3 provides the comparison between both modes. Use of compliant mortar results in a multiple cracking of bricks at the more loaded side, while the proper support provided by the stiff mortars leads to the formation of a major crack passing through the entire pier.

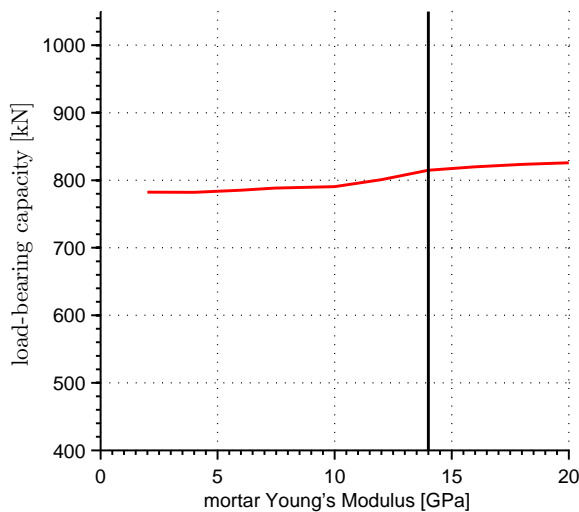


Figure 4.2: Dependence of the masonry pier load-bearing capacity on mortar stiffness; black line represents the Young's modulus of the bricks, $E^{(b)} = 14$ GPa.

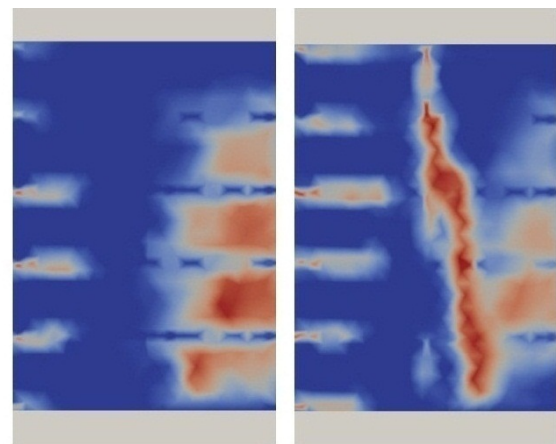


Figure 4.3: Crack patterns on masonry piers containing compliant ($E^{(m)} = 2$ GPa, left) and stiff ($E^{(m)} = 20$ GPa, right) mortar.

Use of less stiff mortars, e.g. without pozzolanic additives, could seem advantageous in order to produce masonry with a larger elastic range. These masonry systems in theory better resist seismic loading or imposed displacement due to differential settlement. Nevertheless, the less stiff compliant lime based mortars without additives suffer from an increased shrinkage cracking and lower resistance to moisture penetration into masonry.

4.2.2 Influence of Mortar Tensile Strength

The tensile strength and fracture energy had to be modified at the same time in order to avoid snap-back as documents the study done by Bažant [88]. Modification of these values at the same time was also important to preserve the same ductility for all investigated mortars.

The tensile strength of mortar has a minor effect on the load-carrying capacity of the pier, especially if the tensile strength of mortar is lower than tensile strength of masonry units. The mortars of a higher tensile strength in tension act as a masonry reinforcement. Tensile strengthening of mortars is usually accomplished e.g. by steel rods in the bed joints [89].

Our simulations predicted cracking of the bricks for mortars strong in tension. For the weaker mortars the formation of tensile cracks in bricks at the part of pier in tension is mitigated and a splitting crack occurs. On the other hand the tensile failure and formation of wedge in the case of strong mortars is illustrated in Figure 4.5.

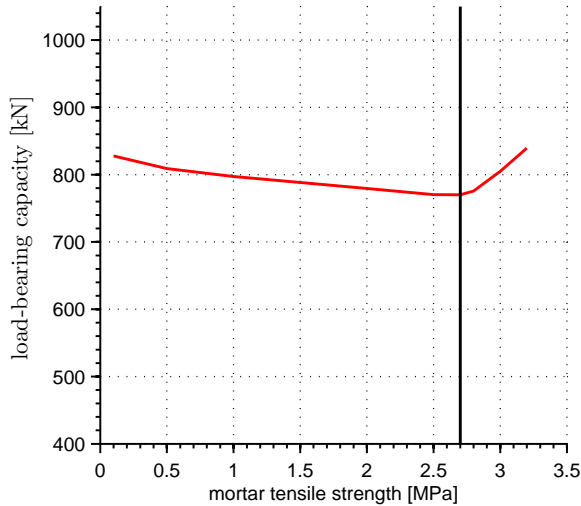


Figure 4.4: Dependence of the masonry pier load-bearing capacity on mortar tensile strength; black line represents the tensile strength of the bricks, $f_t^{(b)} = 2.7$ MPa.

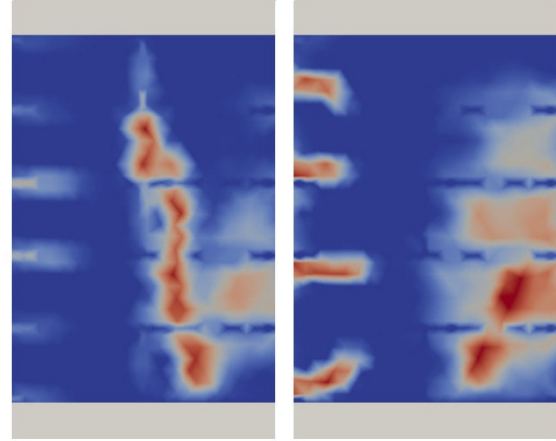


Figure 4.5: Crack patterns on masonry piers containing weak ($f_t = 0.1$ MPa, left) and strong ($f_t = 3.2$ MPa, right) mortar in tension.

4.2.3 Influence of Mortar Compressive Strength

The bed-joint mortar compressive strength determines the total load-bearing capacity of the masonry pier and as shows Figure 4.6. This material parameter seems to be crucial for masonry pier subjected to a combination of compression and bending. Weak mortars suffers an irreversible plastic deformations at low levels applied loading, which results in unbalanced supporting and excessive deformations of the bed joints on the more loaded side of the pier. This fact consequently results in the cracking of bricks as indicated in Figure 4.7. This mechanism seems to be the most significant in determining the load-bearing capacity, especially in the case of very poor mortars ($f_c^{(m)} < 10$ MPa). When the bed joints contain mortar of higher compressive strength, they do not suffer from the inelastic deformations in the early stages of loading and limiting factor influencing the load-bearing capacity seems to be the tensile strength of bricks subjected to transverse expansion. Similar mode of failure can be observed in the case of very stiff mortar (Figure 4.3). Therefore mortars with superior compressive strength should be used especially in the bed joints together with horizontal steel reinforcement mentioned above e.g. steel ladder or truss mesh to reach the full potential of these mortars.

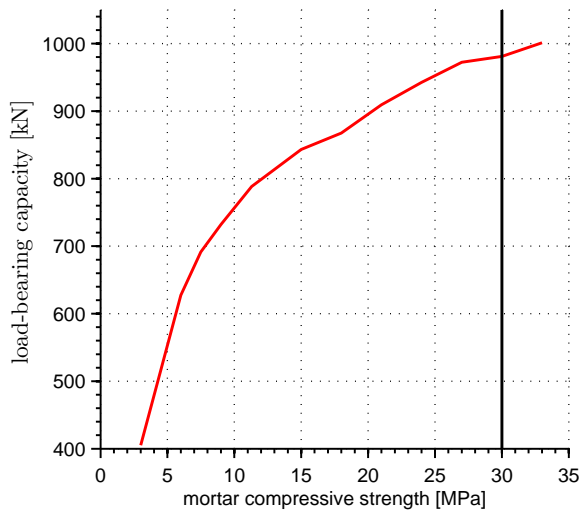


Figure 4.6: Dependence of the masonry pier load-bearing capacity on mortar compressive strength; black line represents the compressive strength of the bricks, $f_c^{(b)} = 30$ MPa.

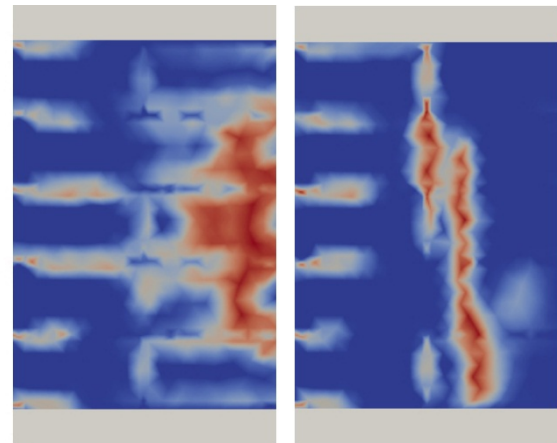


Figure 4.7: Crack patterns on masonry piers containing weak ($f_c = 3$ MPa, left) and strong ($f_c = 33$ MPa, right) mortar in compression.

4.3 Discussion of Results

The selected geometry of masonry pier with the boundary conditions was addressed as an example of typical load-bearing element in masonry, which was exposed to compression together with tension. Damage in tension is considered as critical for masonry systems. Conventionally used lime-cement mortar was compared with mortars containing active pozzolans – metakaolin and beside of this was experimented with adding an additive in form of crushed bricks to replace part of river sand aggregates. This intent was based on previous findings, e.g. [22, 24, 90], which declare that mortars containing active pozzolans and additives in form of crushed bricks should exhibit a superior strength.

The series of destructive tests, namely three-point bending, compression and pull-out tests, were carried out primarily in order to identify individual input parameters for materials in the FE model. The results of these tests indicate that the mentioned additives positively affect the material characteristics. In particular the addition of metakaolin provides the higher strength to the lime-based mortars than the addition of Portland cement. The pure-lime mortars lacking any additives exhibit very poor compression as well as tensile strength. These findings are in full agreement with previous studies; e.g. work by Vejmelková et al. [91] claiming that the 20 % replacement of lime by active pozzolan, metakaolin, can increase the compression strength of mortar up to five times and flexural strength up to three times, which is in full agreement with study by Velosa et al. [13].

The partial substitution of sand grains by crushed bricks fragments leads to a further improvement of the mechanical performance of lime-based mortars. This was discovered in the ancient times based on rules-of-thumb experience, explaining their extensive use in these times [25, 26, 29]. The higher strength is attributed to the formation of additional hydration

products at the interface between brick particles and surrounding lime-matrix and also due to the open porosity system of brick which enables to absorb water and then slowly release it to consequently reduce the shrinkage-induced cracking. This results in better mortar integrity as suggested by Nežerka et al. [22, 30] and lower stress concentration in surrounding matrix around the aggregate particles.

The better structural performance of metakaolin-enriched mortars was also reflected in the higher load-bearing capacity of the tested masonry piers. In case of pure lime mortar (L-SCB) peak force was only 360 kN, while 600 kN in the case of lime-cement mortar (LC-S). When 30 % of binder was replaced by metakaolin (LMK-S), load-bearing capacity increased up to 800 kN and further enhancement was observed with the use of mortar containing crushed bricks (LMK-SCB), reaching up to 915 kN. This superior strength can explain the high resistance and longevity of some ancient masonry structures containing lime-based mortars with crushed bricks, called *cocciopesto* [6, 36]. The mortar strength gain together with better adhesion between mortar and brick should also result in a better seismic resistance, as suggested by Costa et al. [92].

Damage-plastic material model used for 3D FE simulations, supplied with proper material parameters, allowed to reproduce the experimental results with a relatively very high accuracy even in the case of strongly non-homogeneous masonry. The chosen strategy to represent the mortar joints and bricks as two distinct materials allowed capturing the failure, usually consisting of vertical splitting cracks and consequent the complete failure, as also indicates research by Kaushik et al. [93]. The material characteristic with the highest impact on the load-bearing capacity of the masonry pier appeared to be the compression strength of mortar, which is in contradictions with the conclusions of Pavía et al. [94] and Gumaste et al. [95]. Results of their research indicate that the mortar compressive strength has just a slight influence on the load-bearing capacity of masonry elements subjected to uniaxial compression. This disagreement can be caused by different experimental set-up, in particular to the presence of bending moment and consequent tensile loading. The eccentric loading was responsible for the non-linear behavior at relatively early loading-stage because of differential bed joints deformation.

On the other hand, the mortar stiffness appears to have just a negligible impact on the load-bearing capacity. The suggestion of Zucchini and Lourenço [96] that the difference between the Young's moduli of bricks and mortar is the forerunner of the compression failure was not confirmed.

Chapter 5

Conclusions

The selected strategy to combine the comprehensive experimental analysis together with the numerical modeling revealed new findings to be used when designing bed joint mortars. The study was primarily focused on the lime-based mortars compatible with historical materials and their use is in accordance with the requirements of the authorities for cultural heritage. However, the information contained also provide new insight into the design of mortars based on modern materials.

The results of basic material tests indicate the superior strength of mortars enriched with metakaolin, in comparison with the pure-lime or the lime-cement based mortars. The strength can be further increased by the addition of crushed clay materials, such as bricks. In that case the strength enhancement is mostly attributed to the reduction of microcracking due to the reduced shrinkage and also to the formation of additional hydration products around the compliant ceramic aggregates. Moreover, the water retained within the crushed brick fragments is slowly released, supporting the hydraulic reactions taking place in the surrounding matrix.

The enhanced strength of mortars enriched by metakaolin and those containing crushed bricks was reflected to the greatly increased load-bearing capacity of masonry piers subjected to the compression and the bending load. This explains extraordinary resistance and durability of ancient masonry structures containing cocciopesto mortars. The use of ceramic waste by-products from ceramic plants makes this material sustainable for a relatively low cost, because the fragments partially replace binder, what is the most expensive mortar component.

Based on the comparison of the results of FE calculations and experimental observations, the damage-plastic model seems to be most suitable for the description of constitutive behavior. The chosen strategy to model the bricks and the mortars as two distinct materials led to a very accurate reproduction of the experimentally obtained data. The comparison of the FE calculations with the experiments was carried out in terms of matching the crack patterns obtained through DIC and by comparisons of the load-displacement diagrams. The experimental results as well as the numerical analysis indicate that the mortar properties have an enormous impact on the load-bearing capacity of masonry, strain localization and formation of cracks.

The numerical analysis, based on the properly validated FE model by the comprehensive experimental analysis, revealed that mortar compressive strength is the key material parameter with respect to the load-bearing capacity of the piers subjected to the combination of bending and compression load. Considering the studied geometry and boundary conditions, the influ-

ence of Young's modulus and tensile strength is reflected in the different modes of failure and crack patterns, however do not have any significant influence on the load-bearing capacity.

References

- [1] R. Siddall. In roman lime mortars using polarising light microscopy, <http://www.ucl.ac.uk/~ucfbrxs/plmlimes.html>.
- [2] J. Blaber. Ncorr digital image correlation software algorithms, <http://www.ncorr.com/index.php/dic-algorithms>. *Georgia Institute of Technology*, 2014.
- [3] J. Antoř. Investigation of Aggregate Influence on Fracture Properties of Mortars by FEA, Bachelor Thesis, Czech Technical University in Prague, 2013.
- [4] Sanpaz. Deformation of an infinitesimal rectangular material element, <http://wikimedia.org/wiki/file:2d-geometric-strain.svg>. 2009.
- [5] A. Khan and C. Lemmen. Bricks and urbanism in the indus valley rise and decline. *American Journal of Archeology*, 2013,.
- [6] A. Moropoulou, A.S. Cakmak, G. Biscontin, A. Bakolas, and E. Zendri. Advanced Byzantine cement based composites resisting earthquake stresses: the crushed brick/lime mortars of Justinians Hagia Sophia. *Construction and Building Materials*, 16:543–552, 2002.
- [7] C. Rodriguez-Navarro, E. Hansen, and W.S. Ginell. Calcium hydroxide crystal evolution upon aging of lime putty. *Journal of the American Ceramic Society*, 91(11):3032–3034, 1998.
- [8] O. Cazalla, C. Rodriguez-Navarro, E. Sebastian, and G. Cultrone. Aging of lime putty: effects on traditional lime mortar carbonation. *Journal of the American Ceramic Society*, 83(5):1070–1076, 2000.
- [9] A. Arizzi and G. Cultrone. Aerial lime-based mortars blended with a pozzolanic additive and different admixtures: A mineralogical, textural and physical-mechanical study. *Construction and Building Materials*, 31:135–143, 2012.
- [10] F. Veniale, M. Setti, C. Rodriguez-Navarro, S. Lodola, W. Palestra, and A. Busetto. Thamasite as decay product of cement mortar in brick masonry of a church near Venice. *Cement and Concrete Composites*, 25:1123–1129, 2003.
- [11] K. Callebaut, J. Elsen, K. Van Balen, and W. Viaene. Nineteenth century hydraulic restoration mortars in the Saint Michaels Church (Leuven, Belgium). Natural hydraulic lime or cement? *Cement and Concrete Research*, 31:397–403, 2001.

- [12] A. Moropoulou, A. Bakolas, and S. Anagnostopoulou. Composite materials in composite structures. *Cement and Concrete Composites*, 27:295–300, 2005.
- [13] A.L. Velosa, F. Rocha, and R. Veiga. Influence of chemical and mineralogical composition of metakaolin on mortar characteristics. *Acta Geodynamica et Geomaterialia*, 153:121–126, 2009.
- [14] M.P. Seabra, J.A. Labrincha, and V.M. Ferreira. Rheological behaviour of hydraulic lime-based mortars. *Journal of the European Ceramic Society*, 27:1735–1741, 2007.
- [15] A. Sepulcre-Aguilar and F. Hernández-Olivares. Assessment of phase formation in lime-based mortars with added metakaolin, Portland cement and sepiolite, for grouting of historic masonry. *Cement and Concrete Research*, 40:66–76, 2010.
- [16] P. Maravelaki-Kalaitzaki, A. Bakolas, and A. Moropoulou. Physico-chemical study of Cretan ancient mortars. *Cement and Concrete Research*, 33:651–661, 2003.
- [17] A. Moropoulou, A. Bakolas, and E. Aggelakopoulou. Evaluation of pozzolanic activity of natural and artificial pozzolans by thermal analysis. *Thermochimica Acta*, 420:135–140, 2004.
- [18] Z. Slížková. Characteristics of metakaoline modified mortars applied on historic objects. *Metakaolin, Brno*, pages 146–155, 2009.
- [19] I. Papayianni. The longevity of old mortars. *Applied Physics A*, 83:685–688, 2006.
- [20] I. Papayianni and M. Stefanidou. Durability aspects of ancient mortars of the archeological site of Olynthos. *Journal of Cultural Heritage*, 8:193–196, 2007.
- [21] D. Wilk, L. Bratasz, and R. Kozłowski. Shrinkage cracking in roman cement pastes and mortars. *Cement and Concrete Research*, 53:168–175, 2013.
- [22] V. Nežerka, Z. Slížková, P. Tesárek, T. Plachý, D. Frankeová, and V. Petráňová. Comprehensive study on microstructure and mechanical properties of lime-pozzolan pastes with additions of metakaolin and brick dust. *Cement and Concrete Research*, 64:17–29, 2014.
- [23] V. Nežerka and J. Zeman. A micromechanics-based model for stiffness and strength estimation of cocciopesto mortars. *Acta Polytechnica*, 52:29–37, 2012.
- [24] P. Tesárek, V. Nežerka, P. Padevět, J. Antoš, and T. Plachý. Influence of aggregate stiffness on fracture-mechanical properties of lime-based mortars. *Applied Mechanics and Materials*, 486:289–294, 2014.
- [25] G. Baronio, L. Binda, and N. Lombardini. The role of brick pebbles and dust in conglomerates based on hydrated lime and crushed bricks. *Construction and Building Materials*, 11:33–40, 1997.
- [26] L.G. Mallinson and I.L. Davies. A historical examination of concrete. *Office for Official Publications of the European Communities, Luxembourg, Final Report CD-NA-10937-EN-C*, 1987.

- [27] A. Farci, D. Floris, and P. Meloni. Water permeability vs. porosity in samples of Roman mortars. *Journal of Cultural Heritage*, 6:55–59, 2005.
- [28] L. Sbordoni-Mora. Les matériaux des enduits traditionnels. In: *Proceedings of the ICCROM Symposium on Mortars, Cements and Grouts used in the Conservation of Historic Buildings, Rome*, pages 375–383, 1981.
- [29] P. Degryse, J. Elsen, and M. Waelkens. Study of ancient mortars from Sagalassos (Turkey) in view of their conservation. *Cement and Concrete Research*, 21:1457–1463, 2002.
- [30] V. Nežerka, J. Němeček, Z. Slížková, and P. Tesárek. Investigation of crushed brick-matrix interface in lime-based ancient mortar by microscopy and nanoindentation. *Cement and Concrete Composites*, 55:122–128, 2015.
- [31] *EN 459-1:2010 - Building lime, Part 1: Definitions, specifications and conformity criteria*, 2010. European Standard.
- [32] H.F.W. Taylor. *Cement Chemistry, 2nd Ed.* Thomas Telford, London, 1997.
- [33] T. Jeff and J. Hamlin. The Science of Concrete, <http://iti.northwestern.edu/cement/monograph/monograph3-8.html>. Technical report, Northwestern University, Evanston, Illinois, 2014.
- [34] P. Gibbons. Pozzolans for Lime Mortars. *The Conservation and Repair of Ecclesiastical Buildings*, 1997.
- [35] M. Murat, J. Ambroise, , and J. Pera. Investigations on synthetic binders obtained by middle temperature thermal dissociation of clay minerals. *87th Annual Meeting of the American Ceramic Society*, pages Westerville, OH, 1985.
- [36] A. Moropoulou, A. Bakolas, and K. Bisbikou. Investigation of the technology of historic mortars. *Journal of Cultural Heritage*, 1:45–58, 2000.
- [37] A. Moropoulou, A. Bakolas, and K. Bisbikou. Characterization of ancient, Byzantine and later historic mortars by thermal and X-ray diffraction techniques. *Thermochemica Acta*, 269/270:779–995, 1995.
- [38] *ČSN EN 1015-1:1999 - Methods of test for mortar for masonry, Part 1: Determination of particle size distribution (by sieve analysis)*, 1999. Czech National Standard.
- [39] *ČSN EN 1015-3:2000 - Methods of test for mortar for masonry, Part 3: Determination of consistence of fresh mortar (by flow table)*, 2000. Czech National Standard.
- [40] J. Lanas, J.L. Pérez Bernal, M.A. Bello, and J.I. Alvarez Galindo. Mechanical properties of natural hydraulic lime-based mortars. *Cement and Concrete Research*, 34:2191–2201, 2004.
- [41] M. Stefanidou and I. Papayianni. The role of aggregates on the structure and properties of lime mortars. *Cement & Concrete Composites*, 27:914–919, 2005.

- [42] ČSN EN 1015-11:1999 - *Methods of test for mortar for masonry, Part 11: Determination of flexural and compressive strength of hardened mortar*, 1999. Czech National Standard.
- [43] ČSN EN 1015-2:1999 - *Methods of test for mortar for masonry, Part 2: Bulk sampling of mortars and preparation of test mortars*, 1999. Czech National Standard.
- [44] P. Tesárek, T. Plachý, A. Hájková, P. Padevět, and M. Polák. Time evolution of “grey gypsum” mechanical properties. *Latest Trends in Engineering Mechanics, Structures, Engineering Geology, Athens, WSEAS Press*, pages 413–417, 2010.
- [45] T. Plachý, P. Padevět, and M. Polák. Comparison of two experimental techniques for determination of Young’s modulus of concrete specimens. *Proceedings of the 5th WSEAS International Conference on Applied and Theoretical Mechanics - Recent Advances In Applied And Theoretical Mechanics, Athens, WSEAS Press*, pages 68–71, 2009.
- [46] A. Malaikah, K. Al-Saif, and R. Al-Zaid. Prediction of the dynamic modulus of elasticity of concrete under different loading conditions. *International Conference On Concrete Engineering and Technology Universiti Malaya*, 2004.
- [47] ČSN EN 1015-12:1999 - *Methods of test for mortar for masonry, Part 12: Determination of adhesive strength of hardened rendering and plastering mortars on substrates*, 2000. Czech National Standard.
- [48] J.N. Périé, S. Calloch, C. Cluzel, and F. Hild. Analysis of a multiaxial test on a c/c composite by using digital image correlation and a damage model. *Experimental Mechanics*, 42:505–515, 2002.
- [49] I. Yamaguchi. A laser speckle strain gauge. *Journal of Physics E: Scientific Instruments*, 14:1270, 1981.
- [50] W.H. Peters and W.F. Ranson. Digital imaging techniques in experimental stress analysis. *Optical Engineering*, 21:427–431, 1982.
- [51] H. Lu and P.D. Cary. Deformation measurements by Digital Image Correlation: Implementation of a second-order displacement gradient. *Experimental Mechanics*, 40:393–400, 2000.
- [52] B. Pan, H. Xie, and Z. Wang. Equivalence of Digital Image Correlation criteria for pattern matching. *Applied Optics*, 49:5501–5509, 2010.
- [53] B. Pan and K. Li. A fast digital image correlation method for deformation measurement. *Optics and Lasers in Engineering*, 49:841–847, 2011.
- [54] B. Pan, K. Li, and W. Tong. Fast, robust and accurate Digital Image Correlation calculation without redundant computations. *Experimental Mechanics*, 53:1277–1289, 2013.
- [55] A. H. Salmanpour and N. Mojsilovi. Application of Digital Image Correlation for strain measurements of large masonry walls. *APCOM & ISCM*, 2013.

- [56] S.H. Tung, M.H. Shih, and W.P. Sung. Development of Digital Image Correlation method to analyse crack variations of masonry walls. *Sadhana*, 33:767–779, 2008.
- [57] S.V. Lomov, D.S. Ivanov, I. Verpoest, M. Zako, T. Kurashiki, H. Nakai, J. Molimard, and A. Vautrin. Full-field strain measurements for validation of meso-fe analysis of textile composites. *Composites Part A: Applied Science and Manufacturing*, 39:1218–1231, 2008.
- [58] G. Tao and Z. Xia. A non-contact real-time strain measurement and control system for multiaxial cyclic / fatigue tests of polymer materials by digital image correlation method. *Polymer Testing*, 24:844–855, 2005.
- [59] J. Blaber. Ncorr digital image correlation software, <http://www.ncorr.com/>. *Georgia Institute of Technology*, 2014.
- [60] V. Nežerka. Ncorr_post: Dic post-processing tool, <http://mech.fsv.cvut.cz/~nezerka/dic/index.htm>. *CTU in Prague*, 2014.
- [61] Inc. The MathWorks. Matlab release 2011a, <http://www.mathworks.com/products/matlab/>. *Natick, Massachusetts, U.S.*, 2011.
- [62] B. Pan, H. Xie, Z. Guo, and T. Hua. Full-field strain measurement using a two-dimensional Savitzky-Golay digital differentiator in digital image correlation. *Optical Engineering*, 46:033601, 2007.
- [63] D. Lecompte, A. Smits, Bossuyt S., H. Sol, J. Vantomme, D. Van Hemelrijck, and A.M. Habraken. Quality assessment of speckle patterns for digital image correlation. *Optics and Lasers in Engineering*, 44:1132–1145, 2006.
- [64] G. Stoilov, V. Kavardzhikov, and D. Pashkouleva. A comparative study of random patterns for digital image correlation. *Journal of Theoretical and Applied Mechanics*, 42:55–66, 2012.
- [65] B. Pan, Z. Lu, and H. Xie. Mean intensity gradient: An Effective global parameter for quality assessment of the speckle patterns used in digital image correlation. *Optics and Lasers in Engineering*, 48:469–477, 2010.
- [66] Inc. Correlated Solutions. Correlated Solutions VIC-2D guide, <http://www.correlatedsolutions.com/vic-2d/>. 2014.
- [67] S. Sun Yaofeng and J. H.L. Pang. Mean intensity gradient: An Effective global parameter for quality assessment of the speckle patterns used in digital image correlation. *Optics and Lasers in Engineering*, 45:967–974, 2007.
- [68] J. Blaber. Ncorr instruction manual, <http://www.ncorr.com/download/ncorrmanual.pdf>. *Georgia Institute of Technology*, 2014.
- [69] V. Nežerka. Ncorr_post: Instruction manual, http://mech.fsv.cvut.cz/~nezerka/dic/_files/ncorr_post20-20manual.pdf. *CTU in Prague*, 2014.

- [70] P. B. Lourenço. Computations on historic masonry structures. *Progress in Structural Engineering and Materials*, 4:301–319, 2002.
- [71] D. Roylance. *Mechanical Properties of Materials*. MIT, 2008.
- [72] D.R. Smith and C. Truesdell. *An Introduction to Continuum Mechanics after Truesdell and Noll*. Springer, 1993.
- [73] G. Pelosi. The finite-element method, part i: R. L. Courant [Historical Corner]. *IEEE Antennas and Propagation Magazine*, 49:180–182, 2007.
- [74] R.L. Courant. Variational methods for the solution of problems of equilibrium and vibration,. *Bulletin of the American Mathematical Society*, 49:1–23, 1943.
- [75] B. Patzák and Z. Bittnar. Design of object oriented finite element code. *Advances in Engineering Software (www.oofem.org)*, 32:759–767, 2001.
- [76] G. Narasaiah. *Finite element analysis*. Hyderabad: BS Publications, 2008.
- [77] M. Šejnoha. Lecture notes on Structural Mechanics 3, <http://ksm.fsv.cvut.cz/~sejnom/download/sm3.pdf>. 2010.
- [78] X. Zhou, M. Chu, S. Liu, S. Qu, and H. Fan. Elasticity damage and plastic analyses of masonry. *Applied Mechanics and Materials*, 166:1454–1458, 2012.
- [79] A. Wawrzynek and A. Cincio. Plastic-damage macro-model for non-linear masonry structures subjected to cyclic or dynamic loads. In: *Proc. Conf. Analytical Models and New Concepts in Concrete and Masonry Structures, AMCM, Gliwice, Poland, 2005*.
- [80] M. Jirásek and P. Grassl. Damage-plastic model for concrete failure. *International Journal of Solids and Structures*, 43:7166–7196, 2006.
- [81] S.A.S OPEN CASCADE. Salome v. 7.4.0, <http://www.salome-platform.org/>. Guyancourt, France, 2014.
- [82] A. Henderson. ParaView Guide, A Parallel Visualization Application. *Kitware Inc.*, 2007.
- [83] M. Jirásek. Mathematical analysis of strain localization. *Revue Europeenne de Génie Civil*, 11:977–991, 2007.
- [84] M. Drdácěký and D. Michoinová. Lime mortars with natural fibres. *Brittle Matrix Composites, Proceedings of the 7th Int. Symposium*, pages 523–532, 2003.
- [85] J. Vorel, V. Šmilauer, and Z. Bittnar. Multiscale simulations of concrete mechanical tests. *Journal of Computational and Applied Mathematics*, 236:4882–4892, 2012.
- [86] V. Corinaldesi. Mechanical behavior of masonry assemblages manufactured with recycled aggregate mortars. *Cement and Concrete Composites*, 31:505–510, 2009.
- [87] C. Sandoval and P. Roca. Study of the influence of different parameters on the buckling behaviour of masonry walls. *Construction and Building Materials*, 35:888–899, 2012.

- [88] Z.P. Bažant and B.H. Oh. Crack band theory for fracture of concrete. *Materials and Structures*, 16:155–177, 1983.
- [89] M. Valluzzi, C. Binda, and C. Modena. Mechanical behaviour of historic masonry structures strengthened by bed joints structural repointing. *Construction and Building Materials*, 19:63–73, 2005.
- [90] V. Nežerka, P. Tesárek, and J. Zeman. Fracture-micromechanics based model of mortars susceptible to shrinkage. *Key Engineering Materials*, 592–593:189–192, 2014.
- [91] E. Vejmelková, M. Keppert, Z. Keršner, P. Rovnaníková, and R. Černý. Mechanical, fracture-mechanical, hydric, thermal, and durability properties of lime-metakaolin plasters for renovation of historical buildings. *Construction and Building Materials*, 31:22–28, 2012.
- [92] A. Costa, A. Arêde, A. Costa, J. Guedes, and B. Silva. Experimental testing, numerical modelling and seismic strengthening of traditional stone masonry: comprehensive study of a real Azorian pier. *Bulletin of Earthquake Engineering*, 10:135–159, 2012.
- [93] H. Kaushik, D. Rai, and S. Jain. Stress-strain characteristics of clay brick masonry under uniaxial. *Journal of Materials in Civil Engineering*, 19:728–739, 2007.
- [94] S. Pavía and R. Hanley. Flexural bond strength of natural hydraulic lime mortar and clay brick. *Materials and Structures*, 43:913–922, 2010.
- [95] K. Gumaste, K. Nanjunda Rao, B. Venkatarama Reddz, and K. Jagadish. Strength and elasticity of brick masonry prisms and wallettes under compression. *Materials and Structures*, 40:241–253, 2007.
- [96] A. Zucchini and P. B. Lourenço. Mechanics of masonry in compression: Results from a homogenisation approach. *Computers and Structures*, 85:193–204, 2007.